

Durham E-Theses

The aerodynamics of curved jets and breakaway in Coanda flares

Senior, Peter

How to cite:

Senior, Peter (1991) *The aerodynamics of curved jets and breakaway in Coanda flares*, Durham theses, Durham University. Available at Durham E-Theses Online: <http://etheses.dur.ac.uk/6199/>

Use policy

The full-text may be used and/or reproduced, and given to third parties in any format or medium, without prior permission or charge, for personal research or study, educational, or not-for-profit purposes provided that:

- a full bibliographic reference is made to the original source
- a [link](#) is made to the metadata record in Durham E-Theses
- the full-text is not changed in any way

The full-text must not be sold in any format or medium without the formal permission of the copyright holders.

Please consult the [full Durham E-Theses policy](#) for further details.

The Aerodynamics of Curved Jets and Breakaway in Coanda Flares

Peter Senior 1991

An investigation was carried out into external-Coanda Effect flares designed by British Petroleum International plc. The phenomenon of interest was breakaway of an underexpanded axisymmetric curved wall jet from the guiding surface due to high blowing pressure. A survey of investigations of similar flows suggested very complex jet fluid dynamics. Strong cell structure including shock waves was present giving bulk and discrete compression and bulk dilatation. More expansion was imposed by the radial velocity components. Wall curvature and a rear-facing step added further significant influences. The combination of these factors is known to produce highly non-linear turbulence, and this constitutes a major difficulty for the application of computational methods to the flare. In view of the amount of resources required to eliminate the problems of using a Navier-Stokes code, an economical approach was adopted, matching the Method of Characteristics to various simplified models and an integral boundary layer.

In the experimental work, a planar model of the flare was constructed and studied using a wide range of methods in order to achieve accuracy and provide comparability with other work. An axisymmetric model was designed and investigated in a similar manner, so that the influence of this geometry could be clearly distinguished. A full-scale flare was subjected to a restricted range of tests to compare the laboratory results with the industrial application. The results from all the experiments demonstrated good correspondence. The main conclusion was that amalgamation of separation bubbles is crucial for breakaway. These are present long before breakaway, and are strongly reduced by decreasing the cell scale, adding a rear-facing step and axisymmetry, which leads to improved breakaway performance. Although the computational methods did not prove robust enough for all design purposes, they did permit significant insights into the mechanism of breakaway.

The Aerodynamics of Curved Jets and Breakaway in Coanda Flares

Volume 1 of 2

Peter Senior

The copyright of this thesis rests with the author.
No quotation from it should be published without
his prior written consent and information derived
from it should be acknowledged.

University of Durham
School of Engineering and Applied Science

Thesis submitted AD1991 for
the Degree of Doctor of Philosophy



10 FEB 1992

Table of Contents

1	INTRODUCTORY REMARKS	1
1.1	RESEARCH MOTIVATION	1
1.1.1	The INDAIR Flare	1
1.1.2	High Speed Jet Flows	3
1.2	PROJECT OBJECTIVES	3
1.3	THESIS STRUCTURE	5
1.3.1	Nomenclature	5
1.3.2	Layout of the Chapters	5
2	LITERATURE BACKGROUND	7
2.1	COANDA FLARES	7
2.1.1	The Coanda Effect	7
2.1.2	The Flare Flowfield	9
2.1.2.1	General Structure	9
2.1.2.2	Boundary Layer and Separation	11
2.1.2.3	Pressure Gradient, Curvature and Divergence Effects	12
2.1.2.4	Deviations from Steady Two-Dimensional Flow	14
2.1.2.5	Supersonic Base Flow	17
2.1.2.6	The Mixing Layer	19
2.1.2.7	Real Flare Effects	19
2.2	FLUID DYNAMIC COMPUTATION	20
2.2.1	Numerical Method Requirements	20
2.2.2	Inviscid and Empirical Models	24
2.2.3	Solutions of the Complete Flowfield	26
2.2.4	Multiple Zone Methods	32

3 INTERACTING ZONE TECHNIQUES	37
3.1 THE POTENTIAL CORE	37
3.1.1 Euler Equation Solvers	37
3.1.2 The Method of Characteristics	38
3.2 THE BOUNDARY LAYER	39
3.2.1 Integral, Differential and Series Representations	39
3.2.2 Laminar and Turbulent Models	44
3.2.3 Further Complications	48
3.3 SUPERSONIC BASE MODELLING	51
3.4 ZONE INTERACTION	54
3.4.1 Matching Parameters	54
3.4.2 Coupling Algorithms	58
4 COMPUTATIONAL METHOD DEVELOPMENT	61
4.1 METHOD OF CHARACTERISTICS	61
4.1.1 Previously Existing Code	61
4.1.2 Specifications for the MOC Code	62
4.1.3 Details of the Computation	64
4.1.3.1 Basic Algorithm	64
4.1.3.2 Boundary Conditions	66
4.1.3.3 Base Pressure Model	69
4.1.3.4 Shock Waves	69
4.1.3.5 Shock Interactions	72
4.1.3.6 Axisymmetry and Initialisation	76
4.1.3.7 Testing	77
4.2 BOUNDARY LAYER METHOD	77
4.2.1 Description	77
4.2.2 Implementation	79
4.2.3 Matching Procedure	80
4.2.4 Testing	80
4.3 PRESENTATION PROGRAM	81
4.3.1 Objectives and Structure	81
4.3.2 Comparison and Presentation	82
4.3.3 Presentation Formats	83
4.3.3.1 Surface Pressure Plots	83
4.3.3.2 Contour Plots	83
4.3.3.3 Simulated Visualisations	84
4.3.3.4 Breakaway Plots	86
4.4 HYSTERESIS SIMULATION	86

5 EQUIPMENT DESIGN	89
5.1 BACKGROUND	89
5.1.1 Visualisation Methods	89
5.1.1.1 Shadowgraph and Schlieren Techniques	89
5.1.1.2 Surface Flow Visualisation Method	92
5.1.2 Metrology	93
5.1.2.1 Interferometry	94
5.1.2.2 Nephelometry	95
5.1.2.3 Other Methods	97
5.2 VIBRATION ISOLATION	98
5.2.1 Design Motivation	98
5.2.2 Mechanical Rig Suspension System	99
5.2.3 Optical Rig Suspension System	101
5.3 SHADOWGRAPH EQUIPMENT FOR FULL-SCALE TESTS	103
5.4 PLANAR STEPPED RIG DESIGN	105
5.4.1 Design Objectives	105
5.4.2 Adopted Solution	106
5.5 THE AXISYMMETRIC MODEL	109
5.5.1 Design Objectives	109
5.5.2 Adopted Solution	109
5.5.3 Air Supply Modifications	114
6 EXPERIMENTAL TECHNIQUES	117
6.1 INTERFEROMETRY	117
6.1.1 Planar Build General Optical Alignment Procedure	117
6.1.2 Image Adjustment and Photography	120
6.1.3 Optical Cleaning Procedure	121
6.1.4 Interferogram Processing	122
6.2 SCHLIEREN VISUALISATION	124
6.2.1 Axisymmetric Build General Optical Alignment Procedure	124
6.2.2 Optical Rig Conversion	126
6.2.3 Image Adjustment and Photography	127
6.3 SHADOWGRAPH VISUALISATION	128
6.3.1 Flare Model Tests	128
6.3.2 Full Scale Field Tests	128
6.4 SURFACE FILM VISUALISATION	129
6.4.1 Optical System and Photography	129
6.4.2 Full Scale Field Tests	132

6 EXPERIMENTAL TECHNIQUES	<i>continued</i>
6.5 SURFACE PRESSURE MEASUREMENT	132
6.6 MECHANICAL RIG OPERATION	134
6.6.1 Cleaning and Assembly	134
6.6.2 Processing of Instrumentation Output	135
6.6.3 Breakaway Test Procedure	137
7 PLANAR COANDA RESULTS	139
7.1 EXPERIMENTAL WORK	139
7.1.1 Flowfield Measurements	139
7.1.1.1 Breakaway and Reversion Tests	139
7.1.1.2 Interferometry	141
7.1.1.3 Surface Pressure Measurement	143
7.1.2 Flowfield Visualisations	148
7.1.2.1 Interpretation of Photographs	148
7.1.2.2 Unstepped Schlieren and Shadowgraphy	148
7.1.2.3 Base Step Schlieren and Shadowgraphy	150
7.1.2.4 Surface Oil Flow Visualisation	155
7.2 COMPUTATIONAL MODELLING RESULTS	159
7.2.1 Base Pressure Model	159
7.2.2 Method of Characteristics	160
7.2.2.1 Attached Jet Simulations	160
7.2.2.2 Simulations using Experimental Data	161
7.2.2.3 Simulations using Pressure Models – Stepped Model	164
7.2.2.4 Simulations using Pressure Models – Zero Step	165
8 AXISYMMETRIC COANDA RESULTS	169
8.1 EXPERIMENTAL WORK	169
8.1.1 Flowfield Measurements	169
8.1.1.1 Breakaway and Reversion Tests	169
8.1.1.2 Surface Pressure Measurement	170
8.1.2 Flowfield Visualisations	175
8.1.2.1 Interpretation of Photographs	175
8.1.2.2 Unstepped Schlieren and Shadowgraphy	176
8.1.2.3 Base Step Schlieren and Shadowgraphy	180
8.1.2.4 Surface Oil Flow Visualisation	184
8.1.2.5 Field Tests	187
8.2 COMPUTATIONAL MODELLING RESULTS	188
8.2.1 Base Pressure Model	188
8.2.2 Method of Characteristics	189
8.2.2.1 Pressure Model Simulations	189
8.2.2.2 Calculations using Experimental Data	194
8.2.2.3 Field Test Simulations	198

9 DISCUSSION	200
9.1 EXPERIMENTAL FINDINGS	200
9.1.1 Breakaway And Reversion Mechanisms	200
9.1.2 Relevance of Planar Work to the Axisymmetric Model	207
9.1.3 Relevance of Laboratory Results to Industrial Flares	208
9.2 COMPUTATIONAL MODELLING	209
9.2.1 Base Pressure Model	209
9.2.2 Method of Characteristics	210
9.2.3 Boundary Layer Method	212
9.3 OUTLOOK FOR SUPERSONIC COANDA JET RESEARCH	213
9.3.1 Summary Of Current Position	213
9.3.2 Possible Development Routes	215
9.3.3 Implications for Design Improvements	218
9.3.4 By-Products for Other Purposes	222
10 CONCLUSIONS	224
LIST OF REFERENCES	227

List of Figures

- Figure 1.1 Coanda Flare Variants
- Figure 2.1 Coanda Flare Flowfield Schematic
- Figure 2.2 Shock–Boundary Layer Interactions
- Figure 4.1 Method of Characteristics Unit Processes
- Figure 4.2 Expansion Corner MoC Unit Process
- Figure 4.3 Shocked MoC Unit Process
- Figure 4.4 Edge Shock Reflection MoC Unit Processes
- Figure 4.5 Boundary Layer Marching Test Case
- Figure 4.6 Comparison of MoC with Boundary Layer Method
- Figure 5.1 Mechanical Rig Suspension
- Figure 5.2 Mechanical Rig Leg Tube
- Figure 5.3 Planar Flare Model
- Figure 5.4 Axisymmetric Flare Model
- Figure 5.5 Axisymmetric Flare Support
- Figure 5.6 Air Supply Layout
- Figure 6.1 Optical Apparatus Planar Build
- Figure 6.2 Optical Apparatus Axisymmetric Build
- Figure 6.3 Flare Model Surface Flow Visualisation Photography Layout
- Figure 6.4 Manometer Tube Photography
- Figure 7.1.1 Planar Coanda Model Breakaway Behaviour
- Figure 7.1.2 Planar Coanda Model Reversion Behaviour
- Figure 7.1.3 Planar Coanda Model Partial Reversion Behaviour
- Figure 7.1.4 Planar Coanda Model Breakaway/Reversion Behaviour
- Figure 7.1.5 Interferometry Fringe Pattern – Choking
- Figure 7.1.6 Interferometry Density Contours – Choking
- Figure 7.1.7 Interferometry Pressure Contours – Choking
- Figure 7.1.8 Interferometry Mach Number Contours – Choking
- Figure 7.1.9 Interferometry Density Contours – Underexpanding
- Figure 7.1.10 Interferometry Pressure Contours – Underexpanding
- Figure 7.1.11 Interferometry Mach Number Contours – Underexpanding

- Figure 7.1.12 Planar Coanda Model Experimental Surface Pressures: Slot 2.00 mm, Step 0.00 mm
- Figure 7.1.13 Planar Coanda Model Experimental Surface Pressures: Slot 2.00 mm, Step 0.75 mm
- Figure 7.1.14 Planar Coanda Model Experimental Surface Pressures: Slot 2.00 mm, Step 1.50 mm
- Figure 7.1.15 Planar Coanda Model Experimental Surface Pressures: Slot 2.00 mm, Step 1.50 mm
- Figure 7.1.16 Planar Coanda Model Experimental Surface Pressures: Slot 4.00 mm, Step 0.00 mm
- Figure 7.1.17 Planar Coanda Model Experimental Surface Pressures: Slot 4.00 mm, Step 0.75 mm
- Figure 7.1.18 Planar Coanda Model Experimental Surface Pressures: Slot 4.00 mm, Step 1.50 mm
- Figure 7.1.19 Planar Coanda Model Experimental Surface Pressures: Slot 4.00 mm, Step 1.50 mm
- Figure 7.1.20 Planar Coanda Model Experimental Surface Pressures: Slot 4.00 mm, Step 2.55 mm
- Figure 7.1.21 Planar Coanda Model Experimental Surface Pressures: Slot 4.00 mm, Step 3.76 mm
- Figure 7.1.22 Planar Coanda Model Experimental Surface Pressures: Slot 4.00 mm, Step 3.76 mm
- Figure 7.1.23 Planar Coanda Model Experimental Surface Pressures: Slot 6.00 mm, Step 0.00 mm
- Figure 7.1.24 Planar Coanda Model Experimental Surface Pressures: Slot 6.00 mm, Step 0.75 mm
- Figure 7.1.25 Planar Coanda Model Experimental Surface Pressures: Slot 6.00 mm, Step 1.50 mm
- Figure 7.1.26 Planar Coanda Model Experimental Surface Pressures: Slot 6.00 mm, Step 3.75 mm
- Figure 7.1.27 Planar Coanda Model Experimental Surface Pressures: Slot 8.00 mm, Step 0.00 mm
- Figure 7.1.28 Planar Coanda Model Experimental Surface Pressures: Slot 8.00 mm, Step 0.75 mm
- Figure 7.1.29 Planar Coanda Model Experimental Surface Pressures: Slot 8.00 mm, Step 1.50 mm
- Figure 7.1.30 Planar Coanda Model Experimental Surface Pressures: Slot 8.00 mm, Step 3.75 mm
- Figure 7.1.31 Planar Flare Model Endwall Flow
- Figure 7.2.1 Planar Coanda Model Base Pressures: Slot 2.00 mm
- Figure 7.2.2 Planar Coanda Model Base Pressures: Slot 4.00 mm
- Figure 7.2.3 Planar Coanda Model Base Pressures: Slot 6.00 mm
- Figure 7.2.4 Planar Coanda Model Base Pressures: Slot 8.00 mm

- Figure 7.2.5 Planar Coanda Model Method of Characteristics Plot:
Slot 2.00 mm, Step 0.00 mm, $C_{po} = 0.243$
- Figure 7.2.6 Planar Coanda Model Method of Characteristics Plot:
Slot 4.00 mm, Step 0.00 mm, $C_{po} = 0.324$
- Figure 7.2.7 Planar Coanda Model Method of Characteristics Plot:
Slot 6.00 mm, Step 0.00 mm, $C_{po} = 0.366$
- Figure 7.2.8 Planar Coanda Model Method of Characteristics Plot:
Slot 8.00 mm, Step 0.00 mm, $C_{po} = 0.425$
- Figure 7.2.9 Planar Coanda Model Method of Characteristics Plot:
Slot 2.00 mm, Step 0.00 mm, $C_{po} = 0.243$
- Figure 7.2.10 Planar Coanda Model Method of Characteristics Plot:
Slot 2.00 mm, Step 0.00 mm, $C_{po} = 0.176$
- Figure 7.2.11 Planar Coanda Model Method of Characteristics Plot:
Slot 4.00 mm, Step 0.00 mm, $C_{po} = 0.324$
- Figure 7.2.12 Planar Coanda Model Method of Characteristics Plot:
Slot 4.00 mm, Step 0.00 mm, $C_{po} = 0.256$
- Figure 7.2.13 Planar Coanda Model Method of Characteristics Plot:
Slot 6.00 mm, Step 0.00 mm, $C_{po} = 0.366$
- Figure 7.2.14 Planar Coanda Model Method of Characteristics Plot:
Slot 6.00 mm, Step 0.00 mm, $C_{po} = 0.330$
- Figure 7.2.15 Planar Coanda Model Method of Characteristics Plot:
Slot 4.00 mm, Step 1.50 mm, $C_{po} = 0.331$
- Figure 7.2.16 Planar Coanda Model Method of Characteristics Plot:
Slot 4.00 mm, Step 1.50 mm, $C_{po} = 0.331$
- Figure 7.2.17 Planar Coanda Model Method of Characteristics Plot:
Slot 4.00 mm, Step 1.50 mm, $C_{po} = 0.331$
- Figure 7.2.18 Planar Coanda Model Method of Characteristics Plot:
Slot 4.00 mm, Step 1.50 mm, $C_{po} = 0.212$
- Figure 7.2.19 Planar Coanda Model Method of Characteristics Plot:
Slot 2.00 mm, Step 0.00 mm, $C_{po} = 0.258$
- Figure 7.2.20 Planar Coanda Model Method of Characteristics Plot:
Slot 2.00 mm, Step 0.00 mm, $C_{po} = 0.243$
- Figure 7.2.21 Planar Coanda Model Method of Characteristics Plot:
Slot 2.00 mm, Step 0.00 mm, $C_{po} = 0.176$
- Figure 7.2.22 Planar Coanda Model Method of Characteristics Plot:
Slot 4.00 mm, Step 0.00 mm, $C_{po} = 0.355$
- Figure 7.2.23 Planar Coanda Model Method of Characteristics Plot:
Slot 4.00 mm, Step 0.00 mm, $C_{po} = 0.324$
- Figure 7.2.24 Planar Coanda Model Method of Characteristics Plot:
Slot 4.00 mm, Step 0.00 mm, $C_{po} = 0.324$
- Figure 7.2.25 Planar Coanda Model Method of Characteristics Plot:
Slot 4.00 mm, Step 0.00 mm, $C_{po} = 0.277$
- Figure 7.2.26 Planar Coanda Model Method of Characteristics Plot:
Slot 4.00 mm, Step 0.00 mm, $C_{po} = 0.256$
- Figure 7.2.27 Planar Coanda Model Method of Characteristics Plot:
Slot 6.00 mm, Step 0.00 mm, $C_{po} = 0.366$

- Figure 7.2.28 Planar Coanda Model Method of Characteristics Plot:
Slot 6.00 mm, Step 0.00 mm, $C_{po} = 0.343$
- Figure 7.2.29 Planar Coanda Model Method of Characteristics Plot:
Slot 6.00 mm, Step 0.00 mm, $C_{po} = 0.330$
- Figure 7.2.30 Planar Coanda Model Method of Characteristics Plot:
Slot 8.00 mm, Step 0.00 mm, $C_{po} = 0.425$
- Figure 7.2.31 Planar Coanda Model Method of Characteristics Plot:
Slot 8.00 mm, Step 0.00 mm, $C_{po} = 0.391$
- Figure 8.1.1 Axisymmetric Coanda Model Breakaway Performance
- Figure 8.1.2 Axisymmetric Coanda Model Reversion Performance
- Figure 8.1.3 Axisymmetric Coanda Model 2.55mm Slot Breakaway/Reversion Behaviour
- Figure 8.1.3 Planar Coanda Model Partial Reversion Behaviour
- Figure 8.1.4 Planar Coanda Model Breakaway/Reversion Behaviour
- Figure 8.1.5 Axisymmetric Coanda Model Experimental Surface Pressures:
Slot 1.67 mm, Step 0.00 mm
- Figure 8.1.6 Axisymmetric Coanda Model Experimental Surface Pressures:
Slot 1.67 mm, Step 1.25 mm
- Figure 8.1.7 Axisymmetric Coanda Model Experimental Surface Pressures:
Slot 1.67 mm, Step 3.13 mm
- Figure 8.1.8 Axisymmetric Coanda Model Experimental Surface Pressures:
Slot 3.33 mm, Step 0.00 mm
- Figure 8.1.9 Axisymmetric Coanda Model Experimental Surface Pressures:
Slot 3.33 mm, Step 0.00 mm
- Figure 8.1.10 Axisymmetric Coanda Model Experimental Surface Pressures:
Slot 3.33 mm, Step 1.25 mm
- Figure 8.1.11 Axisymmetric Coanda Model Experimental Surface Pressures:
Slot 3.33 mm, Step 3.13 mm
- Figure 8.1.12 Axisymmetric Coanda Model Experimental Surface Pressures:
Slot 5.00 mm, Step 0.00 mm
- Figure 8.1.13 Axisymmetric Coanda Model Experimental Surface Pressures:
Slot 5.00 mm, Step 0.00 mm
- Figure 8.1.14 Axisymmetric Coanda Model Experimental Surface Pressures:
Slot 5.00 mm, Step 1.25 mm
- Figure 8.1.15 Axisymmetric Coanda Model Experimental Surface Pressures:
Slot 5.00 mm, Step 3.13 mm
- Figure 8.1.16 Axisymmetric Coanda Model Experimental Surface Pressures:
Slot 2.54 mm, Step 1.25 mm
- Figure 8.1.17 Axisymmetric Coanda Model Experimental Surface Pressures:
Slot 2.54 mm, Step 1.25 mm

- Figure 8.2.1 Axisymmetric Coanda Model Base Pressures: Slot 1.67 mm
- Figure 8.2.2 Axisymmetric Coanda Model Base Pressures: Slot 2.54 mm
- Figure 8.2.3 Axisymmetric Coanda Model Base Pressures: Slot 3.33 mm
- Figure 8.2.4 Axisymmetric Coanda Model Base Pressures: Slot 5.00 mm
- Figure 8.2.5 Axisymmetric Coanda Model Method of Characteristics Plot:
Slot 3.33.00 mm, Step 0.00 mm, $C_{po} = 0.174$
- Figure 8.2.6 Axisymmetric Coanda Model Method of Characteristics Plot:
Slot 1.67.00 mm, Step 0.00 mm, $C_{po} = 0.202$
- Figure 8.2.7 Axisymmetric Coanda Model Method of Characteristics Plot:
Slot 1.67.00 mm, Step 0.00 mm, $C_{po} = 0.124$
- Figure 8.2.8 Axisymmetric Coanda Model Method of Characteristics Plot:
Slot 3.33.00 mm, Step 0.00 mm, $C_{po} = 0.265$
- Figure 8.2.9 Axisymmetric Coanda Model Method of Characteristics Plot:
Slot 3.33.00 mm, Step 0.00 mm, $C_{po} = 0.265$
- Figure 8.2.10 Axisymmetric Coanda Model Method of Characteristics Plot:
Slot 3.33.00 mm, Step 0.00 mm, $C_{po} = 0.233$
- Figure 8.2.11 Axisymmetric Coanda Model Method of Characteristics Plot:
Slot 3.33.00 mm, Step 0.00 mm, $C_{po} = 0.174$
- Figure 8.2.12 Axisymmetric Coanda Model Method of Characteristics Plot:
Slot 5.00.00 mm, Step 0.00 mm, $C_{po} = 0.225$
- Figure 8.2.13 Axisymmetric Coanda Model Method of Characteristics Plot:
Slot 2.54.00 mm, Step 1.25 mm, $C_{po} = 0.163$
- Figure 8.2.14 Axisymmetric Coanda Model Method of Characteristics Plot:
Slot 2.54.00 mm, Step 1.25 mm, $C_{po} = 0.125$
- Figure 8.2.15 Axisymmetric Coanda Model Method of Characteristics Plot:
Slot 1.67.00 mm, Step 0.00 mm, $C_{po} = 0.202$
- Figure 8.2.16 Axisymmetric Coanda Model Method of Characteristics Plot:
Slot 1.67.00 mm, Step 0.00 mm, $C_{po} = 0.124$
- Figure 8.2.17 Axisymmetric Coanda Model Method of Characteristics Plot:
Slot 3.33.00 mm, Step 0.00 mm, $C_{po} = 0.233$
- Figure 8.2.18 Axisymmetric Coanda Model Method of Characteristics Plot:
Slot 3.33.00 mm, Step 0.00 mm, $C_{po} = 0.174$
- Figure 8.2.19 Axisymmetric Coanda Model Method of Characteristics Plot:
Slot 5.00.00 mm, Step 0.00 mm, $C_{po} = 0.314$
- Figure 8.2.20 Axisymmetric Coanda Model Method of Characteristics Plot:
Slot 5.00.00 mm, Step 0.00 mm, $C_{po} = 0.225$
- Figure 8.2.21 Axisymmetric Coanda Model Method of Characteristics Plot:
Slot 2.54.00 mm, Step 1.25 mm, $C_{po} = 0.125$
- Figure 8.2.22 Axisymmetric Coanda Model Method of Characteristics Plot:
Slot 2.54.00 mm, Step 1.25 mm, $C_{po} = 0.125$
- Figure 8.2.23 Axisymmetric Coanda Model Method of Characteristics Plot:
Slot 6.65.00 mm, Step 0.55 mm, $C_{po} = 0.252$
- Figure 8.2.24 Axisymmetric Coanda Model Method of Characteristics Plot:
Slot 6.65.00 mm, Step 3.60 mm, $C_{po} = 0.184$

List of Plates

- Plate 1a Planar Coanda Model Shadowgraph:
Slot 2.00 mm, Step 0.00 mm, $C_{po} = 0.176$
- Plate 1b Planar Coanda Model Shadowgraph:
Slot 2.00 mm, Step 1.50 mm, $C_{po} = 0.124$
- Plate 2a Planar Coanda Model Interferometry Fringes:
Slot 4.00 mm, Step 0.00 mm, $C_{po} = 0.000$
- Plate 2b Planar Coanda Model Interferometry Fringes:
Slot 4.00 mm, Step 0.00 mm, $C_{po} = 0.488$
- Plate 3a Planar Coanda Model Shadowgraph:
Slot 4.00 mm, Step 0.00 mm, $C_{po} = 0.176$
- Plate 3b Planar Coanda Model Spark Schlieren: Vertical Knife Edge
Slot 4.00 mm, Step 0.00 mm, $C_{po} = 0.256$
- Plate 4a Planar Coanda Model Surface Flow Visualisation:
Slot 4.00 mm, Step 0.00 mm, $C_{po} = 0.324$
- Plate 4b Planar Coanda Model Surface Flow Visualisation:
Slot 4.00 mm, Step 0.00 mm, $C_{po} = 0.256$
- Plate 5a Planar Coanda Model Interferometry Fringes:
Slot 4.00 mm, Step 0.00 mm, $C_{po} = 0.312$
- Plate 5b Planar Coanda Model Interferometry Fringes:
Slot 4.00 mm, Step 1.50 mm, $C_{po} = 0.331$
- Plate 6a Planar Coanda Model Surface Flow Visualisation:
Slot 4.00 mm, Step 1.50 mm, $C_{po} = 0.331$
- Plate 6b Planar Coanda Model Surface Flow Visualisation:
Slot 4.00 mm, Step 1.50 mm, $C_{po} = 0.256$
- Plate 7a Planar Coanda Model Schlieren: Horizontal Knife Edge
Slot 4.00 mm, Step 1.50 mm, $C_{po} = 0.212$
- Plate 7b Planar Coanda Model Schlieren: Vertical Knife Edge
Slot 4.00 mm, Step 2.55 mm, $C_{po} = 0.205$
- Plate 8a Planar Coanda Model Shadowgraph:
Slot 4.00 mm, Step 3.76 mm, $C_{po} = 0.228$

- Plate 8b Planar Coanda Model Spark Schlieren: Vertical Knife Edge
Slot 4.00 mm, Step 3.76 mm, $C_{po} = 0.191$
- Plate 9a Planar Coanda Model Schlieren: Vertical Knife Edge
Slot 6.00 mm, Step 1.50 mm, $C_{po} = 0.290$
- Plate 9b Planar Coanda Model Spark Schlieren: Vertical Knife Edge
Slot 6.00 mm, Step 3.75 mm, $C_{po} = 0.315$
- Plate 10a Planar Coanda Model Schlieren: Horizontal Knife Edge
Slot 8.00 mm, Step 1.49 mm, $C_{po} = 0.359$
- Plate 10b Axisymmetric Coanda Model Schlieren: Horizontal Knife Edge
Slot 5.00 mm, Step 1.25 mm, $C_{po} = 0.207$
- Plate 11a Axisymmetric Coanda Model Schlieren: Horizontal Knife Edge
Slot 1.67 mm, Step 0.00 mm, $C_{po} = 0.124$
- Plate 11b Axisymmetric Coanda Model Schlieren: Vertical Knife Edge
Slot 1.67 mm, Step 1.25 mm, $C_{po} = 0.105$
- Plate 12a Axisymmetric Coanda Model Spark Schlieren: Horizontal Knife Edge
Slot 2.54 mm, Step 1.25 mm, $C_{po} = 0.125$
- Plate 12b Axisymmetric Coanda Model Schlieren: Horizontal Knife Edge
Slot 3.33 mm, Step 0.00 mm, $C_{po} = 0.265$
- Plate 13a Axisymmetric Coanda Model Surface Flow Visualisation:
Slot 2.54 mm, Step 1.25 mm, $C_{po} = 0.125$
- Plate 13b Axisymmetric Coanda Model Surface Flow Visualisation:
Slot 3.33 mm, Step 0.00 mm, $C_{po} = 0.174$
- Plate 14a Axisymmetric Coanda Model Spark Schlieren: Horizontal Knife Edge
Slot 3.33 mm, Step 0.00 mm, $C_{po} = 0.174$
- Plate 14b Axisymmetric Coanda Model Schlieren: Vertical Knife Edge
Slot 3.33 mm, Step 0.00 mm, $C_{po} = 0.243$
- Plate 15a Axisymmetric Coanda Model Surface Flow Visualisation:
Slot 3.33 mm, Step 1.25 mm, $C_{po} = 0.209$
- Plate 15b Axisymmetric Coanda Model Surface Flow Visualisation:
Slot 3.33 mm, Step 1.25 mm, $C_{po} = 0.174$
- Plate 16a Axisymmetric Coanda Model Schlieren: Vertical Knife Edge
Slot 3.33 mm, Step 1.25 mm, $C_{po} = 0.157$
- Plate 16b Axisymmetric Coanda Model Spark Schlieren: Vertical Knife Edge
Slot 3.33 mm, Step 3.13 mm, $C_{po} = 0.159$
- Plate 17a Axisymmetric Coanda Model Schlieren: Vertical Knife Edge
Slot 3.33 mm, Step 1.25 mm, $C_{po} = 0.157$
- Plate 17b Axisymmetric Coanda Model Shadowgraph:
Slot 3.33 mm, Step 3.13 mm, $C_{po} = 0.159$

List of Symbols

VARIABLES

a	sonic speed
A°	mean square of sonic speed on MOC streamline
C_τ	shear stress coefficient
C_D	dissipation coefficient
C_f	skin friction coefficient
C_p	surface pressure coefficient $\equiv (p - p_{atm})/(p_* - p_{atm})$
C_{pb}	base pressure coefficient $\equiv (p_b - p_{atm})/(p_* - p_{atm})$
C_{po}	driving pressure coefficient $\equiv p_{atm}/p_*$
e	strain rate
H	shape factor
H^*	kinetic energy shape parameter
H_0	empirical kinematic shape parameter coefficient
H_k	kinematic shape parameter
K_{gd}	Gladstone-Dale constant
L	length scale
\dot{m}_e	transpiration massflow
M	Mach number
n	normal coordinate
p	static pressure
$p(s, 0)$	surface static pressure distribution
$p(s, \delta)$	boundary layer edge static pressure distribution
Δp	pressure fluctuation
q	dynamic pressure
Q	coefficient for MOC pressure differential
r	radius
R°	mean momentum on MOC streamline
\mathcal{R}	radius of curvature
Re_δ	momentum thickness Reynolds' number
s	streamwise coordinate
S	coefficient for MOC distance differential
$S'(x, y)$	discrete fringe shift field

u	velocity component in s , x or ξ directions
U	velocity component in s , x or ξ directions (boundary layer)
v	velocity component in n , y or η directions
V	flow speed
x	cartesian coordinate (roughly streamwise)
y	cartesian coordinate (roughly normal to stream)
Δz_{ws}	working section depth
α	Mach angle
β	shock angle
δ	boundary layer velocity thickness
δ^*	boundary layer displacement thickness
δ^s	shock stand-off thickness
η	transformed normal coordinate
γ	isentropic coefficient
Λ	Pohlhausen pressure gradient parameter
λ_{HeNe}	laser wavelength
λ	flow line gradient
∇	axisymmetric exponent = $\begin{cases} 0 & \text{in planar geometry;} \\ 1 & \text{in axisymmetric geometry} \end{cases}$
ν	kinematic viscosity
ψ	stream function
ρ	density
ρ_{ref}	no-flow reference density
$\rho'(x, y)$	discrete density field
ϑ	boundary layer momentum thickness
θ	flow angle
ξ	transformed streamwise coordinate
$\Delta\xi$	streamwise increment
ζ	damping coefficient

SUPERSCRIPTS

+	left-running characteristic
-	right-running characteristic
\pm	either left- or right-running characteristic
12	solution line
o	streamline
$s+$	left-running shock
$s-$	right-running shock

SUBSCRIPTS

+	left-running characteristic
-	right-running characteristic
1, 2, 3, 4	discrete solution points
*	stagnation
±	either left- or right-running characteristic
∞	free stream
<i>atm</i>	atmospheric
<i>act</i>	net solution
<i>e</i>	boundary layer edge
<i>e</i> ∞	shear layer edge free stream
<i>inv</i>	inviscid solution
<i>mat</i>	matching line
<i>o</i>	streamline
<i>visc</i>	viscous solution
<i>T</i>	conjugate (M.C Coefficient)

Declarations

No material in this thesis has been previously submitted for a degree at the University of Durham or any other University. The thesis reports individual research carried out by the author.

The copyright of this thesis rests with the author. No quotation from it should be published without his prior written consent and information derived from it should be acknowledged.

set in 12pt Computer Modern Roman
© MCMXCI

Acknowledgements

The author would like to express his gratitude to Mr. R. Mand, Mr. M. Page, Mr. I. Glass, Mr. B. Blackburn, Mr. B. Scurr, Mr. T. Brown, Mr. W. Roscamp and all the other staff of the Engineering Department at Durham who helped in the provision and construction of the experimental equipment.

Thanks are due to Dr. D. Edwards and his team at British Petroleum Research for enabling the full-scale tests to go ahead, as well as for general financial and practical support during the project. Mr. S. Allum of Kaldair Ltd. also deserves thanks for providing copious data on the INDAIR flare.

Useful contributions of literature and other information were made by Dr. P.W. Carpenter and his students, formerly of Exeter University. This section would be incomplete without an expression of appreciation for the my supervisor, Dr. D.G. Gregory-Smith, for his unfailing patience and support during the project.

for Sally

οὔτοι ἀπ' ἀρχῆς πάντα θεοὶ θνητοῖσ' ὑπέδειξαν,
ἀλλὰ χρόνῳ ζητοῦντες ἐφευρίσκουσιν ἄμεινον.
ταῦτα δεδοξάσθω μὲν εἰκότα τοῖς ἐτύμοισι ...

Xenophanes of Colophon

*Not from the start was knowledge revealed to mortals,
but in time, by inquiring, they make better discoveries.*

Let these things be accepted as resembling the truth ...

1 INTRODUCTORY REMARKS

1.1 RESEARCH MOTIVATION

1.1.1 THE INDAIR FLARE

The industrial impetus for this research programme and for the current project stems from the development and manufacturing of high pressure gas flares for oil production platforms by British Petroleum International plc and its various subsidiary companies. The potential of the Coanda effect for this application was first identified in 1967 and various forms of burner geometry were then proposed for testing (see figure 1.1). One practical consequence of those proposals was the INDAIR flare, described by Wilkins *et alia*¹⁹⁷⁷. The main feature of this type of flare is its ability to burn large volumes of high pressure gas without smoke by using the intensification of entrainment induced by the Coanda effect, as confirmed by Carpenter¹⁹⁷⁸. A subsidiary feature is that the flame issuing from the flare is exceptionally stable, with respect to both crosswinds and ignition. In combination with the low flame radiation, this permits shorter (and thus cheaper) support structures.



Certain fortuitous advantages arising from the fluid dynamics have been found in the INDAIR. The fuel gas jet mixes with air in a region away from the flare tip, producing a flame thermally isolated from the flare structure, in contrast to conventional pipe flares, thus permitting the use of cheaper materials. In addition to this, the underexpanded jet produces a shock cell structure which atomises liquid droplets carried in the gas stream. Since these flares are specified for emergency duty, this is an important feature in reducing concern over the prospect of 'flaming rain', which can occur in other types of flare with liquid carry-over.

Given the above advantages, it is natural to ask why these flares have not completely replaced other types. Firstly, the 'tulip' form of the flare tip presents a complex and therefore an expensive manufacturing task. Secondly, the shock cell structure of the flare flowfield produces noise levels which create difficulties in meeting environmental standards in the workplace. The maximum flow performance (directly linked to pressure in a choked nozzle) for a given flare is restricted by the phenomenon of jet breakaway, in which the flare tulip no longer steers the fuel gas jet upwards. This causes a marked reduction in entrainment and the loss of film cooling. More seriously, the uncontrolled flame may also impinge on other structures in the vicinity of the flare. Since the consequences of this condition in operation would be catastrophic, large safety margins have to be applied to the design, with corresponding penalties in cost. Thirdly, the current flare design requires a minimum quantity of high pressure gas, in order to eliminate flame contact which would otherwise erode the flare tip, and to ensure that adequate air is entrained for smokeless

combustion. This minimum flow increases in proportion to the size of the flare tulip. As both maximum and minimum flow limits are set by the flare size, the turndown ratio of the device cannot be independently altered, thus restricting the use of the flare in current installations and hindering wider application of the technology.

So far, the design of the INDAIR has proceeded by heuristic methods, and the potential of these for producing further commercially viable progress has been largely exhausted. For design optimisation of entrainment, breakaway, turndown ratio, manufacturing simplification and noise suppression measures, a less qualitative approach is now required.

1.1.2 HIGH SPEED JET FLOWS

There is scientific interest in high speed jet flows for applications other than flares, principally in the aerospace industry, where typical flow velocities are now of an order which makes applications of such jets a viable proposition. One major area of aeronautical interest is the application of slot blowing to the control of boundary layer separation and the generation of high-lift surfaces. The advent of supersonic and hypersonic transport has also provided motivation for studies of high-speed flows which have strong effects on vehicle heating.

1.2 PROJECT OBJECTIVES

The research programme into Coanda flares at Durham University was initiated, in association with B.P. International plc, to advance knowledge of

the fluid dynamics of INDAIR flares used for gas disposal. A parallel research programme under Dr. P.W. Carpenter at Exeter University is concerned with the noise suppression aspect of the flare. As mentioned in section 1.1.1 above, the major industrial motivation behind the current research project is to advance towards a predictive design method for development and optimisation purposes.

Academically, the motivation for the project is to provide a contribution to the understanding of curved wall jet flows. Previous work at Durham University has been divided into two main projects: low speed investigations of turbulence structure in the flare, reported by Morrison & Gregory-Smith¹⁹⁸⁴, and high speed studies, reported by Gilchrist¹⁹⁸⁵. The current project is a direct continuation of the latter, which developed experimental apparatus for the investigation of the high speed jet, produced results from that equipment and also began the development of prediction methods.

On the experimental side, the current project had four main objectives. The first of these was to upgrade the interferometer to cope with high-speed flows. Secondly, experiments upon a planar, two-dimensional model with a base step were planned, in order to model the real flares already modified in this way. Thirdly, investigations were planned for an axisymmetric model directly analogous to the full-size flare to ensure that any data and computational work can be applied to INDAIR flare design. The final experimental objective was to perform tests on real flare operation to establish conclusive comparability between the research work and an industrial environment.

The theoretical objectives were, firstly, to gain an understanding of the fluid dynamic behaviour of the jet, and, secondly, to use this understanding in the extension of computational methods towards the prediction of jet breakaway. It was envisaged that progress in this area should be of more general application to high-speed jets.

1.3 THESIS STRUCTURE

1.3.1 NOMENCLATURE

The major phenomenon of interest in the flare fluid dynamics for the current project is the gross detachment of the jet from the flare surface. Many workers have applied the terms 'separation' and 'reattachment' to the description of similar behaviour. However, separation and reattachment of the jet flow to the flare surface was shown to occur without gross alteration in the jet deflection, and terminology is therefore required to draw a distinction between detailed flow features and flow modes. Thus, in the text which follows, *separation* and *reattachment* are reserved exclusively for the detailed features of the flow, whilst *breakaway* and *reversion* are used for the analogous gross flow behaviour.

1.3.2 LAYOUT OF THE CHAPTERS

Some of the chapter divisions may appear rather arbitrary, but detailed consideration has been given to their choice. The following brief summary of the selection is given in order to assist the reader. Chapter 2 is a survey of the background of published material relevant to the project in terms of

the fluid dynamic phenomena and computational methods. Chapter 3 focusses on the choice between the available methods, whilst Chapter 4 is reserved for the description of the computational methods used. Chapter 5 describes the development of the apparatus, leaving the description of its use to Chapter 6.

Some thought was given as to whether results should be divided by a computational/experimental split or by a planar/axisymmetric split. The latter was finally adopted in Chapters 7 and 8, since it was decided that comparability between computational and experimental work for each type of geometry should take precedence. Accordingly, some of the comparison between geometry variants was left for Chapter 9, which also draws together other issues arising from the work. Finally, Chapter 10 provides a concise statement of the project achievements.

2 LITERATURE BACKGROUND

2.1 COANDA FLARES

2.1.1 THE COANDA EFFECT

The phenomenon in which a jet of fluid attaches to a curved wall has been studied for a considerable period, for instance Young's work, mentioned in Pritchard¹⁹⁵⁷. Metral & Zerner¹⁹⁴⁸ provide a review of other studies and applications of the Coanda Effect. The Effect can be further sub-divided into:

- (a) An inviscid irrotational effect whereby the streamline pattern induces sufficiently low pressure at the wall to attach the jet (called the 'Teapot Effect' by Keller¹⁹⁵⁷).
- (b) A turbulent mixing effect whereby a jet close to a wall sets up a recirculation zone induced by the mixing layer, which in turn produces a low pressure attracting the jet to the wall, which intensifies the recirculation if the jet is close enough to the wall. This feedback process has been called the 'Chilowsky Effect' by Bradshaw¹⁹⁷³.

(c) An intensified mixing effect at the jet outer edge, caused by the influence on the turbulence of the bending of the jet by the wall, has also been associated with the term 'Coanda Effect' (although this seems to be more a consequence of (a) and (b) above than a mechanism in its own right).

A considerable number of studies have been completed on the low-speed wall jet (e.g. Fekete¹⁹⁶³, Newman *et alia*¹⁹⁷², Morrison¹⁹⁸⁴), of which Gilchrist¹⁹⁸⁵ gives a comprehensive review. It is not proposed to duplicate that review here. Supersonic studies analogous to the present case are much less common, much of the work coming from previous projects in the current research program associated with British Petroleum. However Roderick¹⁹⁶¹ presents results for a supersonic wall jet in which there is clearly a wave structure similar to that of the present work. More recently, a series of papers by Dash and co-workers has been published concerning the curved wall jet flow configuration (e.g. Dash & Wolf¹⁹⁸⁴).

Many studies (for instance Bourque & Newman¹⁹⁶⁰, Fernholz¹⁹⁶⁷, Gregory-Smith & Robinson¹⁹⁸² and El-TaHER¹⁹⁸³) have shown significant hysteresis zones in the operation of subsonic wall jets in various configurations. These zones define initial flow conditions for which the jet may be either detached from or attached to the wall, depending on the history of the flow establishment. Gilchrist^{op. cit.} confirmed that this behaviour also takes place in supersonic Coanda wall jets. It is this phenomenon in particular that is the focus of the current work.

The Coanda Effect using subsonic wall jets has found many applications. McGlaughlin & Taft¹⁹⁶⁷ used separation of a Coanda Effect jet induced by

surface heating to produce an electro-*to*-fluidic transducer. Metral & Zerner¹⁹⁴⁸ cover a number of instances where Coanda surfaces were used to enhance exhaust manifold discharge performance. Wille & Fernholz¹⁹⁶⁵ also describe many subsonic applications of the Coanda Effect, one particularly novel example being the design of turbine blading using the low pressure generated by the attached jet to provide the motive force, thereby leaving one side of the blade 'open' for cooling. Newman¹⁹⁶⁹ includes jet redirection in air cushion vehicles amongst the applications for the Coanda Effect.

The current work is, however, more applicable to the use of the effect for vectoring aero-engine thrust mentioned by Fernholz¹⁹⁶⁶. More recently, there has been interest in control of the boundary layers on airfoil surfaces by wall jets in order to delay or limit the loss of lift experienced at stalling angles of attack. The application of the Effect to parkable rotary wing aircraft is mentioned by Keshavan¹⁹⁷⁵, and Dvorak & Choi¹⁹⁸¹ present further work in this area, where the lift at high vehicle speeds is maintained by low surface pressure generated by an attached jet flowing over the lifting rotor. Clearly, the investigation of the mechanism of separation in the supersonic case is highly relevant to these potential applications.

2.1.2 THE FLARE FLOWFIELD

2.1.2.1 General Structure

The picture emerging from the progress of computational fluid dynamics to date is that no method exists that is truly applicable to all cases (Anderson¹⁹⁸⁶). Consequently, some idea of the structure of the flowfield to be modelled is

required in order to choose the simulation technique. The main features of the flare flowfield set out below, are derived from the results of Gilchrist¹⁹⁸⁵, Green¹⁹⁸⁷ and current investigations (described in detail in Chapters 7 and 8) and are similar to those identified by Catalano, Morton & Humphris¹⁹⁷⁷, namely:

- (a) A region of flow establishment, where an inviscid core is flanked by a growing wall boundary layer and an outer mixing layer. Wille & Fernholz¹⁹⁶⁵ point out that this region is likely to be significant only where the jet is thick with respect to the radius of curvature. Gilchrist's¹⁹⁸⁵ planar results show that the potential core is quite extensive. Since the phenomenon of breakaway, which is the main concern of the present work, is thought to be largely determined by conditions within and adjacent to the core, it and the wall shear layer are the primary focusses of the current work. Although this is less likely to be true of the axisymmetric flare, calculation of the initial region will still be a prerequisite for estimates of the fully developed flow zone.
- (b) A viscous flow region where the inviscid core has been completely eliminated by the growth of the shear layers on the inner and outer boundaries of the jet.

Figure 2.1 gives a qualitative outline of the flowfield and the main features which it contains. The typical jet in flare operation is underexpanded at the nozzle exit, giving rise to a wave system and consequent shock development. The step produces an initial recirculation zone and a shock wave, whilst the reattaching mixing layer causes a significant growth of the initial boundary layer on the Coanda surface compared to the unstepped flare case.

2.1.2.2 Boundary Layer and Separation

Analysis of the flowfield of a shock-wave/boundary layer interaction is complicated by the presence of adjacent subsonic and supersonic flow regions in the boundary layer. The shock is refracted in the viscous supersonic region and reflected at the sonic boundary. Because the subsonic layer cannot undergo a localised pressure jump, it begins to thicken upstream of the shock impingement, spreading out the pressure rise. This in turn affects the pressure and flow pattern in the supersonic layer and adjacent inviscid flow by turning them away from the wall. Figure 2.2 shows schematics for normal and oblique shocks with and without separation of the boundary layer. Unless the shock is quite weak, the intense adverse pressure gradient caused by its impingement on the boundary layer will lead to a more or less localised separation, depending on the pressure gradient before and after the shock affected zone. The supersonic flow is very sensitive to changes in flow angle caused by the boundary layer response, thus giving rise to 'strong' interaction, which can result in substantial modification of the flowfield outside the boundary layer. These modifications feed back into the boundary layer in a non-linear fashion (i.e. unpredictable by superposition), and thus produce great sensitivity of the final flow pattern to the incoming boundary-layer conditions.

Green¹⁹⁷⁰ points out, in his comprehensive review article, that this sensitivity generally makes the prediction of separation bubble size and reattachment extremely difficult where precise knowledge of the boundary layer structure is absent. However, he also presents the well-known suggestion that where the boundary layer separation zone is large enough, the separation bubble is

governed only by the downstream pressure level and by the *incoming* boundary layer and not by the details of the flow separation. This 'free interaction' hypothesis has proved useful for separation zone sizes of engineering interest, although Green points out that even incipient separation may have a considerable effect on the entropy loss through the shock system. Sirieix¹⁹⁷⁵ also recommends this concept by pointing out that data for separation in widely differing situations can be successfully collapsed into one relationship by its use.

Adamson & Messiter¹⁹⁸⁰ also detail mechanisms of shock penetration and diffusion in boundary layers in their review. They present evidence for the more localised effect of a shock wave on a turbulent boundary layer, due to its greater ability to overcome adverse pressure gradients. They examine the applicability of various turbulence models, but conclude that even two-equation formulations give only fair correspondence to experimental evidence. Rose¹⁹⁷⁴ presents results showing the turbulence intensity increase caused by both shock waves and adverse pressure gradients. Samimy, Petrie & Addy¹⁹⁸⁶ have shown that, once separated, the boundary layer quickly assumes a turbulent mixing layer form and this serves to determine the reattachment process. They also found that in supersonic flow the layer re-establishes boundary layer form after reattachment much more quickly than in subsonic flow, and so the inner shear layer in the INDAIR is likely to be characterised by rapid transitions in form.

2.1.2.3 Pressure Gradient, Curvature and Divergence Effects

Unfortunately, the complexity of the actual boundary layer behaviour is not confined merely to shock interactions. Extra complications arise from curvature, divergence and bulk compression and expansion, all of which are present simultaneously in the INDAIR flare. In a laminar shear layer these will cause extra influences on both cross-stream and longitudinal pressure gradients. The turbulent case is further complicated by alterations in the turbulence structure. Bradshaw^{1975a} says that in complex shear layers the effects of extra rates of strain on the turbulence structure caused by flow complications are likely to be significant where the rate $e > \frac{\partial u/\partial n}{100}$. Furthermore, in a series of turbulent boundary layer investigations (Bradshaw¹⁹⁷⁴; Smits, Eaton & Bradshaw¹⁹⁷⁹; Smits, Young & Bradshaw¹⁹⁷⁹; Muck, Hoffman & Bradshaw¹⁹⁸⁵), it becomes apparent that considerable nonlinearity exists between such effects. The third of the above papers presents strong evidence for the generation of longitudinal vortices on walls with destabilising curvature and the persistence of these vortices downstream. Irwin & Arnot-Smith¹⁹⁷⁵ have also found that curvature produces much larger effects on the turbulence than would be produced by analogous streamwise acceleration. Bradshaw¹⁹⁶⁹ suggests that the curvature affects turbulence for $\mathcal{R}/\delta < 300$ and that this limit may be even greater in compressible flow. The work of Schofield¹⁹⁸⁵ reveals further non-linear effects which serve to increase separation zones where a boundary layer is subjected to both shock impingement and adverse pressure gradient.

Dash *et alia*¹⁹⁸³, in a case closely analogous to the INDAIR, point out that their use of overlapping viscous and inviscid computational domains

with turbulence modelling in the viscous calculation still fails to account for the shock wave/turbulence interaction. At present, understanding of this interaction is limited, so failure to account for it cannot be regarded as a criterion for the choice between simulation techniques. In fact, it appears that the general physical mechanisms of turbulence are not well understood, despite a considerable body of work (cf. Bradshaw's¹⁹⁷² bibliography of 600 *selected papers*), and, although the mathematics of chaotic behaviour have recently given further insights (Miles¹⁹⁸⁴), it appears that there are still considerable obstacles to be overcome before the physics of the phenomenon are accurately modelled.

2.1.2.4 Deviations from Steady Two-Dimensional Flow

The previous work in the programme by Gilchrist¹⁹⁸⁵ uses the approximation of steady two-dimensional flow for the flare jet. However, his planar work does show some evidence of side-wall interference. Although it may be acceptable to regard this as negligible where the jet is attached to the wall, it is difficult to be as confident about the effects on the separation bubbles.

Green¹⁹⁷⁰ points out that surface oil flow visualisation shows significant three-dimensionality in a shock separation and reattachment even though a survey of the incoming boundary layer reveals no departure from what is normally considered to be two-dimensionality. Guitton & Newman¹⁹⁷⁷, in their subsonic wall jet experiments, went to considerable lengths to eliminate cross-flows but, even so, obtained skin friction with a 15% difference from that calculated using the two-dimensional momentum equation (the most stringent

test generally applied). Recently, Liu & Squire¹⁹⁸⁸ have reported a shock-induced separation experiment on a curved wall, and again considerable 3D effects emerged.

In the axisymmetric case, wall interference is not present, but nevertheless 2D flow cannot be assumed automatically. Guitton & Newman¹⁹⁷⁷ offer an explanation for non-vortical cross-stream variations by arguing that thicker parts of the wall jet give rise to a smaller surface pressure than thinner parts and so fluid flows from thinner sections to thicker ones, thus amplifying the variation.

Benwell¹⁹⁸⁴ gives evidence for the presence of longitudinal surface structures, which he interprets as vortices, in the axisymmetric flare flowfield. None were observed in the planar model of Gilchrist¹⁹⁸⁵. However, in the planar work of Ramaprian & Shivaprasad¹⁹⁷⁷ on *concave* walls, where such vortices are expected, these were apparently suppressed by side wall effects (when compared with corresponding work by So & Mellor¹⁹⁷⁵). El-Hady & Verma¹⁹⁸⁴ present experimental evidence that this type of vortex generation also takes place in supersonic flows.

Although in the current case the wall curvature is convex and hence stabilising, the unstable streamline curvature at reattachment (as mentioned by Bourque & Newman¹⁹⁶⁰) may be causing vortical motion. Support for this hypothesis comes from the fact that vortices in INDAIR flares are observed only in the surface flow patterns subsequent to the end of the convex surface (after any jet reattachment). Schlieren photographs by Motallebi & Norbury¹⁹⁸¹

reveal considerable vortex shedding following a low supersonic reattachment. Schofield¹⁹⁸⁵ also found evidence for streamwise vortex generation by a shock-induced separation. In the light of such results, similar phenomena are expected in the axisymmetric flare model.

Inger¹⁹⁷⁵ gives evidence in a review paper for a lateral periodic disturbance downstream of a rear-step separation and reattachment. This disturbance features pairs of counter-rotating vortices with a lateral wavelength of $2\delta-4\delta$ centred at the boundary layer edge, which give rise to variations in surface pressure and skin friction between 10% and 25% of the mean values. Increasing Mach number, adverse pressure gradient and 'strong' interaction all have a significant effect on the scale of the disturbances. Two mechanisms are suggested: firstly, Taylor-Görtler instability in the concave curvature region at reattachment; secondly, amplification at reattachment of disturbances arising during the separation. Floryan¹⁹⁸⁹ suggests that Görtler instability can arise in nominally stabilising curvature if the velocity distribution in the shear layer is non-monotonic (as is found in thinly separated boundary layers on convex wall curvature). A notable feature of his analysis is that such instability is shown to be liable to create short wavelength vortices, similar to those observed by Green¹⁹⁸⁷.

Mehta¹⁹⁸⁸ used a laser doppler anemometer to make a detailed study of the effect of pre-existing streamwise vortices on axisymmetric supersonic separation. The net effect was to delay separation on both sides of the vortex but more strongly on the downwash. The separation bubble is also smaller

since the vortical motion promotes momentum interchange with the reversed flow. Such an effect will be beneficial for breakaway performance in the INDAIR case, especially if more than one separation zone is present.

Deviations from the modelling assumption of steady flow might also be present in the INDAIR flare. Havener & Radley¹⁹⁷⁴ detected 3D disturbances with a period less than $15\ \mu\text{s}$ at a flow separation and concluded that these must be a feature of the separation process. However, larger-scale periodic temporal disturbance of the flow is thought unlikely owing to Tanner's¹⁹⁷³ argument that the oscillatory behaviour sometimes observed in subsonic base flows appears not to occur in the supersonic case because such motion tends to require feedback far upstream (well before the separation point) and this is generally weaker or non-existent in supersonic flows.

2.1.2.5 Supersonic Base Flow

The paper by Tanner¹⁹⁷³ sets out the general features of a base flow. The separation of the boundary layer near or at the corner sets up a free shear layer which, if not already turbulent, very quickly undergoes transition. This produces intense mixing which drives a strong recirculation in the 'dead air' region, significantly lowering the pressure there. The flow is thereby attracted towards the lower wall, or centreline, in the case of a wake. When the shear layer reaches the end of the recirculation zone, a recompression takes place, and the layer experiences a change in structure towards boundary layer or symmetrical wake form, as appropriate. In supersonic flow, the recompression coalesces into a shock wave, and, if the base is formed by a

sharp corner, the turning of the flow at this corner can be represented as a centred expansion to a first approximation.

The mechanism above fails to account for one particular feature observed in actual supersonic base flows: the lip shock. Green¹⁹⁷⁰, amongst others, gives an explanation for the appearance of this shock. His argument suggests that the low pressure generated by recirculation in the base zone is communicated upstream of the step in the subsonic part of the boundary layer, giving a favourable pressure gradient and thus thinning the layer before the corner. Moreover, the lower level of the boundary layer (the laminar sub-layer of a turbulent boundary layer according to Alber & Lees¹⁹⁶⁸) attaches to the face of the step under the influence of the very strong favourable pressure gradient at the corner, but then separates almost immediately once into the base zone. The net effect of this gradient on the supersonic layers is that expansion begins ahead of the corner and continues for a short length afterwards as the outer layers attempt to follow the inner layers down the step face. A compression is then required to turn the flow as the sub-layer separates from the step face and this coalesces to form the lip shock. Alber & Lees give evidence that the free shear layer after this process is only $1/10^{\text{th}}$ of the thickness of the incoming boundary layer, which suggests that strong acceleration is present over a finite distance.

Weinbaum¹⁹⁶⁶ gives a detailed explanation of the mechanism and interaction of the subsonic and supersonic layers. He emphasises that, for separation from the step face, an adverse pressure gradient is required, which implies that

immediately adjacent to the corner the pressure must fall *below* the base pressure, leading to an initial overexpansion of the flow and, consequently, a recompression lip shock develops.

Although previous work by Gilchrist¹⁹⁸⁵ reveals the possibility that lip shocks were also present on the outer edge of the jet, the usefulness of the inviscid core calculation appears to be largely unaffected by their presence, and direct empirical modelling was not considered necessary. It is possible that lip shocks in the stepped and axisymmetric cases could be significantly stronger owing to the greater underexpansion, and both the current work and that of Parsons¹⁹⁸⁸ reveal lip shock structures in visualisation work.

2.1.2.6 The Mixing Layer

The outer mixing layer is not a primary concern of the current work, except for the extent to which it affects the demise of the potential core zone and thereby produces significant modification of the near-wall area. Gilchrist's¹⁹⁸⁵ inviscid solutions with prescribed wall pressure match the flow visualisation to a degree which suggests that the influence of the outer mixing layer on separation can be neglected to a first approximation. This may not be the case for the axisymmetric flare, where the potential core appears from the work of Green¹⁹⁸⁷ to be much shorter.

2.1.2.7 Real Flare Effects

The above description of the flare flowfield is based upon experimental work carried out on models using air for the jet (and, of course, for the

surroundings). In practice, the actual fuel gas has significantly different properties and some account must be taken of this in the modelling.

Further discrepancies arise owing to the fact that flame radiation causes heating of the jet, and, more particularly, of the flare tip (Carpenter¹⁹⁷⁸ quotes a typical temperature of 600 K). This is likely to cause earlier separation of the boundary layer. A full model of the combustion effects would pose considerable computational and experimental difficulties, and therefore further investigation in this direction has had to be curtailed in the current work. This curtailment is also partially justified by the fact that combustion does not actually take place until far downstream in the real flare.

Recent experimental work by Papamoschou & Roshko¹⁹⁸⁸ suggests that some account should be taken of the effect of the different densities of the atmosphere and the fuel gas in the outer mixing layer. However, the trend appears to be that the real situation, with the heavier gas at the lower speed (i.e. stationary), promotes more rapid entrainment than predicted by the single gas model, and thus a single fluid calculation should provide a conservative underestimate of breakaway performance, which is thought to improve with increased shear layer entrainment.

2.2 FLUID DYNAMIC COMPUTATION

2.2.1 NUMERICAL METHOD REQUIREMENTS

Gilchrist¹⁹⁸⁵ describes the development of a FORTRAN program implementing the Method of Characteristics (MOC) for a two-dimensional Coanda surface.

As implemented, the program calculates a supersonic, inviscid, irrotational shock-free jet over a circular arc surface. Hence, separation of the jet from the surface observed in laboratory models and industrial flares can only be incorporated by using empirical data. In spite of this, the algorithm provides a reasonable approximation to the jet in the supersonic part of the 'inviscid' core. However, the interpretation of the actual flare flowfield, derived above with the aid of experimental flow visualisation and measurement, reveals the existence of several strongly interactive phenomena. From the point of view of the project, which is concerned with jet separation, the most important of these appears to be boundary layer separation under the influence of steep adverse pressure gradients and of shock waves.

The INDAIR case would be a demanding test case for any method, given the complexity of the flowfield and the range of features it includes, most of which are still under research investigation in isolation. Green¹⁹⁸⁷ expresses the opinion that the flare flowfield is so complex that an accurate model is unlikely to be achieved, even by the most sophisticated techniques. Bradshaw^{1975a} holds the opinion that combinations of extra strain rates invalidate most current turbulence models. Dash *et alia*¹⁹⁸³ also suggest that the problem of accurately modelling the supersonic curved wall jet and its turbulence is a formidable one, and that compromises have to be made even with sophisticated methods. It therefore appears that accuracy will carry less weight than other

considerations, since any putative method of flow prediction is likely to have significant inaccuracy.

Since the principal purpose of developing a computational method is to permit design optimisation of the INDAIR flare, robustness to changes of geometry is required. Accuracy in the major parameters of the design would also be desirable, but, since it is unlikely that a new design would be approved for installation without experimental testing, it may be permissible for practical purposes to accept some approximation. Furthermore, in order to meet the required industrial safety margin, it would appear reasonable to establish the operating limit of any flare design to the lower point of the breakaway hysteresis zone. This may simplify the required analysis, since the experimental evidence points towards extensive separated zones as the hallmark of the hysteresis region. From the point of view of design improvement, therefore, a model which permits comparative analysis between alternatives with slight inaccuracy may be just as acceptable as a fully accurate one, particularly where significant advantages in costs are thereby obtained.

The use of optimisation methods in general, and automated ones in particular, makes computational efficiency a pre-requisite, and the limited time and manpower available to the current project also puts development time at a premium. A further consideration is that the method adopted should be readily transferable to the industrial sponsors. Clearly, this is unlikely to be achievable with a large and complex code unless that code is a proprietary product generally available, especially when considering software support.

The hierarchy of fluid flow modelling generally follows a quite clearly defined progression. The first stage correlates parameters of interest based on assumptions of flow similarity, this being applied normally when varying the size and/or operating conditions of a well characterised piece of fluid machinery according to requirements, usually over a somewhat restricted range. This method is currently applied to the specification process for INDAIR flares for particular duties, but is obviously unsuitable for redesign work.

The next stage is to break the flowfield down into various components which can be modelled without interaction to give an estimate of gross behaviour. For instance, an inviscid solution can be used to give a pressure distribution, and then combined with a check to confirm that adverse pressure gradients on flow walls are not strong enough to cause separation. This is also unsuitable for accurate computation of the interactions apparent in the Coanda flare, since extensive separation was found.

The third stage methods break the flowfield down into regions where some simplifications of the basic fluid dynamic equations apply, and these are then matched by iteration or relaxation of some sort until convergence to the boundary conditions is achieved. For practical engineering use, such techniques are probably the most accurate methods currently available for optimisation purposes at feasible commercial cost, although the development of computing technology is altering this situation rapidly.

The final stage of fluid flow modelling, or computational fluid dynamics (CFD), is composed of sophisticated models using various means to generate a

full flowfield solution from low-level empirical relationships such as turbulence modelling, entrainment modelling (for instance, Newman's method ¹⁹⁶⁹ for wall jet reattachment), and other 'general' simplifications of real fluid flow. Since current models for the essential phenomenon of turbulence suitable for computational use are far from being fully generalisable, they rely on empiricism, and so have a limited sphere of application. The final goal for the engineering of fluids would be to model all the physical processes directly, but at present this is beyond both computer power and theoretical knowledge. The choice which therefore falls to be made in modelling fluid flow is the balance between required accuracy, computational power and the range of applicability of the method.

2.2.2 INVISCID AND EMPIRICAL MODELS

As a preliminary technique for the INDAIR, given the degree of correspondence found by Gilchrist¹⁹⁸⁵ between the purely inviscid Method of Characteristics and the experimental results for attached and separated jets (with experimental edge pressure supplied in the latter case), some simple criteria for separation and reattachment phenomena, such as those of Sirieix¹⁹⁷⁵ or Alber *et alia*¹⁹⁷³, might well provide an acceptable engineering approximation for the breakaway phenomenon. Curle¹⁹⁷⁸ gives a complex criterion for separation derived from a multiple-deck matched asymptotic solution for a boundary layer. Dvorak & Choi¹⁹⁸¹ also found that purely inviscid theory was inadequate to predict the effect of a wall jet and that more sophisticated analysis was necessary, and

they applied the Pohlhausen separation criterion ($\Lambda = \frac{\delta^2}{\nu} \frac{\partial u}{\partial s} = -12$) for wall jet detachment.

The principal problem with separation criteria in general is that they predict separation only in regions of adverse pressure gradient, whereas the comparison between Gilchrist's attached jet modelling and the experimental data suggests that initial separation is followed by upstream movement of the separation into regions of *favourable* pressure gradient. Samimy, Petrie & Addy¹⁹⁸⁶ found an approximate value for the maximum reverse velocity of $0.2V_e$ in a compressible separated shear layer. This agrees reasonably well with the value of $0.16V_e$ quoted by Alber *et alia*¹⁹⁷³ and could be used for estimating the upstream influence of initial separation.

For predicting the actual breakaway point using the above criteria, inspection of the calculated jet shape could be used. However, the inaccuracy of a criterion based on separation prediction could limit the usefulness of this approach. Experimental results given later show a short region of favourable pressure gradient between separation bubbles which shrinks as breakaway is approached. This might also be used as an empirical criterion for breakaway.

Sirieix¹⁹⁷⁵, quoting results by Holden, gives typical pressure fluctuations at reattachment of $\Delta p/q = O(0.1)$ in shock-separated turbulent hypersonic boundary layers, giving up to a $\delta/3$ movement of the reattachment point. Muck, Andreopoulos & Dussauge¹⁹⁸⁸ have also reported unsteadiness and 3D effects in turbulent shock separation. Since breakaway appears to depend upon the absence of a 'sealing' favourable pressure gradient after the separation

bubble reattachment point, a fluctuation level could be used to set a minimum value of pressure decrease as a breakaway criterion.

The problem, however, is not to predict breakaway *per se*, but to establish the start of the hysteresis zone where jet breakaway is possible. This sets the operating limit for the flare since below this point the jet will revert after large disturbances, and the size of the hysteresis zone should ensure an adequate safety margin for transients. Since separation (followed by reattachment) in the INDAIR may be present before the lower limit of the hysteresis region is reached, separation detection alone is not an acceptable criterion for the upper limit of flare operation. Accordingly, a fully reliable prediction of an operating limit appears to require a more sophisticated analysis than is suggested in this section.

2.2.3 SOLUTIONS OF THE COMPLETE FLOWFIELD

The Navier-Stokes equations (NS) for fluid flow are based upon several fundamental assumptions. The first of these is that the fluid can be regarded as a continuum. Relativistic effects are excluded by specifying continuity of mass and preserving momentum in the absence of external forces. Empirical laws for the relationship between shear rates and viscous forces are added to complete the equation set. The equations can be formulated in a number of different ways (see Anderson¹⁹⁸⁶), which are mathematically equivalent but have different implications, both in terms of the geometry of the problem and of the numerical implementation. It should be stressed that solutions

for flowfields in different cases are generated by applying the NS to different boundary conditions.

As Stewartson¹⁹⁷⁴ points out, the NS equations are generally regarded as the correct macroscopic description of the flow of fluids, but the author is not aware of a justification of this view in cases where flow scales become comparable to those of molecular motion, such as inside shock waves. Accordingly, special treatment for such flows appears necessary *a priori*.

The mathematical form of the steady flow NS is elliptic (equivalent physically to every point in the flowfield influencing every other point), and solutions for this type of mathematical problem have concentrated on relaxation methods. However, by formulating the NS for unsteady flow, the set becomes parabolic in time (equivalent to a monotonic marching direction) and can then be advanced iteratively until a steady-state convergence is achieved. Alternatively, simplifications of the NS can be applied to make the set parabolic in a space dimension, giving a set known as the Parabolised Navier-Stokes equations or PNS, which are also referred to by some authors as the Reduced Navier-Stokes equations or RNS. There seems to be no general agreement as to exactly which simplifications these latter terms refer, but in every case some parts of the mathematical description of the flow are ignored as being negligible in the case to which they are applied. Hence, for the solutions to be valid, the corresponding physical quantities must be genuinely small with respect to the rest of the flow.

Solution of the NS for a particular case is usually approached by evaluating fluid properties at particular points in the flowfield. Integral representations of the equations are involved in the Finite Element Method (FEM) which uses small elements of space over which the changes in fluid properties are approximated by modelling functions. By covering the computational domain with a network of such elements, the functions can then be evaluated numerically in accordance with the NS to approximate the fluid dynamics. Experience with FEM suggests that it is particularly robust and adaptable and that it may be able to model flow using relatively coarse grids. The examples Connor & Brebbia¹⁹⁷⁶ give appear to vindicate this view.

However, computational effort per grid element is large, and the appearance of shock discontinuities in the flow may require a finer grid to minimise the inaccuracies caused by smearing the shock over a finite area of the grid, as mentioned by Wadia¹⁹⁷⁹. He also suggests that the stability may be adversely affected by a predominance of supersonic elements in the method (which, if true, clearly rules it out for the present work). Habashi & Hafez¹⁹⁸² confirm the existence of convergence problems with some types of FEM in transonic shock flows. Moreover, the programming of an FEM for CFD is especially complex, and only an externally written program would have been feasible within the time resources of the current project. Since no suitable FEM solver was available at Durham, an approach using this method was rejected. Also, Hall¹⁹⁸² points out that the development of FEM solvers, although progressing, is not yet adequate for embedded shock compressible flows. Elrafaee *et alia*¹⁹⁸² propose a scheme whereby the whole domain integral representation of the NS

is approximated. However, this requires conformal mapping of the physical domain which introduces extreme complexity for anything but the simplest mathematical specifications of flowfield boundaries.

The second approach for a solution of the NS by flowfield means is the use of a spectral method, relying on the postulate that a quasi-stream function incorporating the NS exists for the flow, from which other flow properties can be derived. This function is subjected to a series expansion of some type, for example, a Fourier or Chebyshev expansion. Numerical integration across the flow from the boundary conditions is then used to solve for the coefficients of the expansion terms. Numerical developments of spectral methods for computational fluid dynamics are relatively recent although the technique was used by Blasius as early as 1910 according to Plotkin¹⁹⁸². The methods hold promise for the future, but the comparative simplicity of the solutions achieved so far tends to suggest that they may best be left for further numerical research rather than applied to other problems. Hussaini & Zang¹⁹⁸⁷, in their review, indicate that spectral methods are still not well established for flows with shocks, and that a shock-capturing method would require substantially the same adaptations as other viscous flow solvers, namely, artificial viscosity and appropriate grid specification.

Another important approach to NS solution is to discretise the equation set over a grid and calculate the fluid properties at grid points, depending on the values at surrounding nodes (in both time and space). This class of techniques is known as finite difference method, or FDM. Although a great

variety of FDMs exist,^s one including the following features would be required for the solution of the complex flowfield around the Coanda flare:

- (a) Time-marching, for mixed regions of subsonic, supersonic and reversed flow.
- (b) Shock capturing, for markedly varied shock patterns on different flare configurations.
- (c) Conservation formulation of the NS equation set, which Anderson¹⁹⁸⁶ suggests is necessary in order to avoid large errors in flows with embedded shocks.

Issa & Lockwood^{1977a} compare a range of methods for prediction of supersonic viscous-inviscid interactions. They conclude that time-marching NS solutions are relatively costly in run-time computer resources. This poses difficulties in the current case where the modelling is required for iterative design work. Other problems mentioned are that the techniques are prone to numerical instability and to shock wave smearing inaccuracy in this type of flow. Care is also required in the selection of an appropriate grid for each flow boundary configuration.

Johnson, Horstman & Bacchalo¹⁹⁸⁰ identify the inadequate modelling of the turbulent Reynolds' stresses and shock smearing on grids as the major sources of inaccuracy in this type of method. MacCormack¹⁹⁸² also places emphasis on the importance of correct turbulence modelling for accuracy. Arieli & Murphy¹⁹⁸⁰ suggest that smearing can be overcome with mesh increments that are small with respect to the flow features, but if the locations of critical

features (shocks, separation points, etc.) are unknown in advance, either slow convergence results, if the whole mesh is fine, or computational complexity is required, through self-adaptive or multi-grid techniques.

A further problem, highlighted by Patankar & Spalding¹⁹⁷², is that NS solvers require some way of specifying the downstream boundary condition, which in the current case would require either a boundary placed in a weakly interacting zone downstream of the region of interest (hence significantly lowering computational efficiency) or some way of calculating an approximate solution near the flare, as demonstrated by Barnett & Davis¹⁹⁸⁶. The same argument also applies to the jet outer edge boundary, which would require an undisturbed far-field or some transpiration condition.

Murphy, Presley & Rose¹⁹⁷⁵ show that in supersonic separation the full NS only offer significant accuracy advantages over the PNS where the normal pressure gradient is large. Barnett & Davis¹⁹⁸⁶ point out, however, that if PNS solutions are employed where there are large reverse flow regions instability problems arise, quite apart from the fact that any reverse flow invalidates the PNS assumptions with consequent degradation of accuracy.

The consumption of computer resources by NS FDM solvers at run-time can be reduced considerably by the adaptation of the solution algorithm depending upon the results obtained in previous iterations. Kallinderis & Baron¹⁹⁸⁹ present a method which can change almost all features of the computation as necessary. However, this state-of-the-art code takes almost five hours of minicomputer *cpu* time for a case whose complexity parallels that of the flare. Since many such

cases would be needed for design optimisation such complex techniques are clearly unsuitable for the current requirements.

In spite of what has been said about computational time, it might be possible to refine the results of an approximate solution at reasonable cost, using an NS solver. This presupposes that the approximate solution is derived using some other method, and that the convergence of the full solver from the approximate solution is at least stable and hopefully rapid. Since the driving parameter for corrections usually depends to some extent on the overall error magnitude, achievement of the latter may prove elusive.

The weight of the foregoing evidence on NS FDMs for the full flowfield tends to confirm the advice of Watson¹⁹⁸⁷, that, within the timescale of the project, progress towards successful development of such a technique would be very limited. But it should be noted that Bradshaw^{1975a} offers the opinion that boundary layer methods are unlikely to supplant numerical solutions of the full time-dependent NS equations for accurate solutions of extremely complex turbulent flows. Issa & Lockwood^{1977b} support this opinion and further suggest that, in strong interactions, elliptic procedures are more economical than interacting boundary layer calculations.

2.2.4 MULTIPLE ZONE METHODS

In contrast to the methods described in the last section, multiple zone techniques divide the flowfield into regions of different features, which permits varied simplifications to be made as appropriate (for an example see Mahgoub

& Bradshaw¹⁹⁷⁹). The calculations in different zones may be quite dissimilar in form, depending on the method of coupling the solutions. Dash *et alia*¹⁹⁸³ point out the main feature of such methods: the individual calculations may be much more accurate, efficient and simpler to implement than a method which could cope with the entire flow field (especially since the turbulence model can be altered for the various regions of the flow) but there is obviously a computational overhead associated with iterating the separate calculations in the matching process.

The main problems begin with the fact that the coupling may lead to slow convergence or even instability, especially where the interaction between the zones is very strong. The boundaries of the zones have to be carefully selected, and the adoption of different approximations on either side of a boundary may render the two solutions incompatible. Overlap techniques can be used to avoid this (LeBalleur¹⁹⁸⁴). Furthermore, the approximations adopted within the zones may lead to significant inaccuracy in complex flows. However, for a research programme composed of separate projects, the choice of this approach permits incremental development, and allows relatively simple modification of the model to cope with future computational advances.

Effective selection of zones is a major contributor to the efficiency of the overall technique and depends heavily on both the flow configuration and the capability of various solution techniques. For the flare, the choice arises out of the description of the flowfield presented above:

- (a) A potential core, in which the effects of viscosity may be neglected, except at shock waves.
- (b) Inner and outer shear layers in which the influence of viscosity is significant.
- (c) A step recirculation zone, which is regarded as being at constant pressure, and in which the exact flow pattern is of little engineering interest.

In fact, division of the flowfield in this way also provides a framework for qualitative understanding, since it highlights the important parameters to be considered in each part of the flowfield, but some justification of the division is required.

Hunt's & Lamont's¹⁹⁸⁰ studies show that the assumption of inviscid flow is adequate outside the boundary layer region. This is confirmed for the present work by the absence of visible turbulent activity in the potential core zone of the Coanda jet in Gilchrist's¹⁹⁸⁵ spark schlieren visualisations. Murphy, Presley & Rose¹⁹⁷⁵ suggest that an interacting boundary layer model is acceptable where the normal velocity at the boundary layer edge is small with respect to the streamwise velocity. Whitfield, Swafford & Jacocks¹⁹⁸¹, using an integral boundary layer method in subsonic turbulent separation over an airfoil, show reasonable correspondence with the solution obtained by the full NS equations. Degani & Steger¹⁹⁸³ present evidence that the use of the thin layer approximations in a supersonic compression corner separation give rise to no worse inaccuracy than the PNS, and that both approximations are in reasonable agreement with the actual flow.

Hankey & Holden¹⁹⁷⁵ suggest that an interacting boundary layer method using the two dimensional, rotational MOC for the inviscid flow should be adequate for reasonable engineering predictions of the flow globally, although the detail at separation is likely to be poor. Stollery¹⁹⁷⁵ used the same technique, matching a well separated supersonic laminar boundary layer to the MOC, and concludes that this technique is quite useful, although special attention would be required for shocks and large regions of reverse flow. However, Issa & Lockwood^{1977a} point out that the coupling of a hyperbolic inviscid field (such as a MOC calculation) to a parabolic boundary layer technique makes the complete set of equations elliptic and thus prone to instability. Werle & Vatsa¹⁹⁷⁴ also mention the ellipticity arising from the coupling of hyperbolic and parabolic regions.

Green & Carpenter¹⁹⁸³ have developed a method for the flare mixing layer, which, although offered as a first approximation, would provide a suitable basis for further development. The real gas effects mentioned above suggest that a 'single' density calculation would provide a conservative underestimate for the entrainment. It is thought unlikely within the timescale of the current project that time will be available for investigating the mixing layer, but this is thought much less important from the standpoint of separation prediction than the boundary layer calculation. However, it is re-emphasised that entrainment is amongst the major parameters of the design, and so further development in this area will be required for full industrial application.

Dash & Wolf¹⁹⁸⁴ report what is currently the most complex multi-zone technique applied to the INDAIR type of problem although they have not reported its application to a significantly *separated* supersonic wall jet. Unfortunately, their SCIPVIS code is not available at Durham, and, given the resources available, development of an equivalent code would not have been practical. Moreover, their code appears to follow the trend of full NS solvers in that accuracy is emphasised at the expense of computational speed.

3 INTERACTING ZONE TECHNIQUES

3.1 THE POTENTIAL CORE

3.1.1 EULER EQUATION SOLVERS

The SCIPVIS code mentioned above uses a simplification of the NS equations, obtained by dropping the viscous terms, known as the Euler equations, to produce the solution for the potential core. Shankar¹⁹⁸² emphasises that even Euler solver codes tend to require extensive computer resources in terms of running time and memory usage. Denton¹⁹⁸² confirms this, and adds problems with shock smearing and entropy conservation as typical features.

Hall¹⁹⁸² suggests that oblique shocks can be so diffused by the use of such codes that they become unrecognisable and that capture can be difficult unless one grid direction is closely aligned with a shock. Furthermore, Hall's opinion is that explicit codes are better than implicit for embedded shock flows, but these are comparatively expensive in computing time. Moretti's¹⁹⁸⁷ review paper sets out in detail the main problems with shock-capturing codes, the principal difficulties being the necessity for expensive fine grids, the inaccurate

representation of shocks of some strength, particularly at shock intersections, and poor shock stability in the numerical scheme.

Until recently shock fitting Euler codes were limited mainly to those cases where the shock position was a computational boundary or the embedded shocks were roughly aligned with the grid (for an up-to-date example see Morton & Paisley¹⁹⁸⁹). Work by Moretti¹⁹⁸⁸ has produced a methodology combining the hybrid characteristic differencing recommended by Roe¹⁹⁸² with fitting for internal shocks, the main problem of shock detection being solved by examining the flowfield for jumps in Riemann variables. However, no evidence is given for the effectiveness of this methodology on *very weak* oblique shocks. The use of an Euler code would still require the addition of a viscous layer technique to complete the calculation, and experience shows (Drela & Giles¹⁹⁸⁶) that in strong interaction problems this is best added implicitly within the iteration scheme. Since the shock fitting approach is still under development, an implementation may take some time to appear.

3.1.2 THE METHOD OF CHARACTERISTICS

The Method of Characteristics (MOC) can be used to solve supersonic inviscid flows. Since it marches in space along the lines of physical influence, in the two dimensional form it is highly efficient for a given accuracy. Support for the choice of the method comes from Presley¹⁹⁷⁵, who says that 'for two dimensional flows the Method of Characteristics provides a standard for any other technique'.

Gilchrist¹⁹⁸⁵ demonstrated the Method of Characteristics' applicability to the planar curved wall jet core, which appears to remain supersonic almost up to the point where the shear layers meet and eliminate inviscid flow. In order to extend the technique for the current work, a number of modifications have been necessary, but it appeared both desirable and sensible to make use of the previous work.

One essential development was ensuring robustness in axisymmetry. Although many of the applications of the MOC in axisymmetry have been in cases where the predominant jet velocity is roughly parallel to the axis, Wu *et alia*¹⁹⁷⁷ presented a radial calculation for which no special adaptation requirements were reported. Green¹⁹⁸⁷ reported the use of the technique in the axisymmetric case for very short potential cores.

3.2 THE BOUNDARY LAYER

3.2.1 INTEGRAL, DIFFERENTIAL AND SERIES REPRESENTATIONS

There are numerous methods of computing boundary layer development. Some of the earliest developments concerned series expansions of the boundary layer equations. Lighthill¹⁹⁵³, Nieland¹⁹⁷⁰ and Stewartson¹⁹⁷⁴ have all produced solutions using matched asymptotic expansions in three decks for the shock-wave/boundary-layer separation problem, but, although this works quite well in the immediate vicinity of separation, it is limited to regions where the order of magnitude arguments used to derive the expansions are valid. Hence considerable computational complexity would ensue in applying it to an unknown

separation position and in matching it to incoming and outgoing solutions. The interaction in the above solutions is also clearly defined as a single shock wave separating a flat wall boundary layer, which, in the case of the flare, is clearly a poor approximation.

Integral profile methods for the boundary layer use predominantly empirical models of the velocity profiles which depend on the boundary conditions at the solid wall and the inviscid flow edge. These are regarded by Issa & Lockwood^{1977a} as adequate for predicting *general* features, provided the profiles are appropriate to the flow. Sirieix¹⁹⁷⁵ also points out the necessity for a good profile model.

Lees & Reeves¹⁹⁶⁴ found that the Von Kármán-Pohlhausen laminar boundary layer technique was inapplicable to separating and reattaching supersonic flows. Hankey & Holden¹⁹⁷⁵ are also of the opinion that the Pohlhausen technique is less applicable to adverse pressure gradient flows. Shan-Fu¹⁹⁷⁸ regards the Pohlhausen method as 'notoriously unreliable' with respect to separation prediction.

The numerical behaviour of an integral-defined layer can be classified (Crocco & Lees¹⁹⁶⁴) into subcritical and supercritical. The former category implies that the boundary layer responds to a small increment of pressure by thickening; the latter by thinning. The classification can be understood by taking subcritical as being equivalent to a subsonic *mean* velocity in the layer, and, correspondingly, supercritical as being a net supersonic layer.

Lees & Reeves¹⁹⁶⁴ found that a unique solution to a shock-separated boundary layer 'free interaction' could be defined by requiring that the incoming layer be subcritical, the outgoing one supercritical, and by matching the two solutions at the separation. Since the incoming layer may be supercritical, this method cannot readily be generalised. However, the author inclines to the suggestion of Green¹⁹⁷⁰ that the problem is a consequence of the physical inadequacy of certain numerical representations of the dissipative zone and that some modification is required here. Moreover, Werle & Vatsa¹⁹⁷⁴ criticise boundary layer 'shooting' techniques, in which solutions before and after some identifiable phenomenon such as a shock-induced separation are matched, as being expensive, due to their sensitivity to upstream conditions and inherent instability problems. Hankey & Holden¹⁹⁷⁵ comment that the definition by Myring & Young¹⁹⁶⁸ of integral boundary layer parameters along isobars produces subcritical behaviour. This appears to be the correct physical process since no report has come to the author's attention in which an impinging shock caused the boundary layer to thin out ahead of the interaction, as should be the case with a supercritical layer. Furthermore, Sirieix¹⁹⁷⁵ points out that subcritical behaviour may also be induced by including the normal pressure directly into the boundary layer equations.

Hankey & Holden¹⁹⁷⁵ also mention the possibility of using a two-layer model for the boundary layer with an inviscid rotational supersonic top and a viscous sublayer. Sirieix¹⁹⁷⁵ analysed the boundary layer in a compression corner separation, using a rotational inviscid supersonic deck and a subsonic viscous deck, with considerable success. This provided part of the motivation for

converting the MOC used by Gilchrist¹⁹⁸⁵ to model rotational flow in arbitrary geometry so that the option to try this approach was left open. Additional incentive came from the evidence of Sockol & Johnson¹⁹⁸⁶, which shows that the ‘free’ stream may in fact become rotational in a shock wave/boundary layer separation. Whilst this appears contradictory, as Cebeci & Smith¹⁹⁷⁴ point out, turbulence penetrates intermittently into the flow near the boundary layer ‘edge’, and amplification of this turbulence during interaction with the shock wave thus produces rotational flow in the nominally inviscid stream.

In the current work, an integral boundary layer technique has been chosen on account of the computational speed with which such methods are usually endowed. Halim & Hafez¹⁹⁸⁴ identify three main difficulties in applying integral boundary layer methods to flow with separation bubbles:

- (a) Singularities arising from the coupling method (see below).
- (b) Non-unique solutions for the bubble. (Johnson, Horstman & Bacchalo¹⁹⁸⁰ also note the presence of non-unique solutions but suggest that this can be resolved by compatibility to the outer flow.)
- (c) Instability for large flow reversal. (It is unlikely that any boundary layer method, integral or otherwise, will cope well with separation bubbles of greater scale than the 10δ limit suggested by Sirieix¹⁹⁷⁵ for thin separation. Since the INDAIR hysteresis region lower limit may be defined by thin separation failure, this may become more of an advantage than a problem.)

These difficulties with integral methods may make it necessary to consider moving to other techniques and some discussion of these is therefore required.

Differential boundary layer techniques are mainly analogues of the PNS solvers mentioned above, in that simplifications of the NS (usually ignoring more terms) are used to derive the flow equations. These equations are then discretised on a grid (which may be very fine). Out of many possibilities for this type of differencing, the current favourite scheme appears to be the Keller Box method, described in detail by Keller¹⁹⁷⁸ and recommended by Cebeci & Smith¹⁹⁷⁴ (amongst many others), because of its strong stability features. Provided that the NS simplifications are not too restrictive, differential methods can account for upstream influence via iteration. Efficiency in solution is sometimes increased by the assumption of no reverse flow or upstream influence, as in the parabolic method of Patankar & Spalding¹⁹⁷². This technique is clearly unsuitable for shock wave impingement and large separated regions without some appropriate modification.

The boundary layer method of Bradshaw & Ferris¹⁹⁷¹ (improved by Bradshaw & Unsworth¹⁹⁷⁴) has been found useful for hyperbolic solution of an adiabatic, compressible boundary layer in high subsonic and transonic flow. The algorithm uses a viscous characteristic network formulation to march downstream and as such is not readily adaptable for reverse flows. Moreover, its authors suggest that it will not perform reliably where expansion fans, shock waves or other self-induced pressure gradients are large. The latter paper points out that marching procedures are likely to degrade as the normal pressure gradient increases. Furthermore, the technique uses a logarithmic law to generate the near wall point properties, despite the opinion of Nagano & Hishida¹⁹⁸⁷ that, in a complex flow, this is not necessarily justified. However, Shang *et alia*¹⁹⁷³

show that some modelling of this region is required if errors are to be kept reasonable.

The criticisms of differential methods set out above apply with much greater force to the integral technique chosen for the flare calculation, particularly since, as Bradshaw^{1975b} points out, the downstream marching fails to incorporate the upstream influence due to subsonic transmission and reversed flow. In the absence of such influence, Emanuel¹⁹⁸⁴ points out that laminar boundary layer separation calculations will err towards overprediction of bubbles, but the inviscid attached calculations of Gilchrist¹⁹⁸⁵ show a favourable pressure gradient at points where the actual flare jet separates, suggesting that such a course would underpredict breakaway.

As a preliminary correction, the upstream influence criterion mentioned in section 2.2.2 may prove useful, since current results reveal a very rapid attainment of the constant pressure level observed in separation bubbles. Dvorak & Choi¹⁹⁸¹ report a method in which the first estimate for a differential boundary layer/potential flow is produced by an integral boundary layer approximation in order to accelerate convergence. If it proves necessary, this could be applied to the current technique by using the approximate calculation method during the design optimisation phase, and then by using the final solution as the first iterate in a time-marching method to achieve acceptable computational economy. Routines developed for interpolating the calculation flowfields for presentation purposes could be modified to provide grid point properties for making the transition between calculations.

3.2.2 LAMINAR AND TURBULENT MODELS

For integral boundary layer methods the handling of the presence or absence of turbulence is carried out within the profile model. Laminar profiles can be quite accurately modelled by the use of the Falkner-Skan one-parameter family (see Drela & Giles¹⁹⁸⁶). The adaptation of Stollery's¹⁹⁷⁵ supersonic laminar boundary layer calculation mentioned above to the turbulent case was hampered by the lack of suitable profile modelling in pressure gradients. Swafford¹⁹⁸³ presents an analytical expression for correlating quite complex turbulent pressure gradient boundary layers and references work extending this to compressible flow. Drela & Giles¹⁹⁸⁶ have subsequently made use of this extension.

The profiles can be based on fitting an analytical equation to skin friction and modelling the dissipation coefficient. This approach is adopted by Winter, Rotta & Smith¹⁹⁶⁸. They mention normal pressure gradient as a source of inaccuracy but point out that $H(= \delta^*/\vartheta)$ is not much affected by this, and that the dissipation coefficient modelling to which their calculation is sensitive is a more likely culprit for errors. Assassa & Papailiou¹⁹⁷⁹, in a subsonic case, use dissipation and skin friction modelling which is stated in a form extendable to compressible flow.

For differential techniques the analogous problem is the specification of a turbulence model (laminar behaviour being a consequence of the fluid properties). Few studies have been devoted to specifically compressible models of turbulence (as concluded by Sirieix¹⁹⁷⁵), despite the evidence of Bogdanoff¹⁹⁸³ that compressibility reduces the growth rate of a turbulent shear layer. However,

a considerable amount of work has been extended from incompressible work, based on Morkovin's hypothesis that the turbulence *structure* is unaffected by compressibility if the density fluctuations are small compared to the mean density (mentioned in Bradshaw & Ferris¹⁹⁷⁰). The work of Sturek¹⁹⁷⁴ confirms that this approach is accurate in zero pressure gradient flows, although Viegas & Horstmann¹⁹⁷⁹ have questioned its validity in rapidly changing and separating flows.

Bradshaw¹⁹⁷⁴ points out that regions of bulk compression increase turbulence intensity, whilst bulk dilatation has the opposite effect. Dash, Wilmoth & Pergament¹⁹⁷⁹ also mention that pressure gradients, consequences of compression and dilatation, have large effects on mixing rates in shear layers. Jobe & Hankey¹⁹⁸⁰ rule out the use of algebraic eddy viscosity models in regions of adverse pressure gradient, which would militate against the use of the Bradshaw, Ferris & Atwell¹⁹⁶⁷ technique, and, indeed, the latter state that their empirical mixing length modification is inappropriate for separating flows.

Laderman¹⁹⁷⁹ reviews the turbulence modelling of supersonic adverse pressure gradient boundary layers and Launder & Rodi¹⁹⁸¹ that of turbulent subsonic wall jets. Nagano & Hishida¹⁹⁸⁷ give a critical comparison of the application of current models to a variety of demanding flow fields. A major development of their paper is a modification of the k - ϵ model to apply to the law of the wall region as well as the main part of the boundary layer, which thereby simplifies the coding of turbulent boundary layer techniques.

Viegas & Horstmann¹⁹⁷⁹ compare the performance of several turbulence models to the turbulent compressible separation problem and conclude that no one model is superior; the two-equation Wilcox-Rubesin model giving better reattachment and pressure distribution accuracy, but being inferior to a zero-equation method for the separation point. They sound a cautionary note about possible three-dimensional effects in the nominally two-dimensional test case against which the calculations were compared.

Gibson & Rodi¹⁹⁸¹ found that a conventional k - ϵ model failed to account for curvature effects, but Dash *et alia*¹⁹⁸³, in a closely analogous case to the INDAIR, model the turbulence with a k - ϵ model using Bradshaw-type extra strain rate modifications, as this gave better results than the mixing length model (used in Dash, Wilmoth & Pergament¹⁹⁷⁹). Further problems arise from the fact that most current turbulence models are written so that the turbulence structure does not depend on the history of the flow up to that point. Johnson, Horstman & Bacchalo¹⁹⁸⁰ suggest that these local equilibrium turbulence models overpredict the ability of turbulent boundary layers to overcome adverse pressure gradients owing to the slower large eddy response. Nagano & Hishida¹⁹⁸⁷ also report overprediction of skin friction.

Winter, Rotta & Smith¹⁹⁶⁸ highlight the inadequacy of equilibrium modelling in strong *favourable* pressure gradients and streamline divergence. Wilson & Goldstein¹⁹⁷⁶ show that non-equilibrium turbulence can arise in a curved wall jet even though the mean flow appears to support the assumption of equilibrium. Baldwin & Rose¹⁹⁷⁵ and Werle & Bertke¹⁹⁷⁶ point out the inadequacy of ignoring

non-equilibrium effects in supersonic turbulent separation. Recently, Abdol-Hamid & Wilmoth¹⁹⁸⁹ applied a four-equation k - ϵ type turbulence model based on the Hanjalic approach, which effectively placed turbulence production in the low-frequency part and dissipation in the high-frequency part of the spectrum. In supersonic wall jet studies with the SCIPVIS code, this rudimentary structural modelling has produced a significant improvement on the previous k - ϵ model. It should be emphasised that the problems in obtaining accuracy from a NS solver depend to a large extent on the same turbulence modelling considerations as a differential boundary layer method.

Given the problems of turbulence modelling mentioned above, it seems that the use of a differential rather than an integral method for the boundary layer, in order to give greater accuracy, is not easy to justify. Since the integral method offers the substantial gain in speed mentioned above, it was chosen as the first step in the development process. The method of Whitfield, Swafford & Jacocks¹⁹⁸¹ was adopted as the basis for turbulent boundary layer prediction. This technique was supplemented by laminar predictions, using the Falkner-Skan profile family with an e^9 transition criterion*, and using non-equilibrium turbulence modelling developed by Drela & Giles¹⁹⁸⁶. Since both of these papers match boundary layers with separation to inviscid fields, this was thought to be the most promising of the integral methods reported.

3.2.3 FURTHER COMPLICATIONS

The boundary layer in the flare is likely to have significant areas of laminar flow, due to the influence of strong favourable pressure gradients and

* criterion based on a shape factor correlation of e^9 disturbance amplification curves

convex curvature, which, as Gibson & Younis¹⁹⁸² have demonstrated, causes the suppression of turbulence, especially in the inner layer, which has a large effect on separation behaviour and upstream influence. Guitton¹⁹⁶⁴ presents evidence for the suppression of turbulence in a subsonic turbulent curved wall jet. Liu's & Squire's¹⁹⁸⁸ work on shock-induced separation on curved walls also tends to support the suppression of turbulence by convex curvature, even in the adverse pressure gradient case, since their separation lengths increase with curvature. Although the Drela & Giles¹⁹⁸⁶ integral model chosen for this work has a laminar-to-turbulent transition prediction, it lacks the reverse transition.

Narasimha & Sreenivasan¹⁹⁷⁹ give a wide review of relaminarisation phenomena and suggest that stabilising curvature and rapid acceleration are key factors in turbulent-to-laminar transition. These features give rise to a quasi-laminar flow in which the large turbulent eddies are collapsed. They give an empirical criterion for relaminarisation by acceleration, which could be used in the absence of a more detailed model. Muck, Hoffman & Bradshaw¹⁹⁸⁵ show that the effect of stabilising (convex) curvature on turbulence structure acts very quickly, in contrast to the effect of destabilising curvature.

Surface curvature is a marked feature of the INDAIR and is expected to have a considerable effect on the boundary layer. Gibson & Younis¹⁹⁸² point out that curvature will induce normal pressure gradients and they have estimated these for a subsonic case, using centrifugal arguments. Rotta¹⁹⁶⁷ expresses the opinion that the normal pressure gradient in a supersonic boundary layer amplifies the effects of curvature. Furthermore, this paper suggests that

heat transfer from the flow to the wall in convex curvature destabilises the turbulence of the boundary layer and thus increases its separation resistance, as was also noted by Stollery¹⁹⁶⁹. Hence, conversely, it could be expected that in the real flare the heating of the flare tip by flame radiation would predispose the flow to earlier separation in an adverse pressure gradient and to the maintenance of laminar features over a greater proportion of the boundary layer.

Stollery¹⁹⁶⁹ suggests that computational problems may stem from significant normal pressure gradients in supersonic flows. Myring & Young¹⁹⁶⁸ suggest modifying the definition of the integral parameters to alleviate the problem of normal pressure gradients in supersonic boundary layers. Their hypothesis is that the isobars in the boundary layer are, for all practical purposes, coincident with linear extensions of the Mach lines in the external flow, for which they present some experimental evidence. The work of Havener & Radley¹⁹⁷⁴ supports this evidence and points out that in any flowfield where streamwise pressure gradients are very large normal pressure gradients are likely to occur.

Using the normal pressure gradient generated by an overlapping inviscid solution with an integral boundary layer method is thought by LeBalleur¹⁹⁸⁴ to be accurate for modelling viscous-inviscid interaction, apart from in zones where shock penetration into the boundary layer occurs. Werle & Bertke¹⁹⁷⁶ point out that using an interacting calculation may cause inaccuracies, particularly in the separation region, due to the shock not permeating into the boundary layer.

The axisymmetry of the real flare would require a suitable form of the boundary layer equations, but it would also be highly desirable to have planar calculation capability, both for testing against planar data and for general prediction of planar Coanda jets. Carter¹⁹⁷⁹ calculates an axisymmetric boundary layer by applying the Mangler transformation (Schlichting¹⁹⁷⁹) and calculating an equivalent planar case. This is particularly attractive for use with a MOC solver in that simplicity of modification for axisymmetric geometry is present in both domains. Bradshaw, Cebeci & Whitelaw¹⁹⁸¹ also present the Mangler transformation as a useful engineering technique for axisymmetric flows, but it should be noted that the transformation works only for the boundary layer equations without a normal momentum equation.

The complications set out above suggest that close accuracy is relatively unlikely, regardless of the boundary layer method used. The question which arises here is how much improvement a complex technique would bring. Since a simple integral method can be compared indirectly to the experimental evidence, this appears to be the best route to follow as a first approximation, reserving the resources required for a more complicated attempt for later if found necessary.

3.3 SUPERSONIC BASE MODELLING

Early work on base flow computation by Chapman & Korst used a step and straight walls as the flow boundaries (in both planar and axisymmetric configurations), with the assumption of isentropic recompression of the fluid

on the dividing streamline joining the corner separation and the reattachment stagnation point. Tanner¹⁹⁷³ makes the point that the Chapman-Korst assumption is not borne out by experimental evidence in the low supersonic region or in base flows around wedges. The source of their error seems to lie in the assumption that compression to the final reattachment pressure level occurs on the dividing streamline. Corrections to the model have centred on modifications to the reattachment pressure level (see the comprehensive review of Carpenter & Tabakoff¹⁹⁶⁸), but Sirieix¹⁹⁷⁵ criticises the assumption of isentropic recompression along the dividing streamline in general as an inaccurate representation of the physics of the flow.

Green¹⁹⁷⁰ points out that the methods based on the Chapman-Korst concept, which depend more or less on modelling the overall pressure rise at reattachment, are unsuitable for more complex flows where longitudinal curvature of the wall, incoming waves and shear layers or other disturbances are involved. His suggestion is that streamline angle methods such as those of Tanner and Sirieix are much better suited to these cases. Some work has been devoted to the effect of the incoming boundary layer, but the experiments of Alber & Lees¹⁹⁶⁸ show that these are negligible for $M_\infty < 2$. Chow & Spring¹⁹⁷⁵ correlate many results in base flows and demonstrate that the base pressure is unaffected by boundary layers where $\vartheta < \text{step height}/10$. Inger's¹⁹⁷⁴ data suggests a limit of $1.2\delta < \text{step height}$. Since all these criteria are likely to be met in the current configuration, the boundary layer effect is ignored.

The analysis proposed by Tanner¹⁹⁷³ for the subsonic case equates the pressure drag energy loss at the step to energy loss in the mixing zone, ignoring skin friction as negligible. This appears to be a much more general assumption than that of Chapman-Korst type models, since the configuration of the reattachment zone and the flow conditions external to it, (*e.g* the incoming boundary layer), can be incorporated into the model using conventional shear layer analysis.

The same equating of pressure drag loss to fluid losses is extended to the supersonic case in Tanner¹⁹⁷⁸. However, an additional subtlety is introduced by the reattachment shock. Tanner argues that an 'ideal' fluid case at the same base pressure would produce the loss solely via the shock, whereas the effect of the mixing layer is to produce compression waves, which render the flow effectively isentropic until they coalesce into the reattachment shock at some distance from the surface. The base pressure can be predicted using an analytical approximation for the shear layer profile at reattachment, and then equating the shear layer entropy increase in the real case to the 'lost' shock section in the ideal case via an empirical shock stand-off/shear layer thickness ratio. The choice of stand-off ratio is chosen to match experimental data at $M_\infty = 1.73$ and is shown to give good agreement throughout the low supersonic zone ($1.0 < M_\infty < 3.0$). Although more empirical than the subsonic method, the supersonic method can also account for wall contour via the shock direction required at reattachment in the ideal equivalent case.

Further empiricism in the Tanner model, introduced by the assumption of a finite slip velocity profile shear layer at the wall reattachment point, seems, at first sight, to be somewhat far-fetched, but the work of Alber & Lees¹⁹⁶⁸ shows this assumption to be substantially justified, and Sirieix¹⁹⁷⁵ confirms this by reference to experimental work by Délery (Carrière, Sirieix & Délery¹⁹⁷⁵).

Weinbaum¹⁹⁶⁶ suggests that the overexpansion at the corner can be used with the rotational MOC to give weak lip shocks. Baum¹⁹⁶⁸ shows that accurate modelling of this process requires considerable detail of the boundary layer and corner flow region and this would appear to be a major stumbling block for an engineering computation of the INDAIR flowfield. However, Hama¹⁹⁶⁶ gives a simple correlation for the effects of the lip shock for engineering accuracy simulation. Work by Magi & Gai¹⁹⁸⁸ gives a correction for the effect of the lip shock on the base pressure in the Tanner model. It was therefore decided to use the Tanner model for the supersonic base flow, since coupling to the MOC required little modification and there is good evidence presented for its accuracy in flow conditions typical of the INDAIR.

3.4 ZONE INTERACTION

3.4.1 MATCHING PARAMETERS

The criteria by which an inviscid calculation can be linked to a dissipative layer calculation reduce to a quite limited number, despite the many forms in which they have been presented by different authors. The direct method is to specify $p(s, \delta)$ for the boundary layer from an inviscid solution and to

complete the coupling by modifying the inviscid flow boundary by δ^* , iterating the solutions as necessary to find convergence. A commonly used additional simplification is that $p(s, \delta) = p(s, 0)$ implying that $\frac{\partial p}{\partial n} = 0$ in the boundary layer. It has long been known, however, that this direct method exhibits mathematical instability at points of zero skin friction (*i.e.* separation) and thus is of limited use for the current work. However, Jobe & Hankey¹⁹⁸⁰ recommend this method in regions of known favourable pressure gradient because of its rapid convergence property. LeBalleur¹⁹⁸⁴ uses this technique but switches to other methods well before any likely separation. The work of Ardonceau & de Roquefort¹⁹⁸⁰ on displacement thickness and pressure gradients in laminar boundary layers suggests that not only is direct matching desirable in areas of favourable pressure gradient but that it may even be necessary to prevent numerical instability.

It is common knowledge that this singularity at separation can be alleviated by an ‘inverse’ procedure whereby some other property of the viscous layer is specified and the boundary layer equations are solved to give the edge pressure distribution. Carter¹⁹⁷⁹ uses δ^* as the specified property for both viscous and inviscid domains and adjusts the approximation based upon underrelaxation of the difference in predicted boundary layer edge velocity between the two solutions. The coupling of δ^* into the inviscid calculation is via a notional surface transpiration and viscous/inviscid overlap, but the transpiration condition is unsuitable for MOC matching, due to the inflow

velocity. Whitfield, Swafford & Jacocks¹⁹⁸¹ modify the transpiration equation to:

$$\rho v_{inv} = \frac{1}{r^\nabla} \frac{\partial}{\partial s} (\rho_e u_e \delta^* r^\nabla)$$

$$\text{where } \nabla = \begin{cases} 0 & \text{in planar geometry;} \\ 1 & \text{in axisymmetric geometry} \end{cases}$$

It should be noted that the use of potential sources mentioned by Newman¹⁹⁶⁹ for coupling the effect of boundary layers and wakes to inviscid solutions is effectively a transpiration condition.

Carter & Wornom¹⁹⁷⁵ give three alternative properties for inverse methods; δ^* , C_f or v_e . Dash *et alia*¹⁹⁸³, who use overlapping domains, suggest that simple displacement thickness coupling is inadequate for the supersonic curved wall jet problem. The solution they adopted was to use the displacement surface as the boundary condition for the inviscid flow and the equivalent transpiration velocity at the boundary layer *edge* as the viscous coupling. A related overlap technique is used by LeBalleur¹⁹⁸⁴, who recasts the viscous equations in terms of deficit quantities ($u_{visc} = u_{act} - u_{inv}$, *etc*) and uses surface transpiration as the inviscid coupling condition, and the body no-slip condition combined with inviscid velocities to specify the viscous boundary. The latter technique has been modified for use with an integral boundary layer to speed up the calculation by redefinition of the integral quantities. The paper, however, mentions that its application to strong interaction remains uncertain.

Ribaut¹⁹⁸³ uses vorticity on the matching surface for coupling, but his use of vorticity diffusion and dissipation relationships in separated zones adds complexity and empiricism. Murphy, Presley & Rose¹⁹⁷⁵ suggest that the use of normal velocity matching gives greater physical realism than tangency of

the flow on matching lines. Lees & Reeves¹⁹⁶⁴ also solved a strong interaction problem, by applying the coupling conditions at the boundary layer edge. The inviscid streamline direction was determined by the mass growth rate of the boundary layer, using the following equation:

$$\begin{aligned}\tan \lambda_e^o &= \frac{v_e}{u_e} \\ &= \frac{\partial \delta^*}{\partial s} + \frac{\partial}{\partial s} \log(\rho_e u_e (\delta - \delta^*))\end{aligned}$$

This appears to be quite useful for MOC matching to an integral method, since the edge velocity is explicit and represents an *outflow* from the inviscid field which can be accounted for by interpolation, and the pressure variations within the boundary layer are left to the profile family. Lee & Pletcher¹⁹⁸⁸, in an analogous technique, use the mass flow into the boundary layer to give an inviscid edge stream function value. The method gives some physical realism, since it provides a computational route for the transfer of momentum from the mean flow to the boundary layer, without which, according to Adamson & Messiter¹⁹⁸⁰, matching problems arise.

Halim & Hafez¹⁹⁸⁴ report success with a pseudo-stream function matching, in which the stream functions at the edge of both regions (ψ_{inv} and ψ_{visc}) are combined via a matching formula to produce a matching line stream function ψ_{mat} . This is then used as a boundary condition for the next iteration of both calculations. From a number of options tested, the formulation of this condition which seems most suitable for the Coanda boundary layer calculation is:

$$\begin{aligned}u_{mat}(n_{mat} - \delta^*) &= \psi_{mat} \\ u_{mat} &= \frac{\partial \psi_{mat}}{\partial n}\end{aligned}$$

A particular feature of Halim's & Hafez' method is that it has also been used with some success for predicting flow over a backward-facing step.

However, the most widely used inverse coupling method is the specification of δ^* , so this was used as the starting point for the development programme. This was not regarded as a rigid choice, but the application of other alternatives would have required a significant amount of work in reformulating the computational method.

3.4.2 COUPLING ALGORITHMS

The area of coupling algorithms was also one in which the selection was left somewhat open, since no method offered a clear certainty of rapid convergence. The starting point was taken as the most convenient and least costly technique, namely, that of marching the boundary layer with the MOC and iterating locally at each spatial step.

Mahgoub & Bradshaw¹⁹⁷⁹ point out that errors can arise from local matching when discretised values of the boundary layer properties are used to generate property gradients. They used global iteration and cubic spline approximation, although, when shocks are present, this could present problems. Interpolation might require exponential splines (McCartin¹⁹⁸³), although this would be computationally less efficient. Overall, the approach is less than desirable, since the purpose of using marching methods in the first place is to promote efficiency. However, for a strong interaction problem, sequential iteration appears

inferior to simultaneous global implementations (Drela & Giles¹⁹⁸⁶ and Lee & Pletcher¹⁹⁸⁸).

A more serious objection to marching is that no upstream influence is accounted for in the technique. In some differential boundary layer models this has been dealt with by temporal iteration, for example Werle & Bertke¹⁹⁷⁶, and upstream influence has been further enhanced by upwinding the difference scheme. They suggest that the underestimation of upstream influence is the major factor causing inaccuracy in supersonic separations. Alternating marching directions are mentioned in Bradshaw, Cebeci & Whitelaw¹⁹⁸¹ and were used by Barnett & Davis¹⁹⁸⁶ and Stookesberry & Tannehill¹⁹⁸⁷, amongst others, to generate numerical upstream influence. Since modelling the extent of upstream influence is likely to be somewhat suspect anyway (see section 2.2.2), a simple empirical correction was envisaged, based on iterating the joint marching procedure.

Brandeis & Rom¹⁹⁸⁰ sound a note of caution with respect to matching algorithms with the MOC and use a relaxation of the edge pressures from the viscous and inviscid regions to converge the calculation. Brune, Rubbert & Nark¹⁹⁷⁵ give an interpolation procedure with Newton-type convergence, which may avoid the slow convergence or even divergence which can be experienced with simple iteration. Kwon & Pletcher¹⁹⁸⁶ and Lee & Pletcher¹⁹⁸⁸ both report the use of underrelaxation of the matching parameter (δ^* and \dot{m}_e respectively) in an inverse method to achieve stability, although the latter paper points out that the accuracy of the solution, once attained, depends more upon the turbulence model than the interaction algorithm.

In principle, whatever matching method is finally adopted could also be used to couple in a mixing layer model. However, Brandeis & Rom¹⁹⁸⁰ mention that with multi-zone matching care must be taken that the matching process of any two regions does not destabilise any of the other calculations.

4 COMPUTATIONAL METHOD DEVELOPMENT

4.1 METHOD OF CHARACTERISTICS

4.1.1 PREVIOUSLY EXISTING CODE

A code for applying the Method of Characteristics (MOC) to the INDAIR flare jet core was developed by Gilchrist¹⁹⁸⁵. However, the method logic was strongly tied to the geometry of the original unstepped flare. Both the network numbering scheme and the avoidance of infinite characteristic line gradients by coordinate rotation posed considerable obstacles to conversion for use in a more general situation. It should be mentioned that the irrotational method can be modified for infinite characteristic gradients by applying mathematical limit theorems to the compatibility equations before discretisation, but this requires alteration of the basic unit process and thereby reintroduces complexity. Furthermore, boundary conditions, such as the lip expansion process, were modelled by specialised modifications of the marching process. The foregoing points, allied to the fact that it was proposed to alter the basic MOC algorithm

to cope with rotational flow, left no real justification for extending or modifying the original code.

4.1.2 SPECIFICATIONS FOR THE MOC CODE

Since, as mentioned in previous chapters, the primary purpose of the calculation was to permit redesign of the INDAIR flare, it was considered of paramount importance to separate the logic implementing the MOC as far as possible from that incorporating the special boundary conditions of the current flare. An intended by-product of this approach was to develop a MOC code which could be applied to new flares, or even to other situations, with a minimum of modification. The obvious way to achieve this was by modular programming and by imposing all boundary conditions via routines which set or reset the main flowfield data arrays (including flag arrays). Since the actual MOC unit processes are similar at each marching step, these were also candidates for modular implementation. One great advantage of modular programming is that sections of code can be tested independently, and, provided good discipline is maintained with respect to global variables, this can be relied upon when the whole program is tested.

A second major requirement for the code was that of portability to the industrial sponsor. This determined the choice of FORTRAN77 as the high-level language (in actual fact, IBM FORTRANVS but no IBM extensions were used). Although the development environment was an Amdahl V8 mainframe computer running under the MTS operating system, enquiries revealed that the target machine for industrial use was unlikely to exceed the capabilities of an

advanced desktop microcomputer. This imposed a number of constraints upon the programming, notably the need to ensure rapid convergence of the iterative routines. In the development version, the flowfield data is held in large arrays for efficiency. However, the data is also written to disc file at the end of each marching step so that potential exists for substantial reduction of array space merely by converting the counter handling to modulo arithmetic. This approach also lends itself to data security, since the results are placed in non-volatile form as soon as possible. A more serious problem with portability arises from the use of the NAG Library¹⁹⁸⁸ to perform cubic B-spline interpolation. This is unlikely to be available at the target site (although a micro version of the NAG Library is produced), but the routines using the interpolation are stand-alone that the program is not bound to use this library.

In the later stages of the project, it was found necessary to port the program onto an Apple Macintosh microcomputer. Fortunately, due to the large installed memory on this machine, modulo counter conversion was not required and the program changes were reduced to re-writing the spline routines. For this purpose code from Press *et alia*¹⁹⁸⁷ was used.

No mention has yet been made about the presentation of results from the calculation. It was decided to leave this to a separate program, since the requirements of the research project and of the industrial development are substantially different. Moreover, at the time of writing, portability in the area of computer graphics programs was at best limited, particularly between

mainframe and micro-computers. Specifications for this program are discussed below.

4.1.3 DETAILS OF THE COMPUTATION

4.1.3.1 Basic Algorithm

Considerable evidence was gathered from the planar Coanda model tests for strong oblique shock waves, some of which had noticeable curvature. Chang & Chow¹⁹⁷⁴ found that rotationality arising from curved shock waves was an important factor in the downstream flowfield. Hence a rotational MOC algorithm was required. The basic algorithm for the MOC is that given by Zucrow & Hoffman¹⁹⁷⁶. It is based on the continuity and gas dynamic equations for rotational isentropic flow in two dimensions:

$$\begin{aligned} \rho \frac{\partial u}{\partial x} + \rho \frac{\partial v}{\partial y} + u \frac{\partial \rho}{\partial x} + v \frac{\partial \rho}{\partial y} + \frac{\nabla \rho v}{y} &= 0 \\ \rho u \frac{\partial u}{\partial x} + \rho v \frac{\partial u}{\partial y} + \frac{\partial p}{\partial x} &= 0 \\ \rho u \frac{\partial v}{\partial x} + \rho v \frac{\partial v}{\partial y} + \frac{\partial p}{\partial y} &= 0 \\ u \frac{\partial p}{\partial x} + v \frac{\partial p}{\partial y} - a^2 u \frac{\partial p}{\partial x} - a^2 v \frac{\partial p}{\partial y} &= 0 \end{aligned}$$

where $\nabla = \begin{cases} 0 & \text{in planar geometry} \\ 1 & \text{in axisymmetric geometry} \end{cases}$

After some manipulation these reduce to a set of eight equations valid at every point in the flowfield. Four equations specify lines of influence or characteristics (in fact two of these are coincident with the streamline) and the other four are equations for properties, known as compatibility equations, which are valid along these lines. The characteristic equations are:

$$\lambda^{\pm} = \tan(\theta_{\pm} \pm \alpha_{\pm})$$

$$\lambda^{\circ} = \tan(\theta_{\circ})$$

and the compatibility equations are:

$$\left[\frac{\sqrt{M_{\pm}^2 - 1}}{\rho_{\pm} V_{\pm}^2} \right] dp_{\pm} \mp d\theta_{\pm} + \left[\frac{\nabla \sin(\theta_{\pm})}{r_{\pm} M_{\pm} \cos(\theta_{\pm} \pm \alpha_{\pm})} \right] dx_{\pm} = 0$$

$$\rho_o V_o dV_o + dp_o = 0$$

$$dp_o - a_o^2 d\rho_o = 0$$

Other formulations are possible but Hoffman¹⁹⁷³ presents evidence to suggest that a characteristic finite difference scheme based on this rotational formulation has the best accuracy for a given step size in axisymmetry.

In supersonic flow all the influence line equations have real solutions and thus an algorithm can be derived which permits marching in space. This is achieved by discretising the equations and substituting known values to predict the flowfield values in the marching direction. Repeated application from the initial conditions then provides a complete solution of the supersonic flow by marching downstream. The discretised equations are (with reference to figure 4.1):

$$y_3 - \lambda^o x_3 = y_4 - \lambda^o x_4$$

$$y_1 - \lambda^+ x_1 = y_4 - \lambda^+ x_4$$

$$y_2 - \lambda^- x_2 = y_4 - \lambda^- x_4$$

$$y_3 - \lambda^{12} x_3 = y_2 - \lambda^{12} x_2$$

and the discretisation of the compatibility equations yields:

$$Q^+ p_4 + \theta_4 = -S^+(x_4 - x_1) + Q^+ p_1 + \theta_1$$

$$Q^- p_4 - \theta_4 = -S^-(x_4 - x_2) + Q^- p_2 - \theta_2$$

$$R^o V_4 + p_4 = R^o V_3 + p_3$$

$$p_4 - A^o \rho_4 = p_3 - A^o \rho_3$$

$$\text{where } Q^\pm = \frac{\sqrt{M_\pm^2 - 1}}{\rho_\pm V_\pm^2}$$

$$S^\pm = \frac{\nabla \sin(\theta_\pm)}{r_\pm M_\pm \cos(\theta_\pm \pm \alpha_\pm)}$$

$$R^\circ = \overline{\rho_o V_o}$$

$$A^\circ = \overline{a_o^2}$$

Since there are three equations for position in two-dimensional geometry, this leads to an overspecified problem. In the current method, back projection of the streamline from the intersection of the two characteristics is adopted for computational simplicity despite the slight reduction in accuracy mentioned by Hoffman¹⁹⁷³ from a scheme which projects one characteristic back. Interpolation between known solution points (1) and (2) (figure 4.1) is used to derive properties on the back-projected streamline at the start of the marching step. However, as detailed later, the streamline is used to predict location at points where one characteristic is replaced by boundary conditions. Iterative application of the equations at a solution point is required, since the location of the point depends on the average properties along the characteristic segments, which in turn depend on the predicted location of the solution point.

It will be noticed readily from the above equations that infinite values for gradient affect only the characteristics, ^{in planar flow} in contrast to the method used by Gilchrist¹⁹⁸⁵. Infinite gradients can be detected easily and appropriate geometrical adjustments* made without resorting to the complexity and reduction in efficiency required by coordinate transformation or other methods.

* in axisymmetry as $\theta_\pm \pm \alpha_\pm \rightarrow \pi/2$
 $S_T^\pm dy^\pm$ is used where $S_T^\pm = S^\pm / \lambda^\pm = \frac{\nabla \sin(\theta_\pm)}{r_\pm M_\pm \sin(\theta_\pm \pm \alpha_\pm)}$

4.1.3.2 Boundary Conditions

In the current method, boundary conditions are handled by using separate MOC unit processes which employ known boundary values for geometry or flow properties (or both), in order to eliminate the corresponding characteristic or compatibility equations. Since one family of characteristics is always missing at a boundary, the streamline and the other characteristic is used to march the geometry forward. At the outer jet edge, pressure is constant ($p = p_{atm}$) which also fixes V and ρ along the isentropic streamline and thus eliminates three of the four compatibility equations. The process reduces to identifying the solution point from the streamline λ^o and the left-running λ^+ characteristic and the flow angle θ from the remaining compatibility equation. This algorithm remains iterative since λ^o and λ^+ both depend on θ . A similar process is used at the inner jet edge in predicted separation bubbles by assuming that the pressure in the bubble is substantially constant.

For an attached section of the jet inner edge, the Coanda surface specifies the inner streamline, thereby replacing the λ^o characteristic equation. The absence of the λ^+ characteristic also eliminates the corresponding compatibility equation, but since θ is fixed by the surface gradient, the equation set remains closed, leaving the position on the surface, V , p and ρ as the unknowns for which iterative solution is required. Alternatively, the pressure on the inner edge can be also be specified, leaving the position, V and ρ as the dependent variables. Where this does not converge, due to mismatch between p and θ at the surface, the flow could be assumed to separate, and so recalculation with a separated unit process would be applied. The pressure-specified type

of unit process actually retains the streamline for the iterative determination of geometry with the λ^- characteristic, but the λ^0 characteristic is replaced by the surface contour if the solution point predicted penetrates the Coanda surface. Thus the flow is assumed separated and recalculated as attached when predicted, which gives greater computational simplicity, since it permits the use of one routine for both separated and attached pressure-specified inner edge points. The given pressure can be supplied from experimental data (interpolated using a cubic B-spline), from a concurrent boundary layer calculation (see below), or from an empirical model such as that used below for base flow.

Solution points where all properties are known from other sources, such as initial value points, shock reflections and centred expansion fans, are simply loaded directly into the solution arrays and the program flags set so that calculation of these points by the MOC is not attempted. In the case of expansion fans, each discretised wave of the fan is only required on the marching step subsequent to that using the previous wave (see figure 4.2b). Computationally, this can be reduced to the logic of figure 4.2c, so that by preloading the data arrays and setting the flag arrays appropriately, a unit process can be used to march the solution. By contrast with the conventional unit process, interpolation of the streamline between the λ^- and λ^+ characteristics is not physically valid, since this would imply that the influence of the turning pressure increment was propagating along the *previous* discrete expansion wave, as in figure 4.2a, so a modified process is required

at expansion fans. A decrementing wave counter is used to signal the switch back to other boundary processes.

4.1.3.3 Base Pressure Model

The model chosen for the recirculation zone at the step was that described by Tanner¹⁹⁷⁸. However, direct application of the model was not possible, due to the effects of the lip expansion wave and axisymmetry. The basic idea of equating the entropy gain of the shear layer with that of a notional 'lost' shock segment was retained, but the MOC itself was marched forward to determine the configuration of that shock segment, rather than using simple wave flow arguments. Since the shear layer and the notional shock segment were expected to be quite small with respect to Coanda radius, and since the model itself is semi-empirical, the axisymmetric case was approximated by applying the planar entropy gain balance as given here:

$$\int_0^\infty \frac{\rho U}{\rho_\infty U_\infty} \left(1 - \frac{U}{U_\infty}\right) dy \cdot \gamma M_\infty^2 = \frac{\delta^s}{\delta} \ln \left(\frac{\left[1 + \frac{2\gamma}{\gamma+1} (M_{e\infty}^2 \sin^2 \beta - 1)\right]^{1/(\gamma-1)}}{\left[\frac{(\gamma+1)M_{e\infty}^2 \sin^2 \beta}{(\gamma-1)M_{e\infty}^2 \sin^2 \beta + 2}\right]^{\gamma/(\gamma-1)}} \right)$$

Binary iteration between a sonic turning reattachment shock (minimum base pressure) and the minimum expansion for surface reattachment (maximum base pressure) was used to speed the calculation. The program was arranged in such a way that experimental or estimated values of base pressure could also be used to replace the iteration.

4.1.3.4 Shock Waves

The factors mentioned above in section 4.1.3.1, with respect to rotationality arising from shocks, are also a very persuasive inducement to adopt some

method of accounting for shocks, especially since these were expected to be stronger in the axisymmetric case. Furthermore, reattachment shocks after the base region and separation bubbles are a basic feature of the flowfield.

The appearance of a shock wave in a MOC solution is signalled by the crossing of characteristics of the same family. If the solution continues to be marched, a counter-streamwise velocity appears and, if the shock is weak enough, a subsequent restoration of streamwise marching occurs. This gives rise to two major problems: firstly, the shock violates a basic assumption of the MOC, that of isentropic flow; and, secondly, the solution becomes triple-valued in a region close to the shock. Although this does not give a unique position for the shock, Chang & Chow¹⁹⁷⁴ found that the foldback method gave a reasonably tight prediction of the shock position and so identification by crossed characteristics of the same family appears a reasonable assumption. Zucrow & Hoffman¹⁹⁷⁶ point out that complexity in logic tends to arise if a Rankine-Hugoniot shock process is used with the MOC to explicitly fit a shock.

The method now used detects the formation of embedded shocks by the coalescing of characteristics of the same family. It continues to march the post-shock characteristic through the flowfield as the shock line and uses the array space which would have contained the other coalesced characteristic to store pre-shock properties. A flag array records the direction ($\lambda^{s+}, \lambda^{s-}$) of the shock on this second characteristic so that it is ignored as a base point for solution marching on subsequent steps. Further coalescing characteristics

of the same family are also set to pre-shock values in this way, so that the characteristic furthest downstream always carries the post-shock property values.

This permits a modification to the basic unit processes described above, in which shock lines are used instead of characteristics to march the solution geometry forward. Figure 4.3a sets out the physical representation used for the modification. Back projection of unshocked characteristics from the solution point to the previous solution line with appropriate interpolation gives starting values to determine the pre-shock solution point properties. A Rankine-Hugoniot oblique shock calculation produces post-shock properties which can then be used to close the equation set by projecting a characteristic of the same family as the shock backwards into the previous post-shock flow solution (since the shock line lies between the pre- and post-shock characteristics of the same family). Iterative application of this scheme is used for convergence. Unshocked characteristics can be regarded as infinitesimally weak oblique shocks (which, of course, lie at the same angle as the Mach lines), and so the normal MOC becomes just a special case of the shocked unit process. In fact, all the unit processes above, including the ones adapted for boundary conditions, were developed so that they could be used either shocked or unshocked.

The computational logic first used to implement the formation of shocks in the flow stored both pre- and post-shock properties at a given shock point in the network arrays at the current solution line. However, this was found to break down rapidly at the formation of shocks, since the geometrical form

of the solution line undergoes severe distortion as the region of characteristic coalescence is approached. A second approach was required in which the characteristics were maintained in the computational domain but superimposed in the physical one (see figures 4.3a and 4.3b). This necessitated a great deal more complexity in the marching routines, including a double sweep at each solution line, the first sweep being for unshocked points, since these were required to compute the shocked points at the same marching step. However, the detection of characteristics swallowed by a propagating shock was eased. The swallowing of pre-shock characteristics in this scheme required some points already calculated as unshocked to be discarded. This resulted in double entries in the log file, which had then to be sorted and false results weeded out before submission to the plot program. This also led to particular difficulties where the method broke down during the propagation of the shock, since some false points had no superceeding correct one and manual inspection of the data file was required in order to eliminate them.

The technique of detecting and incorporating shocks is only valid for oblique shocks producing supersonic post-shock flow, since stronger oblique shocks give subsonic flow and terminate the MOC. Normal shocks are not detected but in supersonic free jet flows they are normally preceded by a strengthening oblique shock in the solution so termination should occur when this produces subsonic post-shock conditions. Hence the failure to detect normal shocks is not a major drawback in the method itself.

4.1.3.5 Shock Interactions

Oblique shock interactions arise at flow boundaries and where shocks cross. The simplest case is that of a shock impinging on a solid boundary and reflecting as another oblique shock, as shown in figure 4.4a. Since there are effectively three fluid states to accommodate at the edge point, and only two of these are accommodated by using the front and rear coalesced characteristics, it would appear that a considerable expansion of array space is required to cope with the possibility of a shock reflection at each edge point. However, the same effect can be attained by adding an extra point at the boundary for the reflected shock points via extra routines, as represented by figure 4.4b. Provided that these additions are flagged in the data output, they can be easily handled by presentation programs. Calculation of the shock system proceeds simply by requiring the flow angle to remain parallel to the surface after passing through the impinging and reflected shocks.

The crossing of oblique shocks of opposite family produces greater problems than the oblique shock reflection, since there are two extra fluid states and the requirement for additional variable storage arises in the centre of the flowfield. Since development time was running short and crossed shock behaviour in the jet was mainly observed in association with Mach (and therefore normal) shock structures which invalidate the MOC anyway, this was left for future development. However, extra swallowed characteristics appear very quickly after the formation of a shock wave, and these could be used to provide the necessary array space. Hunt¹⁹⁸⁰ gives a method of analytical solution of oblique shock intersection using a 10th degree polynomial, but the complexity of the

coefficient derivation (involving multiple matrix inversion) suggests that a more practical computer solution would be by an iterative method based on correcting the predictor exit flow angle by the pressure differential across the slip-line (which should, of course, be zero for a converged solution). This latter method also has the advantage that, should the maximum turning be reached on one of the outgoing shocks before convergence is achieved, this would indicate that the physical flow would actually produce a Mach intersection giving subsonic flow and terminating the applicability of the MOC. The explicit detection of Mach intersections in the Hunt model appears to be less easily accomplished.

A further problem arises because an oblique shock intersection gives rise in general to a slip-line, across which velocity and density are discontinuous. In order to march the solution forward some modification of the unit process would therefore be necessary to take this phenomenon into account. One possibility is available, provided the flow on both sides of the slip-line remains locally supersonic. The problem reduces to that of two boundary-type points of opposing sign. Since the four λ^0 characteristics are coincident with the slip-line, the location of the solution point can be determined by the intersection of the λ^+ characteristic from one side and the λ^- characteristic from the other. Three compatibility equations remain on each side of the slip-line which form a closed set, since the unknown variables are two velocities, two densities, a single pressure and, of course, a single flow angle. Again, this was left for future development.

The above method takes no account of shock interactions with a slip-line. The logical complexity of coping with such an interaction is great unless the interaction is symmetric, as found in free jet flows. In principle, asymmetric interactions could be handled in a manner similar to that used for the shock reflections, but, generally, both reflected and transmitted waves are created, and this gives rise to difficulties in generating additional array space. Since the appearance of slip-lines in the actual flow causes the growth of shear layers which will invalidate the use of the MOC to a greater or lesser extent (and this discrepancy will be greatly enhanced by shock – shear layer interactions), it was thought of little benefit with respect to the overall computational objectives to extend the method for such a flow configuration.

The impingement of an oblique shock wave on a ‘free’ boundary with an undisturbed region requires that the pressure rise across the shock must be cancelled by an expansion to maintain a single-valued streamwise edge pressure. Since this expansion is modelled by a number of discrete waves, it would again appear that a large expansion of array space is required. However, as mentioned above in section 4.1.3.2, this can be achieved by forward loading of the data arrays. One remaining problem is to ensure that the total array space does not grow in an uncontrolled fashion. Since the strength of the impinging shock will have an influence on the number of characteristics which coalesce with it, by discretising the expansion into the same number of waves, the total jet height in the numbering scheme can be held constant. Moreover, this maintains comparability in the modelling of different expansions and permits much simpler presentation of the results.

4.1.3.6 Axisymmetry and Initialisation

In order to proceed with a MOC calculation, certain starting conditions, commonly represented by an initial value line, are required. In the present case of an underexpanded nozzle, expansion processes at the nozzle lip and step (if present) must also be added. These present little problem in the planar case, since a simple wave flow model can be used. Johannesen & Meyer¹⁹⁵⁹ present a calculation for the near field flow in a non-planar supersonic expansion corner. However, Ackroyd¹⁹⁷⁵ demonstrates that, in the limit, the corner at an axisymmetric supersonic expansion is directly equivalent to a planar Prandtl-Meyer expansion. This can be implemented trivially with the Method of Characteristics since the initial conditions remain identical to the planar case and the alteration of the characteristic equations copes with the axisymmetry thereafter.

No such simple relation exists for the exit conditions of the axisymmetric nozzle flowfield required for the initial value line. Norwood¹⁹⁶² matched the subsonic to the supersonic flow by assuming a stream function distribution on the sonic line, using a hodograph solution for the subsonic region and a marching solution for the supersonic and by adjusting the approximation on the sonic line until property gradient continuity was achieved. Carroll & Dutton¹⁹⁸⁵ used asymptotic expansions of non-dimensionalised velocities about the throat to derive an initial value line for an axisymmetric nozzle. Their method may only be useful for nozzles with small turning, but this might be a good approximation near the sonic line in the current case.

However, the insensitivity of the planar calculation to variations mentioned by Gilchrist¹⁹⁸⁵ was taken as an indication that this task could be given a lower priority than other modelling work. Furthermore, the work of Green¹⁹⁸⁷ on a closely similar axisymmetric flare model suggests that a quasi-one-dimensional approach is quite suitable as a first approximation. This approach was first reported in Green & Carpenter¹⁹⁸³. A few cases were tried with data taken from the interferometric studies described below, but, since no great alterations in the MOC networks were thereby produced, very simple approximations were retained for the initial value line in all other cases.

4.1.3.7 Testing

The program modules were tested independently using the IF77 debugging environment (Duncan¹⁹⁸⁷) to ensure correct local and global operation. Test data for non-MOC modules was hand-generated, whilst MOC test data was taken from Zucrow & Hoffman¹⁹⁷⁶, as far as possible, and supplemented by hand-generated data for shock processes.

4.2 BOUNDARY LAYER METHOD

4.2.1 DESCRIPTION

As mentioned in the previous chapter, the basic boundary layer method chosen was the integral formulation reported by Drela & Giles¹⁹⁸⁶, using the Falkner-Skan one parameter family for laminar profiles and the Whitfield, Swafford & Jacocks¹⁹⁸¹ correlations for turbulent profiles, modified for the effects of compressibility. An e^9 transition criterion* was employed, and the

* See page 48

Clauser G- β locus model for equilibrium boundary layers was combined with a simplified version of the Bradshaw and Ferriss stress transport equation to model non-equilibrium turbulence effects through the shear stress coefficient C_τ . Drela & Giles expressed the profile families in the following shape-parameter relationships:

Laminar Modelling:

$$\begin{aligned}
 H^* &= \begin{cases} 1.515 + 0.076 \frac{(4-H_k)^2}{H_k}, & H_k < 4 \\ 1.515 + 0.076 \frac{(H_k-4)^2}{H_k}, & H_k \geq 4 \end{cases} \\
 Re_\vartheta \frac{C_f}{2} &= \begin{cases} -0.067 + 0.01977 \frac{(7.4-H_k)^2}{H_k-1}, & H_k < 7.4 \\ -0.067 + 0.01977 \left(1 - \frac{1.4}{H_k-6}\right)^2, & H_k \geq 7.4 \end{cases} \\
 Re_\vartheta \frac{2C_D}{H^*} &= \begin{cases} 0.207 + 0.00205(4-H_k)^{5.5}, & H_k < 4 \\ 0.207 + 0.003 \frac{(H_k-4)^2}{1+0.02(H_k-4)^2}, & H_k \geq 4 \end{cases}
 \end{aligned}$$

Turbulent Modelling:

$$H^* = \begin{cases} 1.505 + \frac{4}{Re_\vartheta} + \left(0.165 - \frac{1.4}{\sqrt{Re_\vartheta}}\right) \frac{(H_0-H_k)^{1.6}}{H_k}, & H_k < H_0 \\ 1.505 + \frac{4}{Re_\vartheta} + (H_0 - H_k)^2 \left[\frac{0.04}{H_k} + \frac{0.007 \ln Re_\vartheta}{(H_k-H_0+4/\ln Re_\vartheta)^2} \right], & H_k \geq H_0 \end{cases}$$

$$\text{where } H_0 = \begin{cases} 4, & Re_\vartheta < 400 \\ 3 + \frac{400}{Re_\vartheta}, & Re_\vartheta \geq 400 \end{cases}$$

$$\begin{aligned}
 C_f \sqrt{1 + 0.2M_{e\infty}^2} &= 0.3e^{-1.33H_k} \left[\log \left(\frac{Re_\vartheta}{\sqrt{1 + 0.2M_{e\infty}^2}} \right) \right]^{-1.74-0.33H_k} \\
 &\quad + 0.00011 \left[\tanh \left(4 - \frac{H_k}{0.875} \right) - 1 \right]
 \end{aligned}$$

$$C_D = \frac{C_f H^*}{4} \left(1 - \frac{4(H_k-1)}{3H} \right) + C_\tau \left[1 - \frac{H^*}{2} \left(1 - \frac{4(H_k-1)}{3H} \right) \right]$$

where C_τ is modelled as described above

These were then used to close the momentum integral equation and the kinetic energy shape factor equation. Iteration was carried out globally by direct linkage to an Euler equation solver for the inviscid flowfield.

4.2.2 IMPLEMENTATION

The adaptation of the method for the current work requires a separate iteration procedure for the momentum integral equation and the kinetic energy shape factor equation, since the outer inviscid solution is generated by the single-pass MOC. Several routines were written so that the iteration could proceed to match either an externally imposed velocity gradient or displacement thickness growth. As Bradshaw^{1975a} suggests, the use of shear layer axes was adopted for computational efficiency. This helps to isolate the boundary layer calculation from the MOC and also permits simple application of the Mangler transformation:

$$\xi = \frac{1}{L^2} \int_0^s r^2(s) ds$$

$$\eta = \frac{r(s)}{L} n$$

$$u(\xi) = u(s)$$

$$v(\eta) = \frac{L}{r(s)} \left[v(n) + \frac{u(s)}{r(s)} \frac{\partial}{\partial s} (r(s)) \right]$$

from Schlichting¹⁹⁷⁹ for the axisymmetric case.

The iteration proceeds by hypothesising constant shape factor, since this is the most insensitive parameter of the modelling, and calculating the momentum thickness gradient required to meet the external boundary condition from the momentum integral equation. The shape factor correlations and kinetic energy shape factor equation are then used to produce a correction and the whole process is iterated to convergence. In the turbulent case, non-equilibrium equations are also included within the iteration. The whole approach lends itself to modular programming and this was adopted with a view to simplifying

the application of any upstream influence correlations which might later be found necessary.

4.2.3 MATCHING PROCEDURE

One major reason for isolating the Method of Characteristics from the boundary layer method is to retain explicit control over the two iteration processes occurring at each edge point, in order to prevent divergence. Furthermore, this permits the selection of forward mode ($\frac{\partial u_e}{\partial \xi}$ specified by the MOC) in regions of acceleration and reverse mode ($\frac{\partial \delta^*}{\partial \xi}$ specified by MOC) in regions of deceleration, which Ardonceau & de Roquefort¹⁹⁸⁰ suggest is necessary for convergence efficiency. In order to avoid numerical problems, it was found that a constant streamwise increment $\Delta \xi$ had to be fixed from the 'first guess' MOC solution, and thereafter back-projection of the λ^- characteristic to the previous solution line was used to solve the MOC edge. Since, in the main part of the flow, the corrector modifications to the original guess were found generally small, this method was not expected to distort the MOC network to any great extent.

4.2.4 TESTING

The boundary layer modules were tested by transferring them to another program, whose control section was written to handle test data, and then copying back the debugged versions to the Coanda simulation program on conclusion of testing. In this way, it was hoped to increase the flexibility of the testing procedures without generating a significant number of extra error

sources. The laminar routines were tested against data given by Schlichting¹⁹⁵⁵ which was derived using a Pohlhausen method. The result is shown in figure 4.5; the slight discrepancy between the two techniques occurs in the region of adverse pressure gradient, in which the Pohlhausen method is regarded with some suspicion (see section 3.2.1 in chapter 2). The turbulent routines were also tested against data from Schlichting, but this only covered flat plate constant pressure gradient cases, since problems were discovered with the matching process of the laminar solution to the MOC and resolution of these problems was regarded as a higher priority than further turbulent routine testing.

Despite checking both laminar and MOC routines separately, and applying a number of different boundary layer iteration formulations, convergence of the two methods could not be obtained. Further investigation, using experimental pressure distributions, revealed that the MOC and boundary layer calculations ^{as the boundary condition for both zones} gave different values of layer thickness (see figure 4.6), regardless of the estimate used for the incoming boundary layer. The possible reasons for this behaviour are discussed in chapter 9 below.

4.3 PRESENTATION PROGRAM

4.3.1 OBJECTIVES AND STRUCTURE

The primary objective in the production of the presentation program was to ensure, as far as possible, that experimental and computational data received the same treatment, so that results could be directly compared. This

was also to reduce the effect of any undiscovered bugs, although much effort was expended in testing to discover and correct errors. Accordingly, the program was arranged around the data arrays for fluid properties such as pressure, density and Mach number, and the data of each type was converted for identical storage, regardless of source. The source was used only to set flags for the various legends required on the plots.

The second objective was to isolate the type of diagram produced from the data type. This was achieved by using modular routines, with much the same practical advantages in terms of testing as found above in the computational program. Since direct transfer of the presentation program to the industrial sponsor was not envisaged, no special effort was made to condense it, unlike that made for the computational work. The GHOST80 graphics system, as described in GHOST Manual¹⁹⁸⁵, was used to generate the plots, since, out of a number of possibilities, this subroutine library was the one most closely integrated with the FORTRAN77 compiler used for the program.

At a later stage in the project, the computational work was ported to an Apple Macintosh computer, and, in order to speed the conversion, plot coordinates were output in the internal form of a computer-aided design package for annotation. This approach proved particularly convenient and is therefore recommended for any presentation of fluid dynamic results.

4.3.2 COMPARISON AND PRESENTATION

The usual form for presenting computational data is to focus upon

some phenomenon or coefficient of interest and to compare experimental and computational figures. However, Settles¹⁹⁸⁶ recommends the use of graphical presentation techniques in fluid dynamics for both experimental data and computational results to permit ready assimilation of the large quantities of information involved. The application of both methods is described in the following sections.

4.3.3 PRESENTATION FORMATS

4.3.3.1 Surface Pressure Plots

The surface pressure plots were produced as a graph of surface pressure (non-dimensionalised using $C_p = [p - p_{atm}]/[p_* - p_{atm}]$) against angle around the Coanda surface in order to permit ready comparison between axisymmetric and planar versions with varying geometries and driving pressures. Discrete data from interferometry, MOC calculations or direct experimental readings were used to generate cubic B-splines (NAG Library¹⁹⁸⁸), which in turn were used to generate plot coordinates. Several graphs could be combined on one page to permit easy comparison and to save space.

4.3.3.2 Contour Plots

The data from interferometry digitisations or from MOC calculations for flowfield properties take the form of irregularly distributed discrete values. For processing, most contouring packages (and particularly GHOST80) require some semblance of regularity in the data, and thus interpolation becomes necessary. The program uses standard routines which weight the influence of irregular

points on the regular grid values by the inverse of the fourth power of the distance between them. The GHOST Manual¹⁹⁸⁵ recommends this technique for data grouped along lines – the obvious selection for interferometric data and almost as obvious for MOC data. The weighting process is ignored where an irregular data point falls within a small ‘capture’ radius of a regular grid point.

Difficulties arise with the above method where there are discontinuities within the regular grid space. Flow boundaries comprise one such discontinuity, which can be overcome to some extent by adding dummy data points interpolated from adjacent flow regions to cover the non-flow region. Unfortunately, flowfield discontinuities such as shocks cannot be treated in this way and some smearing is unavoidable. Insufficient time was available to modify the interpolation routines and, in the author’s opinion, a better use of effort would be the production of a set of contouring routines suitable for irregularly spaced discontinuous data. This is a fairly common requirement, not just in supersonic fluid dynamics, but was regarded as outside the terms of reference of the project. In order to prevent the dummy data producing contours, the flowfields were plotted a number of times with the application of a series of masks to restrict visible output to regions of flow only.

4.3.3.3 Simulated Visualisations

The distortion of a plane parallel light beam by a field of variable refractive index can be regarded, if the deflections are small and input and output beams discretised, as a non-conformal mapping (*i.e.* one output element

may be the result of several input elements). The practical upshot of this is that for a given refractive index field, an incoming beam can be more or less simply analysed to predict the resultant outgoing beam. But the reverse case (the derivation of a refractive index field from incoming and outgoing beams) is impossible to achieve with any great certainty, and the greater the flowfield complexity, the worse the problem becomes.

Hence when the computational results can be cast in the form of a refractive index field (readily derived from the density field for most engineering gases) and the experimental data is in the form of light beam intensities (as is the case with schlieren or shadowgraph photographs), the sensible approach is to predict the *expected* experimental result to confirm its correspondence to the actual experiment. Jenkins¹⁹⁸⁸ took precisely this approach with predicted shadowgraphs from computational models of Rayleigh-Bénard convective flow.

Hesselink¹⁹⁸⁸ gives a wide-ranging review, which includes the latest presentation techniques for fluid dynamics results. Although a good match between computed and experimental visualisations is not conclusive evidence of accuracy, it is nonetheless highly persuasive, especially in a very complex flowfield. By contrast, a poor match provides little direct indication of the deficiencies of the computation (or, conversely, the unappreciated error in experimental technique.)

The routines written for the current program to produce such predictions have so far only reached the stage of modelling thin planar refractive index

fields. In addition, no time has been available for properly debugging the routines, so their application has been left for future development.

4.3.3.4 Breakaway Plots

Since the amount of data to be manipulated for plots of breakaway and reversion is minimal, a separate program was developed for this purpose, so avoiding the extra complexity of the control logic needed for incorporation in the main program and thus speeding compilation and running time. This approach is supported by the lack of the direct comparability which exists between this and other data types handled by the main presentation program. Originally, isometric 'surface' plots were used to simultaneously present the effect of varying slot and step sizes. Although the data is discrete, no experimental evidence was discovered invalidating the assumption of a continuous effect of geometry variation, so a bi-cubic B-spline surface was used to interpolate the data. However, the presentation format was later changed to labelled multiple graphs. This sacrifices ease of comprehension for ease of quantitative comparison, but this was not thought a great disadvantage for the current work.

4.4 HYSTERESIS SIMULATION

The first stage of confirming the MOC's validity for hysteresis simulation was to model the separated jet using experimental data. The procedure used by Gilchrist's program was based upon changing unit processes from surface points to pressure-matched separated jet points at a specified separation angle

supplied by the program user. As described above, a new method was developed which matches the flow to the experimental surface pressures, assuming the flow is separated, and recalculates if the resulting solution point lies inside the wall. The second calculation uses the wall geometry for position but retains interpolated experimental pressure. The separation position is thus dependent purely on the calculation and experimental data, avoiding explicit specification of the separation position.

Since the boundary layer model detailed above appears to require a considerable amount of further work before it can be applied, a simple model was tried in an attempt to provide a preliminary *prediction* of the breakaway condition. Since the point at which the jet separates from the surface is observed to be close to the end of the first expansion cell, it was reasoned that initial separation of the boundary layer causes sufficient upstream disturbance to propagate the bubble until a point is reached where the potential core flow imposes a strong expansion upon the boundary layer. By comparing pressure changes along the surface with those along the incoming characteristics it is possible to detect the point on the surface where the core flow ceases to impose expansion on a hypothetical boundary layer and thus to initiate separation. The pressure in the bubble is equated to that at separation and the solution marched using a process equivalent to that for the outer jet edge. It is argued that when this assumption fails to produce a closed separation bubble it will indicate physical breakaway. Furthermore, the model should indicate very slight separation at the reversion pressure (at which the breakaway of the

jet must be physically overwhelmed by entrainment of the recirculating layer, causing reattachment to propagate downstream).

A manifest attraction of this initial prediction of the surface pressure distribution (if reasonably accurate) is that it could be combined at some later stage with a boundary/shear layer model to refine the detail of the separation bubble at separation and reattachment. This would permit another possibility for establishing the reversion limit, since a bubble pressure of p_{atm} could be applied and the resulting flow angle compared with the empirical findings of Sirieix¹⁹⁷⁵, to establish whether reattachment and subsequent reversion of the jet were feasible.

From the experimental surface pressure readings, it became apparent that first separation was taking place at roughly the same value of *favourable* pressure gradient in both axisymmetric and planar cases. When applied to the planar case, the separation point varied little from that predicted with the above pressure criterion, but in the axisymmetric case much earlier separation occurred. As one would expect, this gave results which are more in line with the visualisation data. Further discussion on this point is reserved for later.

5 EQUIPMENT DESIGN

5.1 BACKGROUND

5.1.1 VISUALISATION METHODS

5.1.1.1 Shadowgraph and Schlieren Techniques

The main techniques used for visualisation were the schlieren and shadowgraph methods. The equipment used was described by Gilchrist¹⁹⁸⁵. Both methods are based upon the refraction of light passing through an object with gradients in its refractive index. In the case of the flow of a transparent fluid, these gradients are generated by density changes, which, for an ideal gas, give a conformal (mono-valued) mapping to refractive index. It is not proposed to give a thorough description of these methods, since this can be found in a standard textbook on flow visualisation, but a brief overview will be set out below.

A shadowgraph visualisation is the result of focussing or dispersion of parts of a probe beam traversing the test section by flow regions with strong curvature in the refractive index profile. As will be demonstrated later, this

does not require stringent control over the collimation or uniformity of the probe illumination, but where such control is exercised the quality of the visualisation is naturally much improved.

The relative simplicity of this method is counterbalanced by the fact that, although the mapping from density to refractive index is single-valued (at least for the gases involved in this investigation), the corresponding mapping from refractive index to illumination level is not. Consequently, the derivation of quantitative data requires detailed knowledge of the structure of the probe beam, exact determination of the behaviour of the optical system and intricate iterative processing of the results, even for true planar flowfields. Even so, there exists the possibility of non-unique solutions for the density field, and, moreover, the resolution of the system will be poor where the curvatures of density are small. It was therefore decided that the considerable effort which would be required to implement a measuring system could not be justified in the current work.

In schlieren techniques, the deflection of the probe beam is rendered visible by introducing an element into the optics after the test section which produces some variation of the illumination, depending on the path of a ray through it. Comparison of the pattern induced by the flow with the basic pattern induced by the optical system is then possible. Normally the base pattern is set to a very simple and convenient layout such as nominally uniform illumination or zero illumination. The sensitivity of the method can be varied by adaptation of the optics to produce different ray deflections or, much more

efficiently, changing the illumination variation element to alter the response to an identical ray deviation. In the current method, this element is a knife-edge placed at a focussed point of the probe beam after the test section so that a certain proportion of the rays passing through each point of the flowfield are cut off. A variation in the deflection of a ray perpendicular to the knife-edge will then produce more illumination at the viewing screen if it is moved from the cut-off zone to the transmitted region or less if moved in the reverse direction. The general effect is to produce results which respond to the gradient of refractive index (to a first order approximation).

Quantitative analysis of schlieren results requires apparatus for the assessment of the illumination levels (usually directly from the photographic negative) and data capture. This is prohibitively expensive for a single project. Furthermore, the inclusion of a calibration element of known refractive index gradient somewhere in the image is required. While this would have been possible (if expensive) with the planar model, the inclusion of a calibration element in the axisymmetric model without disturbing the flow would have caused extreme difficulty. Furthermore, a number of different elements would be required to cope with the different sensitivity requirements of the rig, and to provide for convenient changes between individual runs would have been tricky, even for the planar model case. The problem is further complicated by the need for precise alignment between images so that the deviations caused by the optics alone can be removed by comparison with the 'no-flow' picture. The recording medium must also possess adequate uniformity. In spite of the above difficulties, the potential benefits in terms of the results obtainable are extensive,

and this modification could be worthwhile in the context of infrastructural development.

In view of the excellent performance of the pre-existing monochrome system, any upgrade would have to demonstrate significant advantages. The knife-edge element obviously produces a significant reduction in the total light transmission of the system, which could be increased by the use of a half-filter. This would reduce the contrast at the film plane, and, since enough light is available from the light source even for spark exposures, this is not a pressing need. A graded filter would produce the same effect but simultaneously control the sensitivity of the method, which has to be adjustable in order to cope with wide variations in flow gradients. A series of filters would therefore be required.

Shaped filters or edges could be used to produce variation or superposition of the direction of the refractive index gradient to which the method responds. This could produce difficulties in interpretation, since various wave systems coincide in the flare model and it would be possible for the effect of the gradient in one direction to cancel the effect in the other. This problem could be eliminated by using some type of colour schlieren technique, of which Settles¹⁹⁷³ gives a classification. However, the added cost of a new multi-chromatic probe beam source and more expensive data acquisition media is not thought worthwhile, given the limited potential benefits from the change.

5.1.1.2 Surface Flow Visualisation Method

The method used for visualisation of the flow at the Coanda flare surface was the application of a high viscosity oil pigmented with a fluorescing dye. Gilchrist¹⁹⁸⁵ and Lamont & Hunt¹⁹⁷⁶ also used this 'Dayglo' pigment, oil and ultraviolet illumination for flow visualisation. This method is extensively applied where major changes in the flow direction are expected, such as at separations and reattachments. It is used in this project as back-up evidence for the other visualisations and measurements, and to provide a qualitative appraisal of the extent of three-dimensional disturbances in the model flowfields.

There are a number of limitations to the above technique, the principal one being that it is invasive and can show false results, particularly when the flow is sensitive to small disturbances. This sensitivity appears especially at separation and reattachment points, but, fortunately, as the separation scale grows, the inaccuracy generally reduces. A secondary problem is that the fluid dynamics of the oil/tracer mixture can also produce visualisation patterns that obviously do not correspond to the true behaviour of the flow under investigation. The streaking and bunching with insoluble tracers (as is partially the case for the dye used in the current work) mentioned by Merzkirch¹⁹⁷⁴ comes within this category. Settles¹⁹⁸⁶ points out that surface fluid flow visualisation has essentially zero time response and therefore conceals unsteadiness. However, the comparison of spark and long exposure shadowgraph and schlieren should reveal any such behaviour and so short time response is not required from the oil technique.

5.1.2 METROLOGY

5.1.2.1 Interferometry

The interferometer used is that reported by Gregory-Smith, Gilchrist & Senior¹⁹⁸⁹. It is based on the schlieren optics with additional beam splitting facilities, and operates in the finite fringe mode for accuracy. Data analysis, described in detail later, is achieved by digitisation of fringes.

Ben-Dor, Whitten & Glass¹⁹⁷⁹ say that the assignment of fringe number is still likely to be done manually, particularly in complex flowfields. Arzoan & Ben-Dor¹⁹⁸⁶ claim to have used a fully computerised system, but their paper reveals its application only to a very simple case of a normal shock, and, furthermore, the cross-shock fringe tracing was done manually, using a cursor to 'correct' the digitised image for missing information. Whilst appreciating that their method gives a considerable increase in the efficiency of interferogram processing, the basic assignment of fringe numbers was still effectively manual. Stricker & Kafri¹⁹⁸² mention three methods of identifying fringes: following through from an undisturbed region spatially, following through temporally by observing unsteady evolution of the interferogram or by reducing the sensitivity to get small deviations. Boyd, Miller & Ghiglia¹⁹⁸³ describe a very high resolution system for direct capture and edge detection of fringes, but the cost of such a system would be prohibitive for all but the largest specialist fluid dynamics laboratories, quite apart from the fact that computerised vision systems are currently a major research area in their own right.

The main theme of Stricker's & Kafri's¹⁹⁸² paper is the application of moiré deflectometry to axisymmetric flows, which they show relates the fringe shift to density gradients rather than density, thus making the the Abel transform which they used less prone to discretisation errors, and permitting quantitative mapping. However, they mention that considerable contrast reduction was observed in turbulent zones of the flowfield, therefore, since the INDAIR model is known to generate strong mixing layer turbulence, this method was not likely to produce any great improvement over conventional interferometry.

Stricker, Keren & Kafri¹⁹⁸³ give an iterative algorithm for the simplified interpretation of axisymmetric interferograms in conical flow. Dunagan, Brown & Miles¹⁹⁸⁷ present another method of inverting the Abel transform which arises in the interpretation of the axisymmetric flowfield. Havener¹⁹⁸⁸, however, following Bradley and Hildebrand, uses an alternative transformation and inversion which are reported as reducing the effect of inaccuracy in fringe number measurement. This latter method is used for axisymmetric turbulence, a very severe test. The general complexity of obtaining accurate results from direct interferometry of the axisymmetric flow suggests that an examination of an alternative technique is warranted.

5.1.2.2 Nephelometry

Another possibility for measurement is to use a flow tracer nephelometry technique with appropriate time steps to produce quantifiable data by applying similar processing to that applied to interferograms.

In order to use this technique in an open loop system, either the tracer contamination must be acceptable or a recovery technique must be used. Many of the seeding media so far used, such as sodium (Settles¹⁹⁸⁶), are clearly unsuitable for discharging into the laboratory atmosphere in the quantities which would be required for the Coanda model. Even relatively innocuous tracers such as the talc used by Page & Przimbil¹⁹⁷⁵ to highlight separated zones would cause problems at the large flowrates involved. To limit the amount of tracing medium used, Voisinet¹⁹⁷⁵ injected the tracer through surface pressure tappings. Although this could be used to highlight the separated zones in the current case, alteration of the flow due to injection could be substantial, especially close to breakaway conditions. If the mixing process in the separated bubbles is weak enough it may prove possible to retain visualisation contrast with intermittent seeding through a pressure tapping, thus minimising flowfield distortion.

Accurate quantitative information from tracer nephelometry is difficult to obtain, owing to particle lag (Catalano, Morton Humphris¹⁹⁷⁷), which presents even greater problems in supersonic flow. Stanislas¹⁹⁸³ reports an approximate upper limit of 300 m/s with oil smoke in CO₂. Vest¹⁹⁷⁹ gives a description of a method using laser speckle generated by the molecular scattering of an planar laser sheet, thereby using the fluid itself as the flow marker to circumvent the problems posed by foreign tracers.

In high speed flows exposure times become very short, requiring both intense illumination and very high response switching of the source. Estimates

by Settles¹⁹⁸⁶ suggest that up to 4 W of laser power is required for illuminating slices, well above the capability of current equipment. Vest¹⁹⁷⁹ gives equations for the exposure requirements using speckle as the tracer. For the current problem the required shutter frequency response is in excess of 40 kHz. Up to now this has been achieved mainly by using pulsed lasers or electro- and acousto-optic shutters (see Whiffen & Ahuja¹⁹⁸³ for a fluid dynamic application). Both illumination and pulsing would require the purchases of equipment costing several thousand pounds, which is not justifiable for the purposes of the current work.

Lourenco *et alia*¹⁹⁸⁶ were successful with a method of interferometric analysis of a nephelogram based on the generation of Young's fringes by a reference laser beam travelling through the triple-exposed image. The speckle images could be processed in the same way. This paper also points out the advantages of contrast enhancement by photographic processing, which is applicable not only to metrology but also to the other photographic techniques described above.

5.1.2.3 Other Methods

The last method applied to the Coanda model was the provision of surface pressure tappings. These are relatively reliable for the measurement of time-averaged static pressures of the near-wall flow, provided that the momentum normal to the wall is negligible. This is likely to be a good approximation, apart from the immediate vicinity of separation and reattachment, where small errors might be expected.

Other direct measurements at the surface by shear gauges, heat transfer gauges and the like could only be achieved at high cost, since the movement of important features in the streamwise direction would require the instrumentation of a complete strip. The complicated geometry, particularly in the axisymmetric case, would further increase the costs. Commercial temperature-responsive coatings are too insensitive to produce anything more than qualitative results.

A laser doppler anemometer was installed in the laboratory, but the system was under development and in full time use for another project unconnected with the Coanda flare programme. The possibilities of using this system for fine resolution measurements in both temporal and spatial domains were therefore left for future investigation.

5.2 VIBRATION ISOLATION

5.2.1 DESIGN MOTIVATION

The motivation for the re-design of the mounting systems for mechanical and optical rigs was to eliminate the effect of vibration on the interferometer reported by Gilchrist¹⁹⁸⁵. The vibration effectively rendered the interferometer inoperable at pressures exceeding the choking ratio for the flare model nozzle.

Originally, the mechanical rig was supported by a rigid tripod attached to the bottom of the riser tube and composed of 13mm square section rolled steel tubing. This was supplemented by a rigid strut of the same material, connected directly to the riser tube at one end and to the wall at the other. The strut was placed to resist forces normal to the Coanda surface. The wall

and floor fixings were made with masonry bolts, and the tripod fixings were very close to the legs of the wooden laboratory benches carrying the optical rig. No adjustment in the support work was provided for alignment purposes.

The optical rig was raised to the level of the working section by small wooden platforms. Anti-vibration feet were placed between the platforms and the optical benches. The feet were built essentially from undamped metal strip springs. A considerable amount of vibration was apparent in the mechanical support work when the airflow was turned on, and given the rigid joints at the floor and wall it was suspected that this would be transmitted. No transmission was detectable by hand on the wooden benches or platforms but at the base of the optical rig feet vibration was detected. This was attenuated but not eliminated on passing through the suspension element of the feet.

The specification of the feet was based on typical laboratory duty, which was inadequate for the strong vibration encountered. The options open for consideration for eliminating vibration were therefore to reduce the transmitted vibration from the mechanical rig and/or to provide additional isolation for the optical rig. Since movement of personnel and other environmental vibrations appeared to have little effect on the interferometer it was decided to improve the mechanical rig support work first.

5.2.2 MECHANICAL RIG SUSPENSION SYSTEM

The primary design aim was to reduce vibration normal to the floor and wall surfaces, since torsional vibration forces on the flare model were expected

to be quite small as a consequence of the symmetry. Subsidiary objectives were to provide some adjustment for alignment and to make the suspension readily convertible for installation of the axisymmetric flare model.

The design adopted is set out in figure 5.1. The rubber-to-metal bushings were Ford automobile parts designed for torsional stiffness about their central axis. They were much less stiff under axial forces (the direction in which they are used). In rubber, both material properties and shape changes combine to give a non-linear force/extension curve but an approximate elastic constant of 65 kN/m was used for calculations. The system was further simplified to a single mass-spring-damper system for linear vibration, with no account taken of the wall restraint. Material damping by the rubber was estimated from data given in Harris & Crede¹⁹⁶¹, which was also used as the source for the calculation technique. The following results were obtained:

Forcing Vibration Hz	Damping Coefficient ζ	Energy Transmitted %
200	0.025	3.38
400	0.040	1.07
800	0.060	0.57
1200	0.080	0.48
1600	0.100	0.47

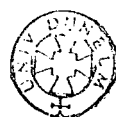
Table 5.1 Mechanical Rig Vibration Transmission

The corresponding natural frequency was calculated at approximately 35 Hz, which was much lower than the expected flowfield fluctuation rates and also substantially less than the film exposure time. The original design envisaged the use of dampers in the legs (shown in chain lines in figure 5.2).

These would have been easily tunable by varying the viscosity of the damping fluid or the resistance of the pistons. However, the system was first tested for the acceptable working section vibration without dampers. Fortunately, this proved to be the case, since extra damping would have increased the energy transmission from that quoted in table 5.1, and the cost of providing the pistons was thus avoided.

The lateral resistance of the bushes depended on load angle, in consequence of the 'pocketing' shown on the sectional view in figure 5.2. Thus the torsional elasticity of the assembly about the axis of the riser tube was tunable by appropriate rotational positioning of the bushes in the leg structures. The maximum stiffness position was chosen but expansion of the flexible tube from the air supply necessitated the provision of additional torsional restraint in the form of foam rubber blocks between one leg tube and the incoming pipework.

The effect of the wall strut in axial and torsional directions was minimised by isolating the connection to the riser tube with foam rubber blocks. The strut itself was modified to give length adjustment. Torsional adjustment was provided by the oversized holes in the base plate, and height and levelling adjustment by the threaded rod connection between the bushes and the base plate. Conversion for the axisymmetric rig was achieved merely by replacing the baseplate. The interferometer was tested with the new mechanical rig suspension in place, and, although some improvement was apparent, it was insufficient for a full test program.



5.2.3 OPTICAL RIG SUSPENSION SYSTEM

In conversation with Dr. H.K Zienkiewicz of Exeter University, it was established that anti-vibration feet similar to those used in the rig had also been found ineffective in a chemical engineering laboratory application. The solution adopted at Exeter had been to provide balloon tyres for the trolley on which the interferometer was mounted and partially deflate these when operating to provide an extremely low transmissibility. The problem had been further reduced by using stiff mountings to minimise the the vibration of the optical components, particularly mirrors, relative to the optical bench.

In the current apparatus the existing component mountings appeared to be fairly stiff, so attention was paid to the rig feet. After checking their positions it was found that the placing of the feet was resulting in uneven loading, although no foot was loaded above its specification. Additional feet were added and the distribution changed but this did not alleviate the problem. Working from the Exeter experience of extremely low mounting stiffness, foam rubber sheeting was introduced underneath the rig feet. At normal density this could not be made thick enough without an unacceptable reduction in the stability of the optical rig. However, a combination of 6 mm rubber mats and high-density reconstituted foam blocks 75 mm thick was successful in completely eliminating the vibration problem.

In retrospect, the foam blocks may have been enough to eliminate the vibration without taking the other measures, but alteration of the support work for the mechanical or optical rigs would still have been required to match

the changed height of the optical axes and to cope with the axisymmetric flare model. Furthermore, by redesigning the mechanical suspension, alignment adjustment capability was added and disturbance to other equipment in the same laboratory from the mechanical rig vibration was reduced.

5.3 SHADOWGRAPH EQUIPMENT FOR FULL-SCALE TESTS

In order to confirm that full-scale flares produced flowfields comparable to those observed in the laboratory, consideration was given to the application of flowfield visualisation techniques to an I8 flare running at a British Petroleum test site. Any method chosen would have had to be successful in daylight but could not rely on direct solar radiation for its effectiveness, since only a few fixed opportunities were available for performing the tests.

Interferometry and schlieren visualisation were rejected as being too complex and expensive to use in a field trial. Suspended particle tracer techniques were rejected, owing to the excessive flow velocities encountered and the difficulty of safe introduction into a combustible gas.

The first technique tried was the use of distortion of the reflected light from a background passing through the flowfield. A striped background technique was tried, as recommended by Settles¹⁹⁸³ for situations unsuitable for complex optics, but satisfactory results were elusive, despite the use of a range of patterns and spacings. Since a vague daylight-generated image was noticeable without equipment during trials of the grid technique, it was decided that shadowgraph held out a better prospect of success.

Schmidt & Shear¹⁹⁷⁵ used a fresnel lens to achieve spatial separation of the visualisation light source and the flowfield luminance of a muzzle blast. The position of the lens was arranged so that the source illumination was collimated at the target, but the blast light, being positioned inside the lens focal length, was diverged, and contrast between the two was maintained. This technique could not be used in the present case, since the background illumination, by definition, could not be placed as required.

Since spatial methods appeared unworkable, either intensity and/or spectral discrimination was required from the apparatus in order to provide the necessary contrast with ambient illumination. Since the solar spectrum is weak in the blue wavelengths, this would have been the ideal colour for a source, but sources with strong emission in this waveband rely mainly on arc discharges. Their use would have compromised safety at the test site and would have required a extra expenditure, since no suitable arc lamp was available from existing equipment stocks.

Two halogen lamps were tried in combination with cheap PMMA fresnel lenses for producing the working beam. A 60 W automobile headlamp did not provide enough contrast and a 500 W site lamp bulb was not sufficiently compact to produce acceptable collimation of the beam. Final success was achieved with a 500 W slide projector set at its longest range. This did not give a collimated beam but did produce a reasonable transmission shadowgraph when the flowfield was photographed against a dark background.

Both ciné and still cameras were used for recording shadowgraphs. These were mounted as close together as possible to obtain roughly the same viewpoint. General orientation was arranged so that the sun was behind the cameras to increase contrast and avoid glare. The light source was placed behind the flare and level with the flowfield and cameras, in order to eliminate direct radiation in the image. The distance of the source was largely determined by the support structures available on site, and by safety requirements. The correct angle necessary to produce a good shadowgraph was found by adjusting the position of the cameras and the contrast screen, as these were mounted on movable supports. Since only qualitative information was sought, no attempt was made to refine the technique further. Exposure of the still Ilford PAN-F 50 ASA film was left to the automatic program of the camera. The ciné film exposure was also set automatically.

More recently, a projection shadowgraphy technique suitable for field tests has been developed by Parthasarthy, Cho & Back¹⁹⁸⁷, using a proprietary reflective screen and flash illumination to overcome the contrast problem.

5.4 PLANAR STEPPED RIG DESIGN

5.4.1 DESIGN OBJECTIVES

Previous work by Gilchrist¹⁹⁸⁵ had been performed on a planar model of the flare which had a smooth transition from nozzle to Coanda surface. During the period of his project a modification was introduced to the industrial flares in the form of a step at the nozzle exit (see figure 5.3). This had the

effect of greatly increasing the blowing pressure required to make the jet break away from the flare surface. It was decided that a study of a planar model of the modified flare would be needed to provide results for verification of calculation techniques. Furthermore, by comparing stepped model results with the unstepped ones it was expected that considerable light would be thrown upon the mechanism of breakaway.

A number of requirements and opportunities was thus presented in the redesign of the planar model. Firstly, the new model was to be comparable with the unstepped one, and this fixed the dimensions and necessitated provision of a zero step setting. Since the use of fixed step pieces would have been costly in both money and operational time, a variable step was specified. Gilchrist¹⁹⁸⁵ mentioned that interpolation of surface pressure results had been necessary and that the tappings had disturbed the flowfield slightly. There was thus an opportunity to reduce these problems by redesign of the pressure tappings. In order to reduce costs, as many parts of the existing model as possible were used, which, incidentally, promotes interchangeability of the models, should this become desirable. It was also proposed to take advantage of the redesign to alleviate contamination of the optical windows as far as possible.

5.4.2 ADOPTED SOLUTION

The design resulting from the above specifications is laid out in figure 5.3 as a general assembly diagram. It should be noted that the backplate was made by modifying that of the unstepped model. The step plate concave surface was designed to match the analogous contour on the unstepped model

so as to give an identical nozzle shape when assembled. The Coanda surface piece was also designed as an exact geometrical match to the unstepped model. Sharp edges were specified at the lower edges of the step and the Coanda surface to avoid disturbance to the flowfield at the zero step setting.

The surface tappings on the Coanda surface were placed in a tighter pattern to give 3° intervals up to 70° around the curved surface, 5° increments from there to the flat surface and 5mm steps on the flat surface. The distribution of the tappings across the surface was arranged to avoid the area of end wall effects, which were expected to be much larger, owing to the presence of the step recirculation zone in addition to surface separation. The hole sizes were reduced to 64% of the area of those in the unstepped model by inserting clock bearings into drilled holes and machining these flush to the surface profile. The bearings were available in brass or hard bronze, and the latter was chosen, being the closer match to the machining characteristics of the mild steel used for the other components. Semi-rigid polyethylene tubing was chosen for connecting up the tappings, in preference to the flexible variety used for the unstepped rig. Although more care was necessary when threading the tubing through the backplate to avoid crushing, better resistance to pressure differential caused by the sub-atmospheric pressures from the model surface was obtained. The tubing was joined to the pick-up holes using short lengths of stainless steel hypodermic pipe glued into the surface with cyanoacrylate adhesive.

Tappings were also placed on the front surface of the step to allow measurement of the pressure inside the step recirculation zone. A distribution of tappings was required to establish that the first one (at the step corner) was not significantly affected by the structure of the separation at a large step height. This was then taken as justification for its accuracy at smaller step heights. In order to allow access for drilling the holes intersecting the tappings, the step plate was designed in two parts, which were assembled and glued before final machining to size. The same clock bearing design was used for all these tappings, except those closest to the nozzle edge, for which a spark erosion machine was needed to pierce holes of the appropriate diameter, at a much greater cost per hole.

A new micrometer carrier was produced to permit accurate adjustment of both step height and slot height (after setting the zero accurately using slip gauges). Feed screws for the step plate and the Coanda surface were integrated into this clamp to aid positional adjustment. Sealing was achieved, as before, by using lengths of O-ring material in milled grooves, but the mating surface between the Coanda surface and step plate was left plain to maintain geometric accuracy once assembled.

Since some of the intended tests did not require optical measurements, a pair of 25 mm perspex side plates was made for these tests, in place of the steel pair carrying the precision windows. The perspex plates were less stiff, but observation of the seals through the perspex during operation did not

reveal leakage paths. The perspex windows were easily cleaned and therefore speeded completion of the test program.

5.5 THE AXISYMMETRIC MODEL

5.5.1 DESIGN OBJECTIVES

Two major objectives motivated the performance of laboratory tests on an axisymmetric flare model. The first of these was to simulate the flowfield of an industrial flare, in order to study in detail the structure and breakaway behaviour of the jet. The second objective was to establish a body of data with which to compare the computational modelling.

A number of subsidiary criteria was set out to fulfil these points. It was proposed to maintain the two-dimensionality of the flow as far as possible, since numerical solution using a three-dimensional code would have been neither practical nor warranted, as no indications of significant three-dimensional effects on breakaway in the real flare had been revealed in other axisymmetric studies (Green¹⁹⁸⁷ and Senior¹⁹⁸⁶). In the industrial flares the axisymmetric nozzle is of simple geometric form, which produces considerable disturbance of the flowfield due to both viscous interactions and wave processes. This was to be avoided in the laboratory model. Good optical and pressure measurement resolution of the flowfield were regarded as important features in the design process. Consideration was also given to the protection of the surrounding environment from noise and airstream impingement.

5.5.2 ADOPTED SOLUTION

The solution adopted to satisfy the design criteria is presented in figure 5.4 as a general arrangement diagram. Its main feature is the complete 360° axisymmetry of the tulip, which affected almost all of the rest of the design. This choice was made in order to avoid both end wall effects, which would be produced by a half-model, and the purchase of optical windows, which a smaller sector would entail. Furthermore, there is considerable evidence (quoted in Chapter 2) that three-dimensional effects in separated regions are enhanced by end walls. Also, Morrison & Gregory-Smith¹⁹⁸⁴ report interference from the base plate boundary layer in a half-flare model, and this was taken as strong persuasion for adopting a full model. Finally, direct comparison with other studies would be vitiated unless full axisymmetry was chosen. The actual shape of the tulip was derived by scaling down an I33 flare design marketed by Kaldair Ltd. to maintain comparability with the industrial flare.

The flow capacity of the model was calculated by a quasi one-dimensional choked nozzle approximation with the throat at the slot exit. Operating pressures were taken from breakaway results of British Petroleum field trials (British Petroleum¹⁹⁸⁰), applying the suggested correction for gas properties. The size was chosen to match the air supply (with modifications described below), giving a larger throat area than in the planar models.

The profile of the nozzle was designed to give the throat at the slot exit and to minimise disturbances arising from the internal acceleration, which affected the external flow. This was achieved by using a FORTRAN77 program to

fit cubic splines through user-specified points on the flow boundaries, providing continuity of curvature, which spreads out the acceleration and the turning of the flow. The objective of the nozzle design was to avoid the considerable disturbance to the external flow which emanated from inside the flare nozzle in the work of Green¹⁹⁸⁷, and which are ascribed to the effects of curvature discontinuity in the nozzle.

Another program was then used to check the area ratio to ensure an S-shaped contraction curve. The process was repeated with alterations to the specifying points. Four points on the shaft profile and three on the lip profile were required to reach a satisfactory solution. A third program took the solution as a basis for generating the co-ordinates for the numerically controlled lathe which was used to manufacture the shaft and the lip tube.

The shaft was designed as the central reference and support member for the model, since this approach permitted the independent variation of slot height and step height and reduced the complexity of providing these adjustments. Moreover, the problem of sealing could be reduced to three joints for which O-rings were specified; heavy duty rings for the main seal and lip tube seal (which were under large positive pressure), and a light duty ring for the tulip bowl seal (which was mainly under negative pressure relative to atmosphere).

Concentricity between the shaft and tulip sub-assembly and the lip and main tube sub-assembly was maintained by the spider piece, which also provided axial support. Checking of concentricity after final assembly was made possible

by provision of a register diameter on the lip tube, which matched the step diameter. The use of an O-ring to seal the main tube joint permitted the clamping force to be transmitted through the spider. The support design calculation was for spider stiffness using an encastré beam simplification. The spider was hand-filed after machining to attain a streamlined leg profile in order to minimise disruption to the riser tube flow. The first contraction from riser to lip tube was provided to damp down any such disturbance and produce a favourable pressure gradient to attenuate the effect of the incoming boundary layer.

The choice of a 360° model posed considerable problems for fitting the pressure tapping tubes, since no access to the rear of the Coanda surface was apparent on first inspection. The model flare tip was designed as a two-component assembly to overcome this problem, but the break had to be carefully placed so that no major flowfield modification occurred. The flat surface was chosen as the location for the joint so that all the tubes could be connected to one component, and so that any discontinuity in the profile would be well away from the zone thought to affect breakaway. The industrial flares were constructed in a similar manner, with a dressed weld at the joint, so that comparability was maintained. A small witness mark was added to the surface to ensure consistent reassembly. Sealing was designed without packing on the register faces between bowl and cone, since results from previous rigs suggested that the pressure differential across the joint would be small.

The tappings were constructed as for the planar stepped model, using hard bronze clock bearings. Advantage was taken of the greater surface area of the axisymmetric model to reduce the streamwise increment to 2° over the Coanda surface and then every 3mm on the flat surface. The tappings were spread over a 120° spanwise sector so that the flow could be visualised over both the tappings and the plain surface, in order to establish how far the tappings affected the flowfield. Semi-rigid polyethylene tubing was attached to the rear of the tappings as before, with hypodermic pipe and cyanoacrylate adhesive, and then threaded through the step orifice in the bowl. The tulip cone was screwed onto the bowl and the tubes then pulled through to free the bowl for insertion of the shaft. In this way, twisting of the tapping tubes during assembly was avoided. The tubes from the step tappings were fed through the tulip and the slack taken up as it was slid onto the shaft.

The lip tube axial movement, by means of a small-pitch thread, was to provide relatively fine adjustment and sufficient leverage to overcome the resistance of the O-ring, although this was reduced by assembly with rubber lubricant. It also permitted the use of a locknut to prevent drifting during running. A three-point static pressure tapping was provided to reduce the effects of the wake from the four-legged spider.

Support work was required to protect the optical rig from impingement of the broken away jet and to provide partial attenuation of the rig noise. It was also used to clamp the top end of the model shaft to prevent flow-driven oscillation, to take some of the pressure load on the nozzle, and to permit some

minor adjustment of the nozzle exit concentricity. A tubular steel frame was designed to provide the main strength and plywood sidewalls were added for shielding at a relatively low cost. By enclosing the axisymmetric model, the future addition of a relatively inexpensive metering system for the entrained air was made possible. In the finished assembly, the sound-proofing material which had been considered was not found necessary.

The shielding structure is shown in figure 5.5. Plate glass windows were provided to allow optical access to the model, and these were checked for adequate strength under jet impingement, using data from Shand¹⁹⁸⁴. Since the application of interferometry to this model was not envisaged, the lower optical quality of the plate glass was tolerable. If required, however, interferometry could be performed with these windows removed, provided care was taken not to break the jet away.

5.5.3 AIR SUPPLY MODIFICATIONS

Owing to the greater breakaway pressures expected and the larger slot area of the axisymmetric configuration, modifications of the air supply line were required. The existing microporous filter had insufficient capacity for the airflow required and so was replaced (in fact, it was changed when the stepped planar model was introduced, since the original was at its maximum specification, resulting in unacceptably short service intervals). Furthermore, the microfibre filter was removed to provide additional flow capacity, and, since the airstream was no longer in direct contact with precision optical components, the reduction in filtration quality could be tolerated.

A calculation of the flow characteristics of the supply system revealed that the original pressure regulator with internal referencing would restrict performance below the flowrate required to break away the axisymmetric jet. Although runs with the pressure reference point shifted downstream of the filters were tried, these attempts failed to modify the reduced pressure versus mass flow characteristic sufficiently to isolate post-regulator pressure from the effects of large decreases of the receiver pressure in blowdown mode.

The regulator was therefore replaced and, because the original regulator had the safety valve built in, an additional blow-off valve and pipe connections had to be provided. Even with the new regulator, a remote pressure reference downstream of the transition to post-regulator pipe diameter was still required to achieve breakaway pressure at the axisymmetric model. This configuration was found to be prone to oscillatory behaviour, so a microbore pilot tube ($\text{\O}2\text{ mm}$) was used in place of a conventional tube to introduce feedback damping. This required additional filtration at both ends of the pilot to prevent clogging, since both the regulator and the reference point were upstream of the main filters.

A change in the pipework of the supply system immediately adjacent to the model was also required. This was accomplished by replacing the riser tube, the baseplate of the suspension system and the riser transition piece with components appropriate to the axisymmetric geometry. The greater part of the existing pipework was retained through these modifications, since care was taken to choose replacement components either with the same port sizes

or with ports which could be accommodated by rearrangement of existing pipe sections. A schematic of the changed layout is presented in figure 5.6.

6 EXPERIMENTAL TECHNIQUES

6.1 INTERFEROMETRY

6.1.1 PLANAR BUILD GENERAL OPTICAL ALIGNMENT PROCEDURE

A schematic of the optical apparatus developed by Gilchrist¹⁹⁸⁵ is given in figure 6.1. The same equipment was used and the following alignment procedure was adapted from that used by Gilchrist:

- (a) The optical benches were assembled as shown in the schematic diagram and the angles checked with a large try-square. The height settings of the feet were adjusted, using a spirit level to check that the benches were level both parallel and perpendicular to their central axes. The arrangement of the anti-vibration supports was calculated to give approximately equal loading on the feet with the optical rig level.
- (b) The spatial filter was attached to the laser. With the secondary lens removed, the position of the primary lens was adjusted until the beam produced a circular image through the pinhole onto a black card. The position of the pinhole was altered slightly and the adjustment of the

primary lens repeated until maximum apparent intensity of the card image was achieved. The secondary lens was reattached to the spatial filter and the beam checked for parallelism. The filter was removed to check that it did not cause deviation of the beam (which would indicate misalignment) and then replaced.

- (c) A concentric target was attached to one of the parabolic mirrors. The beam direction was adjusted until a traverse of the mirror along the central bench showed it to be level at the centre height of the mirror and parallel with the centre line of the bench.
- (d) The three lenses were placed in turn in the beam and adjusted until no deviation of the beam at the mirror target was registered.
- (e) Both beam splitters were placed on the central bench very close to their final position. The laser was then offset slightly from the bench centre line so that the transmitted beam from the second beam splitter emerged along the bench centre line. This was necessary because the beam was refracted by passing through the thick beam splitter substrates. Had no correction had been applied, the reference beam and working beam could not have been made collinear on the optical bench centreline after recombination.
- (f) The mirror M1 (and target) was placed in position. The position and angle of splitter B1 were then adjusted without a lens present to ensure that the beam struck the centre of M1. Lens L1 was introduced between M1 and B1 and traversed along the second bench to establish the direction of the beam with respect to the bench centre line. The

adjustment of B1 was repeated until the angle between the beam and the bench centre line was less than 0.1° .

- (g) The second mirror M2 was placed in position, and the target transferred to it from M1. Rotation of M1 was used to centre the beam on M2. Lens L1 was replaced and traversed to a position giving a parallel beam between the two mirrors. The target was then placed in a separate holder and adjusted simultaneously with M2 until the beam was travelling along the centre line of the last optical bench. Traversing of lens L2 was used in a similar manner to step (f) to confirm the direction. L2 was then traversed to a position in which the beam emerging from it was parallel.
- (h) The position and angle of splitter B2 were adjusted until the reflected working beam and the transmitted reference beam were collinear. This was checked by using the target and holder set up in step (g).
- (i) The mechanical rig was now placed in position and the windows installed. Using a target affixed to the front window, the rig was centred on the beam by adjusting the vertical and horizontal supports. Lens L1 was then removed (after its position was noted) and the torsional support adjusted with the rig pressurised but at zero flow until the back-reflection of the beam from the front window was centred on mirror M1. L1 was then replaced at its previous position. Working beam collimation was confirmed by a target at the windows.
- (j) Lens L3 was added at the end of the optical train to produce a focussed image of the working section.

All the above adjustments were made without the use of micromanipulators and were therefore time-consuming, but the equipment was consequently much less expensive. Checking the alignment at the end of the planar rig test program revealed no significant alteration.

6.1.2 IMAGE ADJUSTMENT AND PHOTOGRAPHY

The final adjustment of the planar build optical rig for interferometry proceeded from the general alignment procedure as follows:

- (a) Mirror M2 was rotated from the central position until vertical fringes appeared on the image projected onto a white board. The position of lens L2 was adjusted to ensure that these fringes were linear when checked with a straight edge. Further rotation of M2 was then used to generate fringes at about 0.75 mm spacing when scaled to the actual size of the working section.
- (b) A Contax 159MM single lens reflex camera was selected for photography on account of its 330 ms vertical travel blade shutter. A 50 mm focal length objective lens and bellows were added for image magnification. Ray-tracing techniques were used to calculate the position of this assembly for maximum depth of field (to minimise shadowgraph effects). A dark filter was placed over the camera eyepiece to permit visual inspection of the laser image through the objective lens and then lens L3 was set to focus the working section image on the film plane.
- (c) The mechanical rig was set to flow conditions and the reference beam blocked off. Small adjustments were then made to the position of lens

L3 and the camera assembly to find the actual minimum shadowgraph setting. This completed the alignment procedure.

The recording of the interference pattern for the no-flow condition took place immediately prior to the flow test, with the rig unpressurised. The photographs were produced on Ilford XP1 800 ASA film with the objective lens at f1.4 and the shutter at $1/2000^{\text{th}}$ s exposure time. This rated the film at 1600 ASA (underexposure), which was compensated for by extra development. XP1 film is particularly suitable for this treatment since it is a dye film in which the resolution of the final negative is almost unaffected by development time. Furthermore, it has a very wide exposure latitude which partially compensated for the intensity variation across the laser beam. The laboratory containing the apparatus was blacked out during the photography to prevent ambient light degrading the image.

6.1.3 OPTICAL CLEANING PROCEDURE

The operation of the filtration system of the air supply failed to provide a completely contaminant-free airstream. In practice, it was found that soiling of the working section windows sufficient to degrade the image occurred after three hours' running. Condensation of vaporised compressor oil and graphite drawing lubricant from the high pressure main appeared to be the main causes of the contamination. The cleaning procedure, adapted from that recommended by Oriel¹⁹⁸⁰, was as follows:

- (a) The windows were removed from the rig and placed on a pad of ordinary tissue paper covered by a sheet of lens tissue. Loose material was removed by the use of an inert gas jet sprayed parallel to the window surface.
- (b) A sheet of lens tissue was placed on the soiled surface and dampened by droplets of microfiltered pure methanol (without drying agents). Just enough methanol was used to completely wet the window surface.
- (c) The sheet of lens tissue was slid over the surface of the window by pulling on the edge. This created a dry area on the component which grew until the entire surface was dry, whereupon the lens tissue was lifted from the window. The direction of pull was set to move contamination away from areas of the window adjacent to the airstream. It was found that two repetitions of the process were required to remove the contamination.

The whole cleaning and handling procedure was carried out using polyethylene gloves to avoid adding further contaminants.

6.1.4 INTERFEROGRAM PROCESSING

The negatives of the interferogram images were printed onto monochrome gloss finish photographic paper at approximately seven times life size. The fringes were numbered manually. On the flow test image this was achieved by following one fringe from the undisturbed region into the flowfield. The other fringes could then be numbered relative to the first identified fringe. The same procedure was used to maintain the numbering sequence through other areas of rapid variation in the flow. The accuracy of this technique was checked by comparing the shift between a fringe in the nozzle entry region and its

undisturbed portion with the shift expected from the riser tube static pressure and the atmospheric pressure.

The numbered fringes and the flare model edges were then manually digitised, using a Summagraphics TD-1-CTR-3648 tablet attached to a Whitechapel MG1 workstation controlled by University of Durham Computer Centre software. The tables of coordinates produced were then transferred to an Amdahl 5860 mainframe using KERMIT communications software for processing. This produced two files, flow and no-flow, for each flowfield condition, at a rate of one image to four hours' digitisation.

Geometrical fitting of the flare model outline to the digitised image was performed using the E04NAF least squares routine from the NAG Library¹⁹⁸⁸. The information from this fitting routine was then used to transform and reduce the raw data. A plot of the transformed points at input image size was used to check the digitisation. Fringe points which could be visually perceived to be in error were removed from the data file using an editor. The resulting files were then copied to backing store for possible future use.

Using this data, the interpretation proceeded by calculating the fringe shifts along fringe lines, and then calculating the corresponding density values from the formula:

$$\rho'(x, y) = \rho_{ref} + (\lambda_{HeNe} / K_{gd} \delta z_{ws}) S'(x, y)$$

The density field $\rho(x, y)$ was then interpolated with a fourth-power distance weighting routine from the discrete values $\rho'(x, y)$. The routine supplemented

the weighting with direct assignment if a discrete density value lay within a small capture radius of a field grid point. Additional discrete values of density had to be added to the data set at points within the Coanda surface, in order to prevent distortion of the interpolated regular grid values. The resulting grid values were transferred to backing store for use as input for the presentation program. Discrete pressure and Mach number fields were derived before the density interpolation, by assuming constant stagnation pressure in the jet core and linear variation in the outer mixing layer. These discrete values were then interpolated with the same algorithm used for the density. The assumptions for stagnation pressure were crude, but gave substantially correct values for the surface pressure when compared with experiment.

6.2 SCHLIEREN VISUALISATION

6.2.1 AXISYMMETRIC BUILD GENERAL OPTICAL ALIGNMENT PROCEDURE

The components used for the planar build optical rig were also used in the axisymmetric build. The procedure used to align the configuration (shown in figure 6.2) was as follows:

- (a) Before demounting the planar build, all components were returned to the fully aligned position of the general procedure. The components were then released from the traverse tracks of the optical benches.
- (b) The optical benches were re-assembled as shown in the schematic diagram and the angles were checked with a large try-square. The height settings

- of the feet were adjusted until all the benches were level when checked with a spirit level both parallel and perpendicular to the central axis.
- (c) The spark source was mounted on a pedestal and set to give a $0.125 \mu\text{J}$ spark at 100 Hz. The primary lens was used to focus the beam for minimum spread and the direction of the beam was adjusted until centred to the optical bench and level at the mirror centre height. This was checked by attaching a target to the mirror M1 and traversing it along the bench, as in step (c) of the planar build. The mounting of the source was adjusted to give a vertical spark image and the beam centre was taken as the centre of this image.
- (d) Mirror M1 was then traversed to its final position and lens L1 interposed between it and the spark source. The relative positions of the source, the primary lens and L1 were adjusted to give a minimum sized image of the spark. The combination was then traversed to place the spark image at the focus of M1, thus producing a parallel reflected beam.
- (e) M1 was rotated until the beam was centred on mirror M2, which was placed on the other bench. The angle of the mechanical rig windows was adjusted with a protractor until these were normal to the line between the mirror centres.
- (f) Lens L2 was introduced onto the second bench and traversed until the emerging beam was parallel. This was checked by traversing a target in the knife-edge holder. Since no plane mirror was available, beam splitter B2 was placed on the central bench and its traverse and angle adjusted until the reflected beam was central to the bench.

(g) Lens L3 was added at the end of the optical train to produce a focussed image of the working section.

The optical rig was built with the mechanical rig in place, since the close juxtaposition of the two rigs in the operating configuration would have exposed the optical rig to a risk of damage, had it been assembled first. The laser could not be used for alignment purposes, since part of the mechanical rig support work would have interfered with the beam path and the position of the first beam splitter. Therefore, the axisymmetric build was not subject to the high quality alignment of the planar build. Since interferometry was the only technique used for which high accuracy was essential, the reduction in alignment quality was tolerated. By omitting the laser, some compensation could be gained by positioning the working beam much closer to the true offset axis of the parabolic mirrors.

6.2.2 OPTICAL RIG CONVERSION

In order to use the optical rig for schlieren, the following steps were taken:

(a)(For conversion from the planar build)

The camera and bellows were left in place and the interferometer was returned to the infinite fringe mode by rotation of mirror M2. The spark source was interposed between splitter B1 and lens L1, and the positions of the source and L1 were adjusted as for step (d) of the axisymmetric build procedure to give a parallel expanded beam through the working section.

(For conversion from the axisymmetric build)

After the general procedure, the camera and bellows assembly described in section 6.1.2 above was added to the end of the optical train.

- (b) The knife-edge holder was introduced between M2 and L2. A target was placed in the holder, which was then traversed to the focus point by noting the size of the spark image on the target (smallest at the focus). Finally, the target was replaced by a vertical knife-edge.
- (c) For horizontal knife edge schlieren, the spark source was remounted at 90° to the original position without disturbing any other components. The direction was then checked with a target at M1 to ensure that the carrier for the spark source had not been shifted. A horizontal knife edge was then substituted for the vertical one.

6.2.3 IMAGE ADJUSTMENT AND PHOTOGRAPHY

Once the optical rig had been prepared for schlieren, the knife edge was removed and the mechanical rig set to flow conditions. The position of lens L3 was adjusted until the minimum possible shadowgraph effect was obtained. The knife edge was then replaced in the appropriate orientation and the cut-off adjusted until maximum tonal range in the image was achieved.

Continuous schlieren photographs were taken on Ilford FP4 125ASA monochrome film with the objective lens at full aperture and the shutter on automatic. The spark was set at 1.25 μ J and 80 Hz, which gave an exposure time of approximately 1/4 s. The film was developed as recommended by the manufacturer and printing was arranged so as to avoid increased contrast.

For spark schlieren, the shutter speed was changed to a fixed $1/2$ s setting. The spark source was then set to give a $12.5\ \mu\text{J}$, $6.5\ \mu\text{s}$ spark at a frequency of 2 Hz so that the image would be formed by a single spark. No synchronisation was used, but three exposures taken at each flow setting ensured the capture of at least one image. This technique was chosen to avoid the cost of synchronisation circuitry. All the schlieren photography was performed with the background lighting extinguished.

6.3 SHADOWGRAPH VISUALISATION

6.3.1 FLARE MODEL TESTS

In order to perform shadowgraph visualisation, the optical rig was first adjusted for horizontal knife edge schlieren, but without the knife edge. The mechanical rig was then set to flow conditions and the image of the working section defocussed using lens L3 until a satisfactory shadowgraph was obtained at the film plane.

This image was recorded on Ilford FP4 125 ASA monochrome film with the objective lens at full aperture (f1.4). The automatic shutter gave an exposure time of approximately $1/8^{\text{th}}$ s and the film was developed as recommended. For flow conditions with very weak wave processes some contrast enhancement was used in the printing of the negatives.

6.3.2 FULL SCALE FIELD TESTS

Shadowgraph visualisation was also performed on an operational IS flare

at British Petroleum's Easington test site. The method used, along with the apparatus, is described in section 5.3.

6.4 SURFACE FILM VISUALISATION

6.4.1 OPTICAL SYSTEM AND PHOTOGRAPHY

A schematic diagram of the optical system for surface flow visualisation is presented as figure 6.3. The media used were based on three components:

A – 200/12,500 cS Dow-Corning Silicone Fluid;

B – 200/1000 cS Dow-Corning Silicone Fluid;

and C – 'Dayglo' fluorescent dye powder (orange emission under ultra-violet radiation).

A high viscosity compound was prepared in the proportions (by weight) of three parts A to one part B to one part C. Proportions of one part A to three parts B to one part C were used for a medium viscosity fluid.

The directional light sources used were a 100 W ultra-violet emitting lamp and a 60 W tungsten filament lamp. Ambient lighting was provided by four 80 W fluorescent tubes. The UV lamp was placed approximately 200 mm away from the Coanda surface, this being a compromise between getting the maximum energy into the dye and avoiding damage to the light source from the airstream. It was not possible to use the perspex windows as a shield for the lamp, since they were opaque to UV radiation. A plane mirror behind the lamp was used to increase the radiation flux into the dye. The 60 W tungsten source was used to relieve the shadow on the underside of the model surface cast by the ambient lighting. The tungsten source was placed behind

the perspex window, and it was found necessary to interpose a tracing paper diffusor between the two to reduce direct reflections from the surface.

In order to avoid damage to the camera and to get an acceptable viewpoint around the illumination equipment, a plane mirror was placed so as to bring out the surface image on an axis below the side windows and normal to them, as shown in figure 6.3. Three stages of optical filtration were used: firstly an ultra-violet excluding filter was added to the objective lens to eliminate direct and reflected radiation from the UV source. Secondly, this was supplemented by an 80B colour correction filter for the preferential transmission of orange to enhance the contrast between the dye and the rest of the image. Thirdly, the filter stack was completed by a linear polarising element which was adjusted until all direct reflections from the visible light sources were eliminated.

The film, Ilford FP4 125 ASA monochrome, was chosen for its definition, but the heavy filtration required the use of an aperture of f2.8 on the objective lens to give an automatic shutter speed of about $\frac{1}{4}$ s. This resulted in a short depth of field and so the surface patterns had to be photographed from two different viewpoints. The complete surface pattern could not therefore be recorded simultaneously. Some benefit, however, was gained by this, since no compromise had to be made between the viewpoints of the upper and lower parts of the surface. The upper surface view was set normal to the flat surface at the end of the curved Coanda section, whilst the lower viewpoint was set along the radius 45° from the slot around the curved surface (see figure 6.3).

For recording of the surface flow pattern on the side walls, the tungsten illumination described above was removed. The tracing paper diffusor on the back of the rear window was replaced by a matt black screen. The ambient light was found to provide enough contrast for photography, provided the camera settings used for the Coanda surface views were retained. The viewpoint was normal to the side windows, with the frame centre aligned to the 'maximum radius' point of the Coanda surface. Only one side wall was coated with visualisation compound to maintain clarity in the image.

The dye compounds were applied to the Coanda surface by brush and painted very thinly to minimise the disturbance to the flowfield. A period of time was allowed for any brush strokes in the coating to disappear before starting a run. The choice of high or medium viscosity fluid for any particular part of the model was dictated by the rate of fluid stripping from the surface at the flow condition required, and mixtures of the two were used for intermediate areas. Some contamination of the general environment by dye mixture stripped by the airstream was found unavoidable and steps had to be taken to ensure that this did not cause damage to any other equipment. In particular, the mixture was thoroughly cleaned from the windows at the end of each series of runs to avoid the stress cracking which can result from the chemical action of oils on perspex.

The position of surface patterns was established by reference to the tapping holes, which were clearly visible on the photographs. Careful note

was also taken whilst running the tests to confirm the pattern positions and to establish the direction of fluid flow on the surface.

6.4.2 FULL SCALE FIELD TESTS

Surface flow visualisation was also performed on a full-scale I8 flare at British Petroleum's Easington Test Site. For this duty, natural daylight was regarded as the only feasible illumination. The high viscosity fluid mentioned in the last section was tested in this application, since it is bright pink in daylight. Finely divided aluminium powder mixed with bearing grease was also tried in place of the dye mixture but gave poor photographic results. However, the most successful mixture used in the tests consisted of white titanium dioxide pigment with silicone fluids A and B (as specified above) in the proportions 1:9:3 respectively by weight. The patterns were photographed on high resolution Ilford Pan-F 50 ASA monochrome film to take advantage of the strong daylight illumination available.

Since no tappings were present in the full-scale flare, markings had to be added to the flare surface to identify the positions of the surface patterns. Insulating tape with rulings drawn in ink proved adequate and inexpensive, although the strips used were rapidly destroyed by the gas stream forces and had to be replaced at frequent intervals.

6.5 SURFACE PRESSURE MEASUREMENT

The measurement of the pressure at the surface of the model was performed using two multimanometer banks with a total of 60 tubes. Mercury was used as the manometer fluid, primarily to provide the required pressure range of approximately 0.1 to 1.2 atmospheres. Higher pressures were experienced as a result of shock wave impingement at the surface. Since such peaks were generally localised to a single point, tappings were sealed off as necessary to prevent manometer blow-out.

A useful consequence of using mercury was the damping out of high frequency pressure fluctuations, thus permitting easy reading of the mean value. However, manual notation of the readings would have been taken too long to avoid errors from low frequency fluctuations and drift of the rig setting. It was therefore decided to photograph the multimanometers, which also permitted synchronisation with flowfield visualisation and hence enabled direct comparison of results.

The photographic set-up is presented in figure 6.4. The manometer tubes were placed at a 45° angle to the photographic axis completely filling a 35 mm frame to ensure that reflections from the glass fronts of the manometer banks were not picked up on the image. This required the use of an f11 aperture on the 50mm objective lens of a Canon AE1 single lens reflex camera to provide sufficient depth-of-field to focus on all the tubes simultaneously. A Vivitar 286 flashgun was needed to provide enough illumination to expose the Ilford FP4 125 ASA monochrome film chosen for its resolution. The use of flash

illumination in conjunction with mercury proved particularly good for contrast with the manometer background and scales.

The flowfield visualisation and manometer cameras were set off in sequence by remote shutter release to achieve the closest possible synchronisation without interfering with the flowfield photography. The tappings were connected in angular sequence to the manometer banks so that the shape of the columns gave an instant visual indication of the pressure distribution. Actual readings were taken by using the scales visible on the manometers when the developed negatives were projected onto a screen at 1.5 times the size of the tube banks. Parallax and other reading errors were estimated at 0.5% of atmospheric pressure.

6.6 MECHANICAL RIG OPERATION

6.6.1 CLEANING AND ASSEMBLY

As mentioned in section 6.1.3 above, problems were experienced with the filtration system's failure to remove all contaminants from the airstream. One suspected cause of this was the passing of vaporised compressor oil through the mechanical filters, since a strong smell of oil was noticeable during running. The addition of an activated carbon filter, as supplied for breathing apparatus, would have been uneconomic for the large air flow rates required. Furthermore, the final filter in the system consisted of a microfibre element, which used collision and static charge effects to remove small particles. Since some of the contamination arose from the graphite used for drawing the seamless pipes of

the high-pressure main, the efficiency of the capture process may have been affected by the conductivity of the graphite particles.

Close examination of the supply system pipework downstream of the filters revealed considerable deposits of corrosion and soiling and so it was decided to dismantle and clean them. A rotary wire brush attached to an electric drive via a flexible shaft was used on the steel piping, followed by pulling through with foam rubber pigs soaked in alcohol. The flexible rubber pipe was washed with a water and detergent mix, then rinsed in water and allowed to dry, and finally an alcohol pig was used to remove the last traces of moisture.

On reassembly, care was taken to use jointing methods which would not affect the airstream. The flexible pipe was joined to the metal fittings by rubber adhesive, and then jubilee clips were fastened over the top to resist the forces on pressurisation. This assembly was allowed to ventilate for several days to ensure that any traces of solvent from the adhesive had dispersed. The many screwed pipe joints were sealed by a two part technique; with PTFE tape on the inner part of the thread (nearest to the flow) and with jointing compound on the outer part. Again, a considerable ventilation period was allowed. Final assembly was made at the flanged joints, which were sealed with conventional fibre or rubber gaskets.

6.6.2 PROCESSING OF INSTRUMENTATION OUTPUT

Mechanical rig leakage estimations were performed in order to correct the

flowmeter readings at flow settings. Static tests were performed by pressurising the supply pipework with the flare model replaced by a blanking flange. The pipework was then isolated from the high pressure main and the rate of pressure loss noted. Leakage rates at different pressures could be calculated from the estimated volume of the system. The test was repeated with the flow control valve closed to give two correlations of leakage (upstream and downstream of the control valve), since, in the majority of tests, the pressures in the two parts of the system were significantly different.

However, there were several sources of possible inaccuracy with this method. Firstly, there would have been some leakage through the isolating valve between the high pressure main and the supply pipework, which would lead to an underestimation of leakage. Secondly, only leakage after the flowmeter was needed for correction, whereas the above test included all pipework up to the high pressure main, thus overestimating leakage. Since the test rates were small (typically 1-2% of the rig flow) and the use of a soap-bubble test mixture on the joints revealed leaks consistent with those calculated, the above problems were judged to be partially counter-balancing.

Leakage around the seals of the flare models could not be estimated. In the case of the planar model in particular, this was expected to be significant at small slot heights. In order to calibrate the flowmeter, it would have been preferable to use a direct method, such as water displacement. However, at typical airflow rates (in the region of 0.25 kg/s), this would have required an impractically large tank for reasonable measuring times. No other

reference device with a large enough capacity was available and so error and flowrate estimation in accordance with B.S.1042 for the flowmeter had to be accepted. Accordingly a systematic bias towards overstatement of rig flowrate was expected.

The pressure gauges and transducers could be removed from the rig and compared to a dead weight tester. In all cases this revealed highly linear curves, although some of the gauges had significant offsets. The errors from the gauges were used to produce an error analysis, which was combined with that for the flowmeter to give some idea of the inaccuracy of stagnation pressure ratio calculation at each rig setting. The error analysis and the calculation itself were implemented in the same computer program to speed the processing of experimental results and to avoid the inevitable mistakes of repeated manual evaluation. It was found that maximum errors were of the order of a few percent in the cases tested.

6.6.3 BREAKAWAY TEST PROCEDURE

The identification of the points of breakaway and reversion was expected to require some care, since these are both features of a flow instability and as such are likely to be heavily influenced by transient flow disturbances. Accordingly, the general regions of these phenomena were identified for a particular geometry with fairly fast operation of the flow control valve and an accurate estimate found by very slow variation when approaching the transition point.

Tests were made to establish the repeatability of the results. Small disturbances such as mechanical vibration and interference with the flowfield were also introduced to reveal any sensitivity. The partial reversion phenomenon described later was found particularly difficult to identify, but other phenomena were quite 'well-behaved' when these disturbances were applied.

7 PLANAR COANDA RESULTS

7.1 EXPERIMENTAL WORK

7.1.1 FLOWFIELD MEASUREMENTS

7.1.1.1 Breakaway and Reversion Tests

The stepped model was tested for breakaway and reversion over the full range of slot/step combinations. Slots ranged from 2.00 to 8.00 mm in 2.00 mm increments and steps from 0.00 mm to the maximum setting which resulted in an initially attached jet. The results (shown as figures 7.1.1 to 7.1.4) showed the same pattern as those obtained by Gilchrist¹⁹⁸⁵ in the unstepped case, namely, that breakaway pressure ratio rises with increasing radius/slot ratio. The breakaway pressures for the stepped rig at zero step were slightly higher than Gilchrist's, as would be expected, since the discontinuity at the step plate - Coanda surface joint is likely to have caused transition (or at least additional turbulence) of the boundary layer. This would have increased its separation resistance, since the detachment takes place as a secondary effect in the favourable pressure gradient zone. A further consequence is that the the

entrainment characteristics of the free shear layers in the recirculation zones should have been similarly enhanced, thereby promoting stronger reattachment through the Chilowsky effect.

For the stepped model, the effect of the slot followed the same general trend, but the dependence on radius/slot ratio was stronger as the step increased. As for the effect of varying the step at a given slot height, it can be seen from the curves that the breakaway pressure increases with step size. It is more convenient to discuss the reasons for the enhanced performance below, where the results of flowfield visualisation are presented. It should be noted that the increased breakaway performance with the step parallels that experienced in operational *axisymmetric* flares and so tends to confirm the value of planar work for use in studying the axisymmetric problem.

The reversion characteristics of the device responded more strongly to the presence of the step, with much more improvement than for breakaway. Flow visualisation results showed that the step recirculation zone was maintained, regardless of the downstream behaviour of the jet, and it appears that this provided initial bulk turning of the flow towards the vertical and a recirculation shear layer (almost certainly turbulent) which scaled with the step size. Both of these features tend to aid a Chilowsky entrainment effect at the Coanda surface, overwhelming separation and accomplishing reversion. Moreover, the tests on stepped flares at 4.00 mm and 6.00 mm slots revealed a third type of behaviour, partial reversion, in which the broken away jet was deflected back towards the Coanda surface, but with the final jet direction at approximately

45° to the vertical. Comparison of the full and partial reversion curves in figure 7.1.3 shows that the latter varied smoothly with step height, suggesting pure Chilowsky effect reattachment, whilst the former, with a more complex shape, suggests that differential scaling of the wave systems was involved. The absence of such a phenomenon for the 2.00 mm slot in figure 7.1.4, and the smooth reattachment curve imply that the Chilowsky effect was dominant where the jet cell structure was small and much reduced by viscous effects on the later part of the Coanda surface. At zero step, it appears that the weaker cell structure failed to interfere with the Chilowsky effect enough to prevent full reversion. For the 8.00 mm slot in figure 7.1.4, since the reversion curve retains the complex form, the reverse appears to be true and this gave rise to a *falling* trend.

7.1.1.2 Interferometry

The finite fringe interferometry revealed several features of use in understanding the near nozzle region of the unstepped flare. Plate 2b shows the fringe pattern obtained with a slot of 4.00 mm and a blowing pressure just sufficient to choke the nozzle ($C_{po} \equiv p_a/p_* = 0.488$). It is apparent that the growth of the turbulent outer shear layer quickly obscured the fringe detail as the jet proceeded downstream, and this rendered digitisation of the interferogram possible only in the region from the nozzle entry to about 30° round the Coanda surface from the nozzle exit. The fringe pattern after digitisation is plotted as figure 7.1.5. This was analysed by comparison with the analogous pattern derived from plate 2a to produce the property fields of figures 7.1.6

to 7.1.8. The Mach number contour plot reveals that the nozzle sonic line lay a significant distance before the exit on the lip side and confirms that the disturbances noticed after this point in the flow visualisation photographs can be explained by supersonic stream/boundary layer interaction. The pressure contour plot also shows how the pressure influence of the surroundings penetrated upstream of the exit. On the nozzle surfaces, strong favourable pressure gradients are shown, in accordance with the strong acceleration associated with contraction in a subsonic flow. This favourable gradient continued on the Coanda surface under the influence of the weak expansion wave from the lip edge and post sonic line boundary contour. This was followed by a recompression as a result of the reflection of the wave from the jet outer edge. Thereafter the compression wave system, weakened by expansion caused by boundary curvature and diffusion in the outer shear layer, was effectively damped out. Weak expansion waves, emanating from the Coanda surface, continued to accelerate the jet as the last vestiges of the wave system caused very slight oscillations in the otherwise practically constant surface pressure distribution.

As the blowing pressure was increased to give a C_{p0} of 0.303, the fringe pattern developed to that of plate 5a. This time, bending of the working beam by the compression wave caused a shadowgraph which obscured the fringe pattern. Despite considerable efforts this effect could not be eliminated and grew worse with stronger compression waves so that the technique became unusable for the jet close to breakaway. The net effect for the example mentioned above was to make it impossible to assign fringe number downstream

of the obscuration, which again limited the zone available for analysis to the first 30° from the nozzle exit (figures 7.1.10 to 7.1.11). The sonic line again lay inside the lip and in almost the same place as before, suggesting it could be regarded as invariant with pressure for this slot height. The favourable pressure gradient on the nozzle upper surface which continued onto the Coanda surface under the influence of the lip expansion was interrupted by a separation bubble and its associated sharp compression wave. The pressure in the bubble is revealed to have been substantially constant, once the immediate region of detachment is passed, as would be expected for a slow speed recirculation zone of sufficient size.

Plate 5b shows that the obscuration problem became much worse still in the reduced cell scale of the stepped jet, and for such cases the considerable effort required to process the interferograms was regarded as not worthwhile for the very limited amount of information which could be derived.

7.1.1.3 Surface Pressure Measurement

The interpretation of surface pressure measurement aids considerably the understanding of boundary layer behaviour, since separation effects can be detected where these are too small to be observed in flowfield visualisation photographs. Furthermore, the disturbance of the flow field introduced by surface oil visualisation is avoided, which is important for regions of very thin separation.

Considering first the unstepped flare model configuration, figures 7.1.12, 7.1.16, 7.1.23 and 7.1.27 show the same basic pattern as the pressure ratio decreases (increased blowing pressure). Figure 7.1.12a gives the clearest demonstration of the pattern, since the wave structure scaled with the slot height so that a 2.00 mm slot gave more waves on the Coanda surface. At $C_{po} = 0.331$, the wave pressure structure was smooth and regular, implying that the boundary layer only affected the flow minimally and that therefore the jet was fully attached. However, there was a slight irregularity at the first pressure trough, indicating incipient or very thin separation. As the blowing pressure increased, evidence of separation at the first two troughs became clear; roughly constant pressure zones indicating substantial separation which extended upstream into regions that should have been *favourable* pressure gradient zones (as found by Gilchrist¹⁹⁸⁵). The figure also demonstrates the lengthening of the shock cell structure with decreasing pressure ratio. Regions of strong favourable pressure gradient appeared after each separation and the consequent presumption of reattachment is well supported by the surface oil flow results. However, reattachment was not solely due to favourable pressure gradients, since the sub-atmospheric bubble pressure should also have caused gross jet bending towards the surface and the rapid growth of the shear layer entrainment at the bubble edge will also have caused enhanced recirculation, hence lowering the bubble pressure and further attracting the flow towards the surface. The next plot in the series shows that the separations at the troughs of the first two waves amalgamated and that the jet impingement onto the surface at reattachment became very weak, as revealed by the small pressure

rise on the third peak. In the final plot, the jet was broken away, as the initial failure to reattach allowed fluid at atmospheric pressure to be drawn into the bubble, which, in turn, caused the jet to 'flip' further away from the surface.

The same behaviour is evident from figure 7.1.16 for a 4.00 mm slot, and the trend continues in figure 7.1.23 with the 6.00 mm slot, but here the third 'recovery' wave peak had moved off the end of the Coanda surface (and was practically dissipated by viscous action). Consequently, breakaway occurred at the disappearance of the recovery peak *between* the first two pressure troughs. This was repeated for the 8.00 mm slot in figure 7.1.27 and explains why the breakaway ratio for the larger slots was weaker than that for the smaller ones.

In the case of the 2.00/0.75 mm slot/step configuration shown in figure 7.1.13, the basic pattern of lip waves was complicated by waves generated at the step expansion and by the reattachment shock after the step recirculation zone. The interference of these waves damped down the pressure oscillations, since the cell structure approached that of a free jet more closely, and thus the scaling of the cells was reduced (a free planar jet is half the scale of the equivalent flat wall jet). Owing to the wave interference, the pressure peaks were smaller, making the adverse pressure gradients weaker. Furthermore, the step zone pushed the first separation further round the Coanda surface. Apart from these changes, the general behaviour of the surface pressure distributions

for this configuration was altered only by the blowing pressure at which significant changes occurred. Most noteworthy is the fact that the cell structure again practically disappeared as breakaway was approached.

As the step was increased further to 1.50 mm in figures 7.1.14 and 7.1.15, the interference pattern between waves appears to have widened the region over which a favourable pressure gradient occurred towards the end of the curved surface. The pressure coefficient at the step followed the same pattern as for the smaller step, *i.e.* it rose with blowing pressure. This suggests a weakening of the effect of the step towards breakaway, as the different scaling of the interfering wave systems with blowing pressure leads to destructive interference of the wave system, thereby exposing the boundary layer to a continuous adverse pressure gradient. The rise in step pressure coefficient was smaller for the larger step, which would serve to explain the increase in performance with step size.

The picture alters significantly, however, at larger slot heights; the 4.00/0.75 mm slot-step combination in figure 7.1.17 reacted much more strongly to the presence of the step. The pressure coefficient at the step was much lower, and the rest of the wave system was so altered by interference from the step expansion and reattachment shock wave systems that little similarity exists between the stepped and unstepped cases until breakaway was again approached, when the wave system in both cases disappeared. From later visualisation results it appears that in the unstepped case waves were smoothed out by large separations, whereas the stepped flow showed much less gross

separation effect, implying that wave cancellation played a more important role in this case. As the step was increased to 1.50 mm in figures 7.1.18 and 7.1.19, similar (stepped) wave patterns were maintained and the increase in performance was small compared to the 2.00 mm slot case. For the larger slot, the step zone pressure coefficient ($C_{pb} \equiv (p - p_a)/(p_* - p_a)$) rose with blowing pressure, but the effect was weakened, as before, when the step grew larger (figures 7.1.20 to 7.1.22). However, this weakening was less marked than before (when a step of 3.76 mm was used there was very little change in C_{pb} between choking conditions and breakaway, at a C_{po} of 0.203). The 'starting' step coefficient was also lower (*i.e.* more effective), which goes even further towards explaining why the step gave less benefit at this slot height.

For the 2.55 mm step of figure 7.1.20, two pressure distributions are shown at a blowing C_{po} of 0.232. The first is with the jet fully attached, and the second after reversion. The plots are identical except for the pressure towards the end of the Coanda surface, where a peak giving rise to a favourable pressure gradient was replaced by a trough, indicating that reversion to attached jet flow was not complete. Investigation of the subsequent breakaway point revealed this to be lower than the primary one, thus providing strong evidence of the importance of this pressure wave seal for breakaway resistance. The same trends were continued for steps at slots of 6.00 and 8.00 mm (figures 7.1.24 to 7.1.26 and 7.1.28 to 7.1.30, respectively), leading, in the latter case, to a slight improvement of the stepped over the unstepped case, but showing very little beneficial effect of larger steps compared to small ones. Once again, the

major feature to be noted is the disappearance of wave structure as breakaway was approached.

7.1.2 FLOWFIELD VISUALISATIONS

7.1.2.1 Interpretation of Photographs

A note of caution should be sounded concerning shock positioning and form, since, as Stricker & Kafri¹⁹⁸² point out, the sharpness of the shock image will be affected by the interaction with the end-wall boundary layers. Vest¹⁹⁷⁹ gives a first-order analysis of refraction error and shows that it can be compensated by appropriate focussing.

The rig settings for flow visualisation were selected to permit as much comparability as possible between different geometric variants without choosing levels which were inappropriate to any particular configuration (such as exceeding the breakaway point). Furthermore, for each variant it was decided that coverage of the region between choking and breakaway should be covered as evenly as possible. Inevitably, some conflict arose, and this was resolved in favour of restricting the database, in view of the large number of geometry variants and of the time restraints on producing and processing large numbers of visualisation photographs.

7.1.2.2 Unstepped Schlieren and Shadowgraphy

In order to confirm that the planar rig with the step modifications was performing similarly to the results obtained by Gilchrist¹⁹⁸⁵, a number of

tests was carried out with the step set to zero depth. Plate 1a shows the shadowgraph for a 2.00 mm slot at a C_{po} of 0.176 (shortly before breakaway). The expansion fan from the lip rebounded from the Coanda surface and then reflected as a compression wave travelling towards the surface. This resulted in gross separation, which was transmitted upstream in the boundary layer and by recirculation, causing a strong shock at separation. The reflection of the incoming compression wave at the recirculation bubble and the shock wave at the jet edge (and *vice-versa*) created a quasi-symmetric cell system, which, although clearly subject to strong dissipative effects from the shear layers on both sides of the separated jet, managed to persist until the jet reattached.

Plate 3a shows a shadowgraph for a 4.00 mm slot, this time somewhat further from breakaway at a C_{po} of 0.325. Although the separation bubble did not match the extent of that in the previous photograph, the same general wave pattern is observed, but this time the system persisted until well after the apparent reattachment point at about 35° . There also appears to be some evidence of a transonic separation much further downstream at about 80° , which gave rise to a very faint normal shock. The same geometry is shown in plate 3b, but this time a vertical knife edge spark schlieren photograph very close to breakaway ($C_{po} = 0.255$) is depicted, and it can be seen that the wave system reverted to that of plate 1a, with extensive separation and viscous dissipation shortly after reattachment. Since the results for larger slots followed roughly the same pattern, it was not thought important to show them here.

Comparison with Gilchrist's results show very little difference, apart from a slight disturbance at the start of the Coanda surface (at the step plate joint). The main potential core of the jet was practically unaltered, but the effect on the boundary layer might have been significant. Recalling from section 7.1.1.1 above that the breakaway performance of the current model at the unstepped setting was slightly higher than that of Gilchrist, the disturbance can be interpreted as a destabilising influence on the ^{turbulence of the} boundary layer, which would thereby have increased its separation resistance.

7.1.2.3 Base Step Schlieren and Shadowgraphy

Once a step is introduced into the flow at the start of the Coanda surface, major changes were observed in the jet appearance close to breakaway. Plate 1b shows the shadowgraph for a 2.00/1.50 mm slot/step configuration shortly before breakaway at a C_{po} of 0.124. The most obvious feature is that the large separation bubble characteristic of the unstepped flare model was completely eliminated. The flowfield also exhibited much greater complexity due to the influence of the strong reattachment shock and the step expansion wave (which the pressure results show to have been at least as strong as the lip expansion for all cases tested).

In order to discuss in detail the stepped planar model flowfield, a larger slot/step case (4.00/3.76 mm) has been chosen. Plate 8b shows a particularly clear vertical knife edge spark schlieren photograph of this geometry at $C_{po} = 0.191$, just before breakaway. The detailed interpretation which follows also depends in part upon comparisons with other visualisations of this geometry at

the same conditions. Starting inside the nozzle, there were small disturbances on the lip surface, most probably due to small separations of the boundary layer. Since these disturbances failed to propagate (in the visualisation) through the expansion fans, their general effect on the model flowfield is thought to have been small. At the nozzle exit, the two expansion fans at lip and step are clearly visible, along with evidence for accompanying lip shocks, which, although quite weak (to judge by their interaction with the reattachment shock), nevertheless penetrated a considerable distance downstream into the jet core. Both the inner and outer shear layers thickened rapidly. At the reattachment point of the inner shear layer, a turning shock was produced in the jet core, and this exhibited noticeable curvature as it travelled towards the jet edge and interacted with the incoming expansion from the lip and the compression wave resulting from the reflection of the step expansion at the outer jet edge.

There was also an apparent penetration of the inner shear layer disturbance into the jet core after reattachment. However, this section of the flow was primarily under the influence of the stabilising expansion wave from the lip and the visible effect is quite faint, hence a much more likely explanation of this feature is that a 3D interaction with the side wall boundary layer at the reattachment point gave rise to a significant secondary flow. This interpretation is supported by the obscuration of the reattachment point, which suggests that there were strong density gradients normal to the plane of viewing.

Moving downstream, the next significant features were a separation shock at the Coanda surface and, almost opposite this on the outer edge of the jet, the reflection of the step reattachment shock as a strong expansion. The separation and its associated shock appear to have arisen from influence propagating upstream from the strong compression which resulted from the first reflection of the step wave. This wave was reflected again from the separation bubble as an expansion, which was made clear further downstream where it underwent a second reflection from the jet outer edge as a diffuse compression zone. The second separation bubble appears to be a direct result of this second incoming compression. Between the two separations the strong incoming expansion, resulting from the reflection of the step zone shock mentioned above, caused the jet to reattach and to generate a further outward travelling reattachment shock at the end of the first separation bubble. A considerable growth in the shear layer thickness through this interaction was noticeable.

Continuing further downstream, the second reattachment shock reflected from the jet edge as an expansion and ended the second separation bubble in a precisely analogous manner to the reattachment after the first separation. The net result was a very weak reattachment shock almost at the end of the curved Coanda surface. Two features in the flowfield have remained undescribed so far. Firstly, the lip expansion, after striking the attached boundary layer ahead of the first separation, continued as an expansion towards the outer jet edge. It reached the edge slightly ahead of the first separation shock, where it was reflected as a compression wave, which struck the boundary layer slightly

downstream of the start of the second separation bubble. Secondly, the first separation shock reflected back from the jet edge as a strong expansion, which served to restrict the width of the second separation until the continuation of the step wave described above came in to boost the bubble size. As a final point, by the end of the second separation, it appears that the combined effects of shock deceleration and shear layer growth largely eliminated the cell-like structure of the jet, which accorded well with the surface pressure distribution.

The flowfield pattern above was only demonstrated as breakaway was approached; plate 8a shows the same geometry at a C_{p0} of 0.229 (lower blowing pressure) in shadowgraph visualisation. In this case, the smaller scale of the wave system resulted in a Mach shock configuration at the first separation, and the subsequent flow revealed much weaker wave formations, with the result that the second separation appears to have been very much smaller than the first (in contrast to the first flow, where the second was obviously larger). Clear slip lines are apparent in the flow and the resulting shear layers will have helped to transport momentum to the near wall region, re-energising the boundary layer and further inhibiting separation. Although not shown, immediately after breakaway the flow reverted to this second form, and the enhanced mixing on the inner jet edge will have accounted for some of the disproportionate improvement in the reversion characteristics for the stepped model. A further aid in this direction was that the jet past the step recirculation zone remained practically unaltered by breakaway and so

the broken away jet was turned much further towards the wall than in the unstepped model.

For a smaller step, such as the 1.50 mm one visualised by horizontal knife edge schlieren in plate 7a just before breakaway at $C_{po} = 0.212$, the flowfield was free of Mach shocks and took the same form as the previously described stepped model flow. However, due to the smaller step size, the cell structure was condensed and the waves were damped out earlier, with the result that the expansion causing the end of the second separation was less effective and the bubble was thus more extensive. This agrees with the increase in breakaway performance with step size. Plate 7b shows a vertical knife edge schlieren photograph with a step of 2.55 mm close to breakaway and demonstrates that the reduction of the second bubble with step size appears to have taken place in a continuous rather than a step-wise manner. Also noteworthy is the fact that the transition from Mach shock to the other form took place at roughly the same C_{po} for all the stepped cases at this slot height, which tends to suggest that the interaction of the reattachment shock and step wave reflection at the jet edge were the main determinants of the flowfield in the first cell, since these scale together.

The vertical knife edge schlieren photograph in plate 9b shows the pattern produced by a 6.00/3.75 mm slot-step configuration in the hysteresis zone between breakaway and reversion blowing pressures. The Mach shock flow pattern was clearly established and two extensive shear layers concentric with the Coanda surface are apparent. Most remarkable is the fact that no

second separation can be seen, although the faint line towards the end of the Coanda surface may be the reattachment shock (or compression) arising from a separated zone of extremely small width. For this slot geometry, the flow pattern developed into the full wave system before breakaway, but the altered cell scaling gave a much shorter attached zone between the two separation bubbles. Furthermore, there was no clear reattachment to the Coanda surface at the end of the second separation. Plate 9a of the vertical knife edge schlieren visualisation of the same slot with a 1.50 mm step shows the same wave pattern with a secondary separation, which had no clear end on the Coanda surface. This tallies with the result that, although a step made a noticeable improvement over the unstepped case at this slot height (because a large single separation near breakaway was reduced to two much thinner ones), varying the step size (above 0.75 mm) produced much less effect. Since the reattachment appears to take place in the fully developed turbulent jet on the flat surface, the resistance of the jet to 'peel off' relied mainly on the the jet entrainment capacity at the inner edge which will not have varied drastically with different step sizes and similar wave patterns. Plate 10a of an 8.00/1.50 mm slot-step combination at $C_{po} = 0.360$ just before breakaway shows similar behaviour to that of the 6.00 mm slot case.

7.1.2.4 Surface Oil Flow Visualisation

The surface oil flow visualisations performed upon the planar rig were used primarily to confirm the interpretations of the other experimental visualisation techniques and so only a small fraction of the photographs are shown here.

This is justified by the good correspondence between these results and the ones reported above.

Plate 4a shows the flow pattern corresponding to a slot of 4.00 mm, no step and a C_{po} of 0.325 (the same conditions as in plate 3a). The large accumulation of visualisation oil in the first separation is apparent. The band extended across almost the full width of the Coanda surface, between 12° and 22° from the nozzle, but a small cross-stream variation can be seen. In common with the bands further downstream, it had slight curvature on both sides of the centreline giving it a 'moustache' form. The deviation from uniformity was much smaller at the separation (upstream) edge of the band than the reattachment edge, suggesting that secondary flow within the zone was responsible for the distortion. Thin stripes are also visible at 70° and 90° , corresponding to points where compression wave *contact* with the surface is apparent in the other photographs. Two explanations are possible: the zones may have been separations caused by the oil medium or they may have been a true feature of the flow which is too small to be identified by other methods. Since some disturbance is also to be seen in the surface pressure distributions where compression waves impacted, interpretation as a true feature appears valid, although the oil may have served to alter the separation scale slightly.

What is abundantly clear from the surface flow results is that a significant secondary flow arose at the side walls after the first large separation bubble, which was then amplified at subsequent separation bands. Figure 7.1.31 shows the detail of the surface oil flow and the side-wall visualisation. This appears

to suggest that fairly strong cross stream vortices were formed, which were then swept downstream by the main flow. The main jet flow was narrowed by the growth of the secondary flows and the separation zones were reduced. This, along with the enhanced transfer of mean flow energy to the surface layer by the vortical action, should have resulted in an increase in breakaway performance over an assumed 2D planar jet. In spite of this, by the end of the Coanda surface, some 85% of the cross-section still remained approximately uniform, and the surface pressure tapings continued to lie within this zone, so the other visualisation results from the side and the pressure distributions should have been fairly close to the true 2D form. However, the two side wall patterns were not symmetrical, and this suggests that the secondary flow was quite sensitive to the incoming flow boundary layers or to minor variations in the sidewall geometry.

With the same settings for slot and step (no step) but stronger blowing (close to breakaway with $C_{po} = 0.255$), the pattern became that of plate 4b. The edge disturbances at the first separation bear a resemblance to those of Mehta¹⁹⁸⁸, generated by vortex interaction, and leads to the interpretation that strong vortical structures were formed normal to the surface connecting the start and end of the much larger primary separation. However, the thin oil bands towards the end of the Coanda surface were more even in the cross stream direction than before, the central uniform zone remained the dominant part of the flow and the tapings stay within the central 'potential' core zone. The disturbances in the oil patterns at the tapings in separated zones are interpreted as having been due to the very large viscosity and surface tension

of the oil used. The absence of longitudinal disturbances in the central jet zone on the flat surface (after the tappings) seems to confirm the conclusion that the tappings themselves had no great 3D effect.

Turning to a 4.00 mm slot case with a step (1.50 mm) at similar C_{po} settings to the unstepped case above (plate 6a with $C_{po} = 0.331$ and plate 6b with $C_{po} = 0.257$) gave a surprising result: despite the increased complexity of the flow (particularly the step recirculation zone), the secondary flow extent was suppressed and the separation stripes in the main flow zone were more uniform. Since the major change in the other visualisation results due to the step was greatly reduced recirculation zone scale, this is strong evidence that the secondary flows were heavily affected by the size of the separation bubbles. The step separation zone also appears to show strong cross-stream variation, but no extensive secondary effect is noted in the main jet immediately downstream. This points to two features: firstly, that the boundary layers at the nozzle exit were small enough to have had a minimal effect on the main flow, and, secondly, that deviations from two-dimensionality within a separation zone had a very small direct effect on the uniformity of the main jet. Furthermore, the cross-stream property gradients in the early part of the jet at the edges will have been much higher as a result of the thinner shear layer, which will have caused greater distortion of the planar flowfield visualisations in this region of the model. As before, the total separation area was reduced by the secondary flows, which should have enhanced the breakaway performance in the stepped flare model as well. Many more faint bands were observed in the stepped flow case at $C_{po} = 0.331$, as would be expected from the greatly increased number

of interacting waves. At the higher blowing pressure, the number of visible stripes is reduced, suggesting that wave interference was beginning to play a significant rôle in the flowfield, evening out the surface pressure fluctuation.

7.2 COMPUTATIONAL MODELLING RESULTS

7.2.1 BASE PRESSURE MODEL

The model used to predict the pressure in the recirculation zone after the base step seems to have performed relatively well, despite the fact that the empirical constants used were unaltered from those optimised for an approach Mach number of 1.73 in Tanner's¹⁹⁷⁸ paper, as opposed to the near sonic values in the calculation (and in the actual flow). Figures 7.2.1 to 7.2.4 show that this general observation is not justified for two main cases. In the first case, that of a step which is small in relationship to the slot height, the Tanner method considerably underestimated the base pressure. This effect is attributed to the real flow deviating significantly from the basic assumption of an approximately constant pressure recirculation zone, separated from the main flow by a shear layer, due to interaction with the wall. In the second case, the model failed to find a solution as the blowing pressure reduced towards the choking level. The trend was for both the model and the rig flow to produce reduced base pressures as the blowing pressure falls. A physical limit should be expected when the jet-driven shear layer entrainment is no longer strong enough to generate sufficient recirculation velocity in the separated zone to maintain a pressure which justifies the assumptions of the model. The

fact that discrepancies between model and experiment were more frequently encountered with the larger steps tends to support such an interpretation.

It is more difficult to find an explanation for the fact that the Tanner method appears to have underestimated the base pressure for all cases except the 4.00 mm slot. Careful examination of the diagrams shows that the trend is for the overestimation in the 4.00 mm case to be continued to the 6.00 mm and 8.00 mm cases, unless overwhelmed by the first mechanism described above, with respect to the effect of the shear layer. This further suggests that the 2.00 mm slot recirculation zone is also dominated by shear layer/wall interactions (as might be expected). With this interpretation, the accuracy of the base pressure prediction for a 1.50 mm step with a 2.00 mm slot very close to breakaway appears to have been fortuitous.

7.2.2 METHOD OF CHARACTERISTICS

7.2.2.1 Attached Jet Simulations

The results of modelling the jet without separation are included for comparison with the previous results of Gilchrist¹⁹⁸⁵. However, the stagnation pressure ratios were chosen to match the conditions of other results in the current work, so the plots only approximate to those in the above work. Figure 7.2.5 shows the expansion fan characteristics for a slot of 2.00 mm (with, of course, zero step) at a C_{p0} of 0.243. The correspondence with Gilchrist's figure 3.21A ($C_{p0} = 0.249$) is excellent. However, the application of shock fitting did not enable further marching of the solution, due to numerical breakdown caused by the absorption of too many characteristics into the shock.

Although only the absorption of characteristics from the expansion wave is depicted, characteristics emanating from the initial line were also absorbed.

The same observations apply to the 4.00 mm slot case shown in figure 7.2.6, which corresponds to Gilchrist's figure 3.17B. The shock fitting was somewhat more successful in figure 7.2.7, where the marching successfully crossed the shock and generated an expansion fan reflection at the jet edge. This is because the shock was much weaker at a blowing ratio C_{po} of 0.366. However, the weakening of the wave system applied also to the post-nozzle acceleration, with the net effect that shortly after the shock the method detected subsonic flow and halted. A clear indication of this is given by the first lip expansion wave characteristic which had become almost perpendicular to the flow direction by the time it reached the calculation end. This is shown even more clearly in figure 7.2.8 where an 8.00 mm slot is used at $C_{po} = 0.425$. The general impression of the shock-fitting method for the Method of Characteristics (MOC) in *attached* flow is that, where strong shocks arise, the advantages over an unshocked method are marginal. For weaker shocks, the Coanda flow undergoes subsonic transition shortly afterwards, so in such cases the advantage of the fitting is once again of marginal value.

7.2.2.2 Simulations using Experimental Data

A series of simulations using the experimental values of surface pressure was carried out to confirm that the MOC model was generating reasonable results when correct boundary conditions were imposed. Figures 7.2.9 and 7.2.10 show the situation for a 2.00 mm slot with no step as breakaway ($C_{po} = 0.168$)

is approached. At a C_{p_o} of 0.243, the separation shock/compression was quite weak and easily marched through. A second compression at what seems to have been reattachment of the jet at around 25° coalesced into a strong shock and caused the solution to go subsonic and halt. As the blowing pressure was increased to give a C_{p_o} of 0.176, a strong separation shock formed, halting the solution much sooner through subsonic flow. However, the clearest feature is the enormous increase in the size of the separation bubble. In practice, this seems to signal a transition from thin layer separation, in which the jet boundary layer interacts with the wall along the entire length with strong Chilowsky effect, to a gross separation, in which the governing factor concerning breakaway appears to be whether the pressure in the main bubble is low enough to achieve the eventual reattachment of the jet before atmospheric pressure penetrates to the near wall layer, shortly after the end of the curved surface.

For the 4.00 mm slot case without a step, a similar picture emerges from figures 7.2.11 and 7.2.12, but, due to the reduced blowing pressures and larger cell structures, the solution penetrated further downstream. A remarkable feature is that, despite the difference in blowing pressures ($C_{p_o} = 0.324$ to 0.256), the separation point which results from the experimental data remained at about 15° around the Coanda surface. In figure 7.2.11, the characteristics emanating from the approximate region of separation have been included. Examination of the solution towards the end of the domain shows that, for this case, three separate shock coalescences are to be seen. The first arose from the reflection of the early part of the lip expansion wave from the separation bubble, which suggests that reattachment was occurring there. The second

also arose from the lip expansion wave, and, in the model flowfield, viscous effects from the outer shear layer might be expected to have amalgamated these two compressions. The last of the three coalescences appears to reveal the start of a second separation zone about 40° around the curved surface. An estimate of the reattachment in figure 7.2.12 at $C_{po} = 0.256$, made by scaling the second half of the separation bubble of figure 7.2.11 similarly to the first half, suggests reattachment with a very shallow impingement angle round about 70° . The implications for breakaway (which follows at $C_{po} = 0.250$) again support the hypothesis that the bubble pressure is no longer low enough to bend the jet sufficiently for reattachment.

Figures 7.2.13 and 7.2.14 show that an increase of the slot to 6.00 mm preserved the same basic flow pattern. The separation shock in figure 7.2.13 was weak enough for the method to march through, and the reflection of the shock from the jet edge as an expansion impinged on the zone where the second separation was just beginning. The start of a faint compression, indicating reattachment, can be seen on the last two waves of the lip expansion. The first separation point again remained remarkably constant at about 22° around the Coanda surface.

Results for an 8.00 mm slot are not shown, as the first separation shock in cases with this slot size was strong enough to cause subsonic transition and halt the method. However, the basic flow behaviour in the solutions did not change from that discussed for smaller slots. Discussion of the solutions for

stepped cases will be postponed until the next section since these are better reviewed in comparison with pressure models.

7.2.2.3 Simulations using Pressure Models – Stepped Model

Figures 7.2.15 to 7.2.17 at a C_{po} of 0.331 show the solutions derived for the planar model flow with geometries roughly equivalent to those in the INDAIR flare. Experimental surface pressures (including the step recirculation zone region) were used to generate the characteristic network of figure 7.2.15. Features of note include the rapid coalescence of characteristics at reattachment after the base step (which led, via a shock transition, to numerical collapse of the method), and the influence of the step expansion wave on the rest of the jet (which caused very strong turning of the whole jet towards the Coanda surface). Solution of the same flow using a constant base pressure at the experimental value gave the network seen in figure 7.2.16, which shows the same features but with marching now having passed the reattachment shock, which was weakened both by lip wave reflections from the surface and by direct waves from the step expansion at the outer tip. Counteracting this were the reflections of the step wave from the jet edge, which strengthened the shock. The jet edge reflection transformed the step wave into a compression, which was further focussed by its interaction with the reattachment shock, resulting in another shock running towards a boundary layer interaction at approximately 22° . This latter shock caused the solution to halt due to subsonic transition. This is consistent with the experimental results, which showed boundary layer separation at this point. The assumption of constant

pressure in the step recirculation zone appears to cause little error in the reattachment point. Figure 7.2.17 shows a solution using the base pressure prediction described above, which led to a slightly later reattachment and hence a weaker shock, but this appears to have made no great difference to the development of the solution thereafter.

By increasing the blowing pressure to $C_{p_o} = 0.212$ (shortly before breakaway), the solution revealed strong evidence for the improved breakaway performance of the stepped model. In figure 7.2.18 a very large increase in the cell structure is shown to have taken place, and the interaction of reattachment shock and lip wave extended the zone of favourable pressure gradient at the curved surface, compared to the lower blowing pressure, although this gradient was weakened. Also clearly shown is that the impact of the step wave reflecting from the jet edge as a compression was delayed until much further around the Coanda surface. A comparison with figure 7.2.26 for the same slot of 4.00 mm, with no step and a *higher* C_{p_o} of 0.256, shows that the generation of an adverse pressure gradient was strongly delayed by the 1.50 mm step. Unfortunately, the increased strength of the shock prevented further downstream marching, due to subsonic transition. Since similar results were encountered for all other slot/step combinations, it was not thought worthwhile to present their characteristic networks. Moreover, the general flow behaviour remained similar to the 4.00 mm slot case.

7.2.2.4 Simulations using Pressure Models – Zero Step

The following MOC plots show the results of applying two different separation criteria to the planar model without a step. The results using a criterion based on a minimum value of favourable pressure gradient were practically indistinguishable from those produced by allowing the jet inner edge after the last expansion wave from the lip to float (*i.e.* the jet attached only if a notional separated MOC unit process indicated jet penetration of the surface). Figure 7.2.19 represents the jet issuing from a 2.00mm slot at a C_{po} of 0.258, which was the experimental point for reversion of the jet after breakaway. In this case, the predicted separation was very thin and other evidence suggests that the actual model flow was more or less fully attached.

Figure 7.2.20 shows the jet calculated at $C_{po} = 0.243$ for comparison with figure 7.2.9. The separation in the prediction model occurred slightly later, and the absence of a model for the compression at separation in the prediction technique resulted in a smaller bubble, but, despite this, the reattachment points of the two diagrams are in very good agreement. A second, very thin separation was predicted by the model, and it was the shock generated at this reattachment which caused numerical breakdown. The solution using experimental pressures also showed further evidence of the second separation, so it appears that the simple pressure model gave a very fair approximation to the jet behaviour at this point. Figure 7.2.21 shows the network for this slot at $C_{po} = 0.176$ (shortly before breakaway). The separation grew from a thin strip, and the incoming compression wave from the reflection of the lip expansion coalesced into a shock. This concurs with the surface pressure results which

showed an increasing separation bubble C_p as the blowing pressure increased. However, the solution grossly underestimated the scale of the separation bubble, apparently due to the absence of a model for the separation compression/shock, which is much stronger in this case.

Moving to a 4.00 mm slot in figure 7.2.22 near the reversion point at $C_{po} = 0.355$, shows that the bubble was again quite small. The method marched through the reattachment shock and was halted by a second shock coalescence of the lip wave, which caused subsonic flow. The reflection of the first shock as an expansion wave from the jet edge did not penetrate far enough to weaken this compression. This did occur with slightly stronger blowing at $C_{po} = 0.324$ in figure 7.2.23, but this time the swallowing of too many characteristics by the stronger reattachment shock caused numerical breakdown. Comparison of this diagram with the corresponding experimental pressure solution in figure 7.2.11 reveals very much better agreement than in the 2.00 mm slot case, principally due to the absence of a strong separation compression for the larger slot. Figure 7.2.24 shows the same conditions as figure 7.2.23, but using a solution technique without shock fitting. The breakdown of the method at reattachment shows that the shock fitting procedure did bring some computational advantage over the plain MOC method. Figures 7.2.25 and 7.2.26 show the development of the separation bubble as blowing pressure was increased. A comparison of the maximum thickness of the bubble in the solutions from $C_{po} = 0.355$ to $C_{po} = 0.256$ reveals very strong growth towards breakaway. This provides both a criterion for use of the method in breakaway *prediction* and further evidence for the hypothesis that breakaway is critically dependent on the

failure of Chilowsky effect attraction of the grossly separated jet to the wall. Comparison of figure 7.2.26 to figure 7.2.12 reveals that the agreement between models using predicted and experimental pressures was poorer at the lower C_{po} value. In the latter case, a clear separation shock explains the greater deviation of the prediction model.

For the 6.00 mm slot of figures 7.2.27 and 7.2.29, the pressure model caused separation in advance of solutions derived from the experimental data, and this serves to compensate for the neglect of the separation shock to give very good agreement with figures 7.2.13 and 7.2.14. The intervening solution of figure 7.2.28 failed to reveal rapid growth of the separation zone as breakaway was approached, but this is to be expected, since the bubble was relatively large in all three cases. However, it is noteworthy that the bubble *length* increased dramatically towards the end of the curved surface, where the absence of jet curvature permits penetration of atmospheric pressure towards the boundary layer which then penetrates through the layer to meet the separation bubble. Breakaway would occur when the reattachment compression no longer supplied the necessary pressure recovery as a barrier to flow upstream into the bubble.

The solutions for an 8.00 mm slot depicted in figures 7.2.30 and 7.2.31 confirmed this hypothesis, although the jet did not reattach until after the curved surface (since the jet remains curved, due to the separation bubble). Surface pressure measurements show that for the larger slots, the pressure recovery to atmospheric was indeed delayed until further along the flat surface.

8 AXISYMMETRIC COANDA RESULTS

8.1 EXPERIMENTAL WORK

8.1.1 FLOWFIELD MEASUREMENTS

8.1.1.1 Breakaway and Reversion Tests

The breakaway and reversion tests for the axisymmetric rig necessarily covered a much smaller range than those for the planar model, since the available air supply limited the configurations at which breakaway could be reached. This rig limitation to the coverage is made clear in figure 8.1.1, which shows the results obtained. The breakaway performance rose as the slot height was reduced and also rose sharply when the step was introduced, but further increase in performance fell away as the step was increased. Reversion characteristics (figure 8.1.2) respond in a similar manner, but the diminishing returns as the step increased were less marked.

Comparative breakaway data from Green¹⁹⁸⁷ for an unstepped axisymmetric flare model and similar data converted from a correlation of the full scale methane results (British Petroleum¹⁹⁸⁰) is also given in figure 8.1.1, from which

it can be seen that both sets of data put breakaway lower than the current findings. This may be due to a similar process to that found in the planar model, where the introduction of a discontinuity in the surface at the step caused an increase in performance (Green's model had a smooth transition from the nozzle to the Coanda surface). Differences in the nozzle exit flow should also have had an effect in the axisymmetric case, since the axisymmetric rig was specifically designed to avoid disturbances arising within the nozzle, which were noted in Green's apparatus. Similar disturbances should also occur in the full-scale flare, since that has only a rudimentary nozzle form. Despite the discrepancy between the current model and other results, the general pattern of increasing performance with increased slot and reduced slot is retained.

Another feature worthy of note is that, although the breakaway performance is greatly improved over the planar case, the effects of varying slot height and step height are very similar. This confirms the value of using the planar models to study the axisymmetric phenomenon and suggests that wall effects in the planar model do not have too large an influence on the device operation.

8.1.1.2 Surface Pressure Measurement

The surface pressure curves for the unstepped flare model at small slot heights have forms which are very similar to those obtained in the planar results. A pressure wave system of alternating favourable and adverse gradient regions can be seen in figures 8.1.5a to 8.1.5c for a slot height of 1.67 mm. However, two changes are noticeable. Firstly the 'automatic' expansion imposed

by the radially outward flow partially replaced low surface pressures as the turning influence, this effect being greater in the early part of the jet as the flow there was more nearly radial (for a constant height radial jet, the expansion area ratio would develop as $1/r$). Secondly, the wave pattern was maintained until extremely close to breakaway, as found for the *stepped planar* case.

Two diagrams at approximately $C_{p0} = 0.124$ show the effect of breakaway. Figure 8.1.5c before breakaway shows a separated boundary layer practically all the way along the surface until a pressure peak between 60° and 70° 'seals' the bubble from downstream recirculation. In figure 8.1.5d this disappeared, and fluid at atmospheric pressure penetrated upstream almost as far as the nozzle. The peak on the graphs at 94° is due to a faulty tapping, and data from this tapping was ignored in subsequent results. If a 1.25 mm step is introduced, as in figures 8.1.6a to 8.1.6d, the general appearance of the surface pressure distribution is little altered, apart from the fact that large constant pressure zones (*i.e.* separated) in the troughs did not appear until much closer to breakaway. Furthermore, these zones appeared suddenly and evened out several troughs instead of starting as several troughs and growing together. This may have been due to the much smaller wave scale, which allowed the boundary layer to resist higher adverse pressure gradients over shorter distances, but caused a correspondingly stronger upstream influence once separation did take place. The step separation behaved as for the planar case with C_p rising as blowing C_{p0} increased. However, the increase was not as marked as in the planar case. Although no 'constant' pressure zone was

noticeable at the step, this is thought to be a consequence of the pressure tapping spacing being insufficient to resolve the detail. Figure 8.1.7a with a still larger step (3.13 mm) confirms this conjecture, as the step constant pressure bubble is now clearly visible. The development of the surface pressure in the subsequent figures (to 8.1.7c) followed much the same trend as for the smaller step case, but this time large separation zones could not be achieved within the rig operating limits (in keeping with the higher breakaway limit expected for the 3.13 mm step).

Moving back to the unstepped case, but with a medium sized slot of 3.33 mm (shown in figures 8.1.8 and 8.1.9), the pressure waves became much steeper than for the small slot, and, consequently there was evidence of more extensive separation in the adverse pressure gradient regions. From figure 8.1.9d it is more difficult to ascribe breakaway solely to the absence of a recovery favourable gradient towards the end of the Coanda surface, since no significant peak was visible and the other separation zones had already amalgamated by the time this blowing pressure was reached. Upon breakaway (figure 8.1.9e), the jet remained attached for approximately 6° after the surface pressure fell below atmospheric ($C_p < 0$) in contrast to the planar value of 1° for a corresponding geometry, which suggests that the radial expansion gave the boundary layer/main stream feedback interaction a stronger resistance to upstream influence from the separation. Figure 8.1.8b shows the jet before reversion and reveals that the initial, attached part of the jet grew downstream, but also that the wall pressure all along the Coanda surface was falling. This

would be explained by the separation zone becoming thinner and Chilowsky effect attraction of the jet taking place.

When a 1.25 mm step was added at this slot height, the familiar complication of the wave system recurred, as shown in figures 8.1.10a to 8.1.10d. The changes in the pattern again appear to be due to differential scaling of the wave systems generated by the lip expansion, the step expansion and the reattachment shock. There were only isolated constant pressure zones in the wave troughs, even at a C_{po} of 0.159 (although breakaway for this step/slot configuration was outside the air supply capability, it was only just outside and was expected to occur at $C_{po} = 0.140$). Another significant feature is that the pressure oscillation/wave structure continued to the end of the Coanda surface, even at high blowing pressures. Comparison of the step recirculation zone C_{pb} with the equivalent planar case (figures 7.1.18 and 7.1.19) shows that the axisymmetric step gave a much higher step C_{pb} , which was less effective, but nevertheless much less sensitive to the influence of blowing C_{po} . This sensitivity was further reduced for the larger step of 3.13 mm shown in figure 8.1.11, where little or no dependence of step zone C_{pb} on blowing C_{po} can be seen. In this configuration, the wave system was tighter than before, which would seem to correspond to more wave interference and cancellation. At the highest blowing pressure attainable ($C_{po} = 0.159$), the pressure distribution was similar to that of the planar case just before breakaway (figure 7.1.22). The wave patterns in the axisymmetric case were slightly less smooth, but the major difference was in the jet after the end of the wave structure, which occurred roughly 60° around the surface. Whereas the planar case showed a continuous

adverse pressure gradient to the flat surface, the axisymmetric model exhibited a slight *favourable* one until approximately 80° around the surface.

The unstepped axisymmetric model at the widest slot tried (5.00 mm) gave the familiar simple compression-expansion system, which increased in scale with C_{po} , as is depicted in figures 8.1.12a to 8.1.13e. Evidence of separation at the wave troughs is clearly shown, and the onset of breakaway by amalgamation of the first two separation zones and the elimination of the 'sealing' peak at the end of the Coanda surface is also obvious. Again, the radial expansion at the end of the wave system seems to have been adequate to avoid adverse pressure gradients until close to the flat cone surface. Figure 8.1.13e after breakaway reveals that the jet remained attached for a considerable distance near the nozzle, and reducing the blowing C_{po} towards reversion gave a Chilowsky effect recirculation pressure drop in figure 8.1.12c. The introduction of the step produced much the same effect as for the 3.33 mm slot, which can be seen from figures 8.1.14 and 8.1.15. In both these cases, low surface pressure levels were maintained until practically the end of the Coanda surface. The acceleration caused by radial expansion appears to have provided the conditions necessary for maintaining the wave system which was damped out in the planar case at large slot heights.

The 2.54 mm slot/1.25 mm step case of figures 8.1.16 and 8.1.17 represented an intermediate stage between the cases for 1.67 and 3.33 mm slots with the same step. The pressure patterns before breakaway showed much the same features as those in figures 8.1.6 and 8.1.10. This time, however, it was

possible to break the jet away, revealing the retention of the step recirculation zone in figure 8.1.17d. The subsequent increase of C_{p0} to 0.145 (almost at the reversion condition) gave the pattern shown in figure 8.1.17e, which shows that a strong Chilowsky effect was generated despite the relatively small reduction of blowing pressure from the breakaway condition. This tends to suggest that the step recirculation and reattachment shock were strongly enhancing the entrainment capability of the inner shear layer, thus providing an explanation for the very large effect of the step on the reversion performance.

8.1.2 FLOWFIELD VISUALISATIONS

8.1.2.1 Interpretation of Photographs

Lamont & Hunt¹⁹⁷⁶ point out, in reference to shadowgraph, that even with the system 'focussed' on the central plane, a finite depth of field will reveal non-central features. This tends to confuse the picture if an axisymmetric flowfield is under consideration, since the off-centre flowfield is quite different from the plane under investigation. Moreover, the approximation that the beam deflection is a secondary effect in the results (which is implicitly assumed by interpreting the visualisation as a thin slice), is much less valid in axisymmetric flow. This is because the deviation of a ray (and hence the visualisation effect), in addition to being influenced by the strength of the density gradients, will depend more upon the particular 'history' of the path taken through the flowfield than in the planar case. For the particular case of the Coanda flare model, which has enormous density gradients at shock waves to add to the varying path lengths over which different rays of the probe beam are affected

by the flow, this problem was particularly acute. In the experiments, detail was further obscured by the working beam twice travelling through the very turbulent outer shear layer. This 'double-pass' error made the identification of separation bubbles extremely difficult, since flow features were projected through such zones, which made the bubbles appear to belong to the main jet. Consequently, a great deal of care had to be taken in the interpretation of the results, and comparison between the different types of visualisation at any one flow condition was found necessary to obtain a reliable impression of the actual flow.

8.1.2.2 Unstepped Schlieren and Shadowgraphy

The smallest slot in the axisymmetric model for which flowfield photographs were taken was 1.67 mm, chosen to give the same Coanda radius to slot height ratio as the 2.00 mm step in the planar model. Plate 11a shows a horizontal knife edge schlieren photo of the flowfield at a C_{p_o} of 0.124, just before breakaway. In spite of the nominally zero step, a disturbance is clearly seen emanating from the step location. The edge of the first cell on the open side was strongly curved, but this is obscured to some effect by the axisymmetric viewing, which projected the straight line of the lowest point back onto the near lip region. The large pale band which appears to have emanated from the impact of the lip expansion on the Coanda surface could be interpreted in several ways. However, the shadowgraph for this configuration shows very strong compression wave action, amounting to a shock interaction system at the jet edge, opposite a large separated zone. This shock system lay at a

position in the jet where it would have projected back to produce the band. The relative straightness of the band tends to support this view. Massive separation is confirmed by the separation shock, which can be seen crossing the light band that marked the start of the reverse flow zone. The separation shock and a coalescing compression, which resulted from the lip expansion after wall and then jet edge reflections, met at the above mentioned band, further strengthening the interaction. A reattachment shock can be made out, followed by a further compression, but no second separation structure could be found in the other photographs at this rig setting. Further weakened wave action in the jet was visible downstream, but, by this time, the shear layers appear to have developed across the whole jet height, which is contrary to the planar experience, where this took place much later. The stronger initial acceleration and compression/shock interaction in the axisymmetric model seem to have increased the mixing greatly. The much greater surface area/volume ratio for the jet and the much larger separation bubble scale would also have been involved in the enhanced mixing.

Moving on to a 3.33mm slot, horizontal knife edge schlieren gave the pattern in plate 12b for a blowing C_{p_o} of 0.265. Again, there was a shock disturbance from the nominally zero step, but the internal flowfield in the nozzle appears not to have generated any strong disturbance, implying that, for this configuration, the design was successful. The jet boundary of the first cell did not bulge significantly, indicating that the radial expansion helped to achieve a sizeable proportion of the expansion to atmospheric pressure. Again, to judge by the angle of the shock, strong separation occurred very rapidly as

the influence of the lip expansion on the surface boundary layer waned. The shear layer grew so rapidly that, by the first reattachment shock, the potential core had practically vanished, and, consequently, wave action was strongly damped by turbulent transfer. Further downstream, a number of disturbances roughly normal to the jet flow can be seen, which seems to indicate that what persisted of the wave structure was strong enough to cause very small scale separation bubbles.

Plate 14a shows the same geometry at $C_{p0} = 0.175$, shortly before breakaway, in a horizontal knife edge spark schlieren photograph. Up to the point where the separation shock reached the jet edge, the flow pattern remained much as for the lower blowing pressures. However, the bright band moved out to be coincident with the separation shock, thus obscuring its details. Thereafter, a dark structure roughly parallel to the Coanda surface can be distinguished, apparently in the centre of the jet. Reference to the shadowgraph results for the same configuration shows that this was, in fact, the jet inner edge, thus revealing an enormous separated zone. The detail inside this zone appears merely as a consequence of axisymmetric viewing. Reflections of the lip wave and separation shock produced a very strong cell structure, and by about 65° around the surface most of this had vanished, presumably by transition to subsonic flow. This also marked the point where shear layer growth from the outside and inside edges swamped the potential core. Reattachment then took place very late on the curved surface, and a very faint reattachment shock can be made out at the trailing edge of the last dark zone.

The rapid destruction of the jet core cell system after the first compression is also apparent in the vertical knife edge schlieren picture of plate 14b, which shows the same geometry yet again, but with the jet broken away and a C_{po} of 0.243, just before reversion. Significant jet bending can be seen, suggesting that, in the zone between the jet and the wall, the very rapid increase of the shear layer was driving a recirculation, thus lowering the pressure on the inner edge. This expanded inner layer appears to have been about to touch the wall, closing the first separation into a bubble and causing a chain reaction by the consequent enhanced circulation in the bubble, further lowering the pressure and attracting the jet back onto the wall.

Plate 17a shows the effect of increasing the slot to 5.00 mm. The vertical knife edge schlieren photo at $C_{po} = 0.225$, just before breakaway, again reveals a very large separation zone with a maximum where the lip expansion, surface and radial expansion waves coalesced to form a strong compression. Only a faint trace of the second cell structure is visible at the reflection from the outer edge, as the shear layers grew just as rapidly in this case. The subsequent reattachment must have been very weak, since the corresponding compression can only be made out very vaguely. A small disturbance of the flow at the nozzle is also visible on the opposite side from the expected step irregularity disturbance. This seems to parallel that found in the planar model interferometry, and implies that, at such a large slot, the design of the nozzle no longer gave sufficient acceleration to avoid a small separation on the 'suction' surface. The small structure visible on the lip below this appears to have been outside the jet and, as such, a viewing effect. The alternative

argument that the nozzle is overexpanding on this edge seems unlikely, in view of a critical pressure of roughly 1.8 bar (*i.e.* $C_{po} = 0.528$).

8.1.2.3 Base Step Schlieren and Shadowgraphy

As with the planar model, the introduction of the step made a radical difference to the flowfield. Plate 11b shows the 1.67mm slot combined with a 1.25mm step in a vertical knife edge schlieren photograph. With C_{po} at 0.104, the rig was at the limit of its performance, but extrapolation of the curves for other geometries predict that the photograph represents a condition not far from breakaway. The major effect is quite clear; the massive separation zone in the unstepped case was pushed further downstream and was much reduced in scale. This is surprising, in view of the fact that the step expansion wave should have reflected from the jet edge as a distributed compression to approximately the region of the bubble and thus enhance the adverse pressure gradient. Examination of the shadowgraph for this condition helps to reveal a crossed shock interaction between the step reattachment shock and the coalescing reflection of the step expansion, which concentrated the latter and increased the turning effect on the separated bubble edge, causing reattachment.

The reflection of the step shock at the jet outer edge produced a centred expansion very quickly after the compression zone. As a result of the rapid reattachment, this met the inner edge where the jet was *attached*, and thus produced a favourable pressure gradient to further strengthen breakaway resistance. The straight line through the middle of the first cell appears to

be the projection through the axisymmetric flowfield of the strong interaction between the compression and the step reattachment shock towards the end of the first cell. The reattachment shock from the first bubble was closely followed by a second separation, with its accompanying shock. These two shocks coalesced on the way to the jet outer shear layer, which by this stage had grown very large, thus diffusing the reflected expansion over a wide area. The second reattachment seems to have been the result of strong compression, caused by superposition of the lip expansion wave reflection (compressive, after attached jet inner and free outer edge bounces) and the step-originated wave (also compressive, after reflection at the jet outer edge, the first separation bubble and the jet outer edge again). After closure of the second bubble, the potential core had vanished and viscous action had damped out the cell structure, since no second reattachment shock is visible at the end of the Coanda surface where the jet was attached. The reason for the increased breakaway performance becomes clear; the separation compressions were stronger but more concentrated, so that the flow did not stray as far from the wall, which enabled the inner shear layer to drive the recirculations more strongly and to reduce the separation bubble sizes further.

Plate 12a shows a horizontal knife edge spark schlieren photograph of the same 1.25 mm step with a 2.55 mm slot, which approximates to the geometry of the full-scale flare. The model in this case was being operated at $C_{po} = 0.124$, shortly before breakaway. The inner edge of the jet in the bubble can be clearly distinguished, as for the unstepped case of plate 14a, and it appears that the jet reattached only towards the end of the Coanda surface after all

waves had been damped out by viscous action. As for the planar model, the second bubble amalgamated with the first to form a much larger separation zone near breakaway. The first cell showed much the same characteristics as in the smaller slot case, but thereafter the wave pattern followed that for the unstepped separated jet. Tracing them back shows the wave reflections to have originated from the separation shock, the lip expansion and step expansion waves, as these again became partially superimposed as a consequence of the cell scaling and interaction with the step reattachment shock. The reflections of these waves are only visible about 70° downstream from the nozzle, after which the general dissipation of the cell structure by the shear layers and repeated strong compressions and shocks was complete.

Moving to a still larger slot of 3.33 mm with a C_{p0} of 0.157 gave the vertical knife edge schlieren photograph of plate 16a. Although the airflow at this jet configuration was limited by blowdown time, extrapolation of the experimental curve for other geometries indicated that the model was operating not far from breakaway. In this case, the density gradients were smaller than for the other cases and less detail was obscured. The flowfield again followed the pattern of plate 11b but with an increased scale, which means that the details of the second separation zone were 'hidden' by the effects of viscous dissipation. A significant kink in the step reattachment shock direction took place to mark the incoming compression coalescence and crossed shock interaction. The corresponding horizontal knife edge spark schlieren photograph gave enough extra detail to confirm a second separation zone towards the end of the Coanda surface.

Increasing the step still further to 3.13 mm, but remaining at roughly the same C_{p0} (0.159 in this case) due to the airflow limitations, gave the vertical knife edge spark schlieren photograph shown in plate 16b. The model was operating further from breakaway. The step reattachment shock and a disturbance, which apparently issued from the nozzle and reflected at the jet edge, combined to produce a noticeable Mach-type shock interaction shortly after the reattachment point. The incoming compression from the outer edge reflection of the step expansion wave and the first separation shock combine to produce another shock interaction near the jet outer edge. These two interactions produced the horizontal bars in the step zone, due to axisymmetric viewing, noticed by other investigators (Green¹⁹⁸⁷ and Parsons¹⁹⁸⁸). The disturbance emanating from the nozzle could have been the effect of the axisymmetry on the flow, producing a lip shock. This will be discussed later with the computational results. The incoming compression from the step expansion wave was concentrated by its interaction with the step reattachment shock, and proceeded to form another Mach interaction with the separation shock at the start of the first bubble. The relative weakness of downstream wave action serves to confirm this interpretation. These interactions produced very strong growth of the shear layers, which diffused the edge reflections of the wave system. Consequently, the shocks at the first bubble reattachment and at the second bubble separation were very weak, and subsequent wave action was almost impossible to detect in the visualisation so that no shock is seen marking the reattachment of the second bubble.

The same description applies equally to a large slot of 5.00 mm as the horizontal knife edge schlieren and shadowgraph results in plates 10b and 17b show. The first of these two had a 1.25 mm step and a C_{po} of 0.207, not far from where breakaway was to be expected, whilst the second is of the larger step, 3.13 mm, with a blowing C_{po} of 0.222. The transition from multiple cell system to Mach interaction, which occurred with increasing step size, is again clear. In plate 10b, the second separation zone with shocks at the leading and trailing edges reached practically to 90° downstream of the nozzle. Plate 17b reveals that the disturbance from the nozzle mentioned above, did issue from the near vicinity of the nozzle lip, and, consequently, the influence of a viscous lip shock mechanism would have enhanced the effect.

8.1.2.4 Surface Oil Flow Visualisation

The surface oil flow visualisation results for the axisymmetric rig provided general confirmation of the interpretation of other results. Plate 13a shows the pattern obtained for a 2.54 mm slot, a 1.25 mm step and a driving C_{po} of 0.125, close to breakaway. The bright spots are due to reflections from the illumination system, which could not be eliminated, despite the measures described in chapter 6. The recirculation bubble at the step is clearly marked with oil/dye mixture, and was of relatively small dimensions. After quite a long first cell structure, the separation was marked by a sharp leading edge. The width of this band was larger than first expected, but this corresponded with calculations shown below for the form of the separated zone in the axisymmetric flare. The end of this first bubble was marked by a similarly

extended band, which may have been due to the very high viscosity fluid used for visualisation, in addition to the form of the separated zone. A sharp second separation band appeared almost immediately afterwards (as expected, close to breakaway), followed by a final reattachment band of larger scale, near to (but still noticeably before) the maximum diameter of the flare model. On the cone surface, more or less regular streamwise dye streaks were observed. These were similar to the ones shown in plate 19a for the I8 flare operating on natural gas. This plate shows much the same surface pattern as the laboratory model for the first separation cell, although, with a 6.65 mm slot and 0.55 mm step at $C_{po} = 0.252$, the I8 was operating much further from breakaway. A second bubble, towards the maximum flare diameter, was only made out with difficulty, and the single faint line seems to indicate only a very small separation.

A similar pattern is observed in the photograph in plate 13b, which shows a zero step configuration with a slot of 3.33 mm operating just before breakaway, at a C_{po} of 0.174. This seems to suggest, for the unstepped flare, that the primary separation zone alone reached the critical size for breakaway. The streamwise streaks on the cone were not very distinct in this case. The two large streaks indicate the unequal distribution of dye mixture, since this photograph, like some others, was taken rapidly to avoid running into transient conditions at the end of the pressure tank blow-down. This did not allow transient features on the cone surface to be eliminated before photographing the pattern. In spite of this, the structure in the earlier part of the jet on the Coanda surface varied very little in the cross-stream direction. Although

the pressure tappings cleared small gaps in the oil bands, apparently due to the expulsion of air as the pressure at the surface falls during start-up, no large three-dimensional disturbances were visible.

Plate 15a shows the same slot height with the addition of a 1.25 mm step at a driving C_{po} of 0.209. The appearance of the second bubble, marked by two bands, is now clear, although it was still small. The longitudinal streaks on the cone were still somewhat indistinct. Since these were far from the separation bubbles, it is not thought that they play any great rôle in the performance at breakaway. However, if they persisted in the jet boundary after breakaway, the increased mixing, which can be assumed from the additional gradients introduced into the shear layer, may well have promoted better reversion characteristics.

Plate 15b shows the same stepped geometry as plate 15a, but this time with the C_{po} at 0.174, as in plate 13b. Both separation bubbles were pushed further around the surface without any large difference in streamwise length. The longitudinal streaks were much clearer, and, since it seems clear that they were enhanced by the presence of the second bubble, this may indicate that the width of this separation, and hence the strength of the disturbance at reattachment, was increasing. It should be noted that the *volume* of fluid in the separations would, in any case, have increased as the bubbles move further downstream due to the stronger driving pressure. In the axisymmetric case, this suggests that more shear layer growth can take place in bubbles without

a major deviation of the jet from the surface direction, thus enhancing the Chilowsky effect.

8.1.2.5 Field Tests

In order to confirm that the laboratory model with air produced similar results to a methane flare at larger scale, tests were performed with an INDAIR I8 variable step model with natural gas in a British Petroleum facility. Plate 18a shows a transmission shadowgraph of the model with a slot of 6.67 mm (corresponding to slots of 3.33 mm for the axisymmetric model and 4.00 mm for the planar one). It was only possible to adjust the step in predetermined increments, so the smallest step (0.55 mm) was used in this case. Furthermore, because of the juxtaposition of the visualisation equipment and the inflammable gas, no breakaway could be tolerated, and so the flare was operated at a C_{po} of 0.252, some distance from the expected breakaway (at roughly $C_{po} = 0.200$). In spite of these limitations and the discrepancy in nozzle design between laboratory and field models, the general agreement between seems to be good. The Mach interaction at the end of the first cell and a subsequent shock both lay in positions corresponding to those in the laboratory model jet. Plate 19a shows a surface oil flow visualisation, photographed simultaneously with plate 18a. A sharp band was visible at the first separation, followed quite soon by a band marking reattachment. The oil was then swept from the surface for a considerable distance before a second sharp band marked the second bubble. This pattern is to be expected with

the rig operating far from breakaway, and the reattachment after the second separation took place well before the maximum radius was reached.

Plate 18b shows the largest step of 3.60 mm with the same slot and, in this case, a much stronger blowing C_{p0} of 0.184 could be tolerated without danger. The step reattachment shock was much clearer and reached the jet edge at the end of the first cell, taking part in a Mach shock interaction, just as in the laboratory model. Also similar was the disappearance of strong wave action, which occurred after the reattachment shock from the first separation bubble. Ciné film was also made of the field trials and this shows that, as the blowing pressure increased from the nozzle choking value, the initial four or five clear cells increased in size, and then, as mixing of the shear layers and shock strengths developed, the cells further around the surface are dissipated by viscous action, leaving the two-cell structure seen in the photographs described above.

8.2 COMPUTATIONAL MODELLING RESULTS

8.2.1 BASE PRESSURE MODEL

The base pressure model used for the planar case was also applied to the axisymmetric case, using the Method of Characteristics to adjust for the altered reattachment shock configuration. Some error will arise here, since the notional shock segment was, in fact, a disc, as opposed to a flat sheet, as assumed. However, the main error will arise from the second major empiricism of the method, namely, the constant used to relate the shear layer thickness to

the first coalescence of the reattachment shock, since no alteration was made to account for axisymmetric effects.

Figures 8.2.1. to 8.2.4 show that, as expected, the correspondence with the experimental results was worse in comparison with the planar case. However, the general behaviour of the Tanner model does follow that of the experiment. Another positive point is that the agreement improves as the slot size was decreased, just as in the planar case. Both these facts suggest that corrections to the basic method can be made by appropriate adjustments of the empirical constants (and, in the axisymmetric case, by accounting for radial expansion effects), since the basic mechanism of the prediction appears to have produced the correct behaviour.

The exception to the above was the 1.67 mm slot for the 3.13 mm step when the driving pressure ratio rose. In this case, the reattachment of the jet to the Coanda surface took place much further downstream than in the other cases, and it seems clear that the jet had some difficulty in attaching to the wall with such a large step at the lower speed. That this condition occurred less frequently in the axisymmetric model is understandable, since the jet underwent expansion simply by issuing radially from the slot, which will have dropped the bulk jet pressure, thus more readily turning the jet towards the Coanda surface.

8.2.2 METHOD OF CHARACTERISTICS

8.2.2.1 Pressure Model Simulations

For attached jets in axisymmetric geometry, the calculation led very rapidly to expansion towards the vacuum limit at the surface. The method broke down somewhat before this because the discretised point in the network on the incoming characteristic lay so far from the wall that this characteristic (at a very acute angle to the flow direction) no longer hit the surface. Figure 8.2.5 shows this effect with a slot of 3.33 mm (the separation was permitted where the characteristic failed to hit the surface). This gave a continuous favourable pressure gradient over the first 30° of the surface, which is clearly unjustified by the experimental results. In practice, of course, the generation of very low pressure at the surface increased the following adverse pressure gradient and, consequently, separation took place well before the end of the wall zone which was immediately influenced by the lip expansion fan. Given that the method for the attached jet provided results that were neither helpful in the assessment of jet behaviour nor gave a first approximation of the real jet, it was not thought necessary to present any more of them.

Accordingly, figure 8.2.6 shows the solution for the separation prediction method for an unstepped axisymmetric flare with a slot of 1.67 mm and a driving C_{p0} of 0.202. The radial expansion accounted for some of the initial expansion, thereby stretching the zone of influence of the lip expansion, but simultaneously diluting the strength of the favourable pressure gradient at the wall. The concentrated expansion at the lip also influenced the characteristics emanating from the initial value line, especially in the immediate vicinity

of the corner, and this produced a strong coalescence after reflection from the outer jet edge. For similar characteristics further away from the trailing edge of the lip wave, the radial expansion was enough to spread out the expansion travelling towards the edge so that the reflection was weaker, and then to further weaken the resultant compression after the reversal so that the coalescence was partially 'stabilised'. However, enough strength remained in the earlier compression to eventually cause a shock at the inner edge, which, together with the compression caused by the predicted separation, ended the marching by subsonic transition. Only the coalescing characteristics have been plotted to avoid cluttering the diagram and this policy is followed in most of the other Method of Characteristics (MOC) plots. The result is somewhat surprising, since it gives a mechanism for a lip shock in axisymmetric flow without the aid of viscosity. When the effect combines with that of viscosity (as must have taken place in the actual flow), then the compression will be stronger, and the separation correspondingly earlier.

Figure 8.2.7 shows the same geometry, with the blowing C_{p0} reduced to 0.124, close to where the jet breaks away. Although the marching did not reach the crossing point of lip and separation shocks, the stronger lip expansion and reflected compression from the above mechanism were enough to cause subsonic transition on their own. The figure shows that the assumption of a constant pressure recirculation bubble, which the experimental results justify away from the immediate vicinity of separation and reattachment, gave a much greater offset than in the planar case. Another contrasting fact was that maintenance of the constant pressure bubble in the presence of radial

expansion strengthened the compressive reflection of the last waves of the lip expansion fan from the inner edge of the jet.

Figure 8.2.8 of a 3.33 mm slot case at $C_{po} = 0.265$ shows that the solution was again halted by subsonic transition at the lip shock. The larger cell structure shifted the second reflection of the lip expansion further downstream so that interaction with the separation compression was proportionately smaller, compared with the 1.67 mm slot. Apart from this no other changes in the flowfield structure are to be observed. Figure 8.2.9 shows the solution for an identical case without the shock-fitting method, which was attempted to see if the numerical breakdown could be avoided by allowing the characteristics to cross. As is clear from the diagram, the neglect of the shock caused earlier breakdown, and so all further cases were calculated with shock fitting turned on. The effect of increasing the driving pressure is shown in figures 8.2.10 and 8.2.11 for C_{po} 's of 0.233 and 0.174 (close to breakaway), respectively. The separation point, as for the planar case, remained roughly constant on the surface, but the extent of the expansion fan from the lip increased, and thus the compression, which followed this and turned the jet back towards the surface, occurred later. The practical consequence is that the separation zone grew strongly at breakaway, and thin separation was no longer a tenable assumption for approximating the inner shear layer. At the still larger slot of 5.00 mm, the same effect is to be seen. The calculation of figure 8.2.12 at $C_{po} = 0.225$ was also close to breakaway, and the subsonic halt came somewhat sooner. As for the planar case, the separation point position just

before breakaway is also seen to be fairly constant with respect to the slot size.

The addition of a step introduces more complexity to the flowfield for the axisymmetric case than for the planar case. Figure 8.2.13 shows a slot of 2.54 mm and step of 1.25 mm (approximating the industrial flare) at a C_{po} of 0.163. The Tanner base pressure prediction was also used in this solution. Lip shocks issued from both inner and outer nozzle edges, that coming from the step being expected to reinforce the step reattachment shock. At the same time, the first incoming compression (to the wall) was formed by the reflection of the step expansion wave at the outer jet edge, and it thus occurred much earlier than in the unstepped case. However, the jet separated before the impact with the inner edge, and so, to support the compression, a jet turn towards the wall was necessary. This gives the primary mechanism for the improvement in breakaway performance due to the step, since the turning towards the wall after the first wall separation bubble occurred much earlier. In the centre of the flowfield, a very complex shock interaction was forming and it appears highly likely that the strength of this would be strong enough in the real case (as well as in the solution) to cause a local subsonic patch. The sharp kink in the reattachment shock seen in experimental results would also be reproduced in the numerical method if the marching could be continued. Figure 8.2.14 of the same geometry at $C_{po} = 0.125$, just before breakaway, shows that coalescence of the lip shock and reattachment shock from the base recirculation zone occurred earlier in the cell system, which led to the subsonic breakdown. The separation zone extent grew massively, although

the latter stages of the calculated flowfield would clearly have been altered had the incoming compression/shock from the reflection of the step expansion wave penetrated to the jet inner edge. Thus, it appears that the additional complication introduced by the lip shocks and radial expansion affects only the details of the flowfield configuration, and that the basic mechanism of earlier turning of the separated jet towards the Coanda surface by the step remains the same as found in the planar case.

8.2.2.2 Calculations using Experimental Data

For most cases solved with the aid of experimental surface pressure distributions, the full characteristic network is presented, since this allows the determination of features which were generated by the inner shear layer. Figure 8.2.15 shows the solution produced for a slot of 1.67 mm with a 0.00 mm step setting and a C_{p0} of 0.202. A very faint disturbance from the nominally zero step can just be distinguished. Equally faint is the compression at separation, which can only be seen due to the fact that the first reflection of the discretised waves from the lip expansion ceased to propagate to the outer jet edge as an expansion. If the two characteristics which mark this disturbance are followed through to the reflection at the end of the inner edge, they appear to have started a somewhat stronger compression. The lip shock generated by the solution remained weak, and the marching proceeded after its reflection at the inner edge. The left-running waves from the initial value line accelerated slightly through the expansion fan due to the radial displacement. These waves were reflected at the outer jet edge as compression, but the

subsequent superimposed radial expansion was enough to nullify the effect on the inner jet edge, which maintains the direction imposed by the interaction of the later part of the expansion from the lip with the separated jet. This interaction also caused these waves to coalesce on reflection into a strong left-running shock which caused subsonic transition and halted the marching. The right-running waves from the initial value line picked up expansion from the attached jet at the surface, and, combined with the radial expansion, caused a reversal to compression when they reflected again at the jet edge. The radial expansion, which followed as penetration to the inner edge took place, was no longer strong enough to completely nullify the compression, and, consequently, the jet began to turn back towards the wall. This compression was then immediately followed by the second reflection of the early part of the lip expansion, which gives a much stronger compression and turned the jet almost parallel to the Coanda surface.

In figure 8.2.16 with a C_{p0} of 0.124, just before breakaway, the first separation had moved almost to the leading edge of the lip expansion wave. In consequence, the part of the wave interacting with the separated jet was much larger, thereby massively increasing the initial turning of the flow from the wall. Although the initial value line is not shown (apart from the lip shock, which is much stronger and halts the marching), it is quite clear from the rest of the network that the compression on reflection from the jet edge was much stronger and would therefore have produced a correspondingly stronger turn of the inner jet edge back towards the wall. However a glance at the surface

pressure curve shows that this was not strong enough to promote immediate reattachment of the jet.

As the slot was increased to 3.33 mm in figure 8.2.17 with a driving C_{po} of 0.233, the wave action was considerably weakened by the axisymmetric behaviour. Apart from the somewhat clearer disturbance at the nominally zero step, and the lip shock, which was again strong enough to collapse the marching, the flowfield gradients remained very mild, despite the jet separation. It was not until the C_{po} of 0.174 in figure 8.2.18 was reached that the wave structure returned to the form described above for the smaller slot. At this near-breakaway condition, massive separation was again observed. Especially noteworthy is that the shear layer on the inner surface did not maintain a constant pressure character until the separation distance was much larger than in the planar case. This is to be expected, since subsonic entrained fluid returning along the wall has to contract to maintain continuity, and the consequent adverse pressure gradient (for the reverse flow) provides resistance to separation growth long after the actual separation point.

Figure 8.2.19 for the 5.00 mm slot at a driving C_{po} of 0.314 shows a strong disturbance at the step surface discontinuity, and this appears to have caused separation almost directly from the slot. The apparent compression coalescence, coming from the inner edge at about 8° , seems merely to have been the consequence of the discretisation of the lip expansion, since no major change in jet edge direction accompanied it. The lip shock remained and again caused the method to break down due to subsonic transition. However,

for the same geometry close to breakaway at $C_{po} = 0.225$ in figure 8.2.20, a clear separation compression can be seen at about 5° . As for the smaller slots, this was followed by a further coalescence downstream, where the main constant pressure recirculation zone was established. Comparison with the lower driving pressure shows that the incoming compression, which turned the jet back towards the wall, would have reached the inner jet edge much later, and that, consequently, the scale of the first separation would have grown strongly as breakaway was approached.

Moving on to a solution for the stepped flow, figure 8.2.21 shows the 2.54 mm slot with a 1.25 mm step at $C_{po} = 0.125$, just before breakaway. As for similar planar calculations, the inner jet edge did not meet the surface. This leads to three conclusions: firstly, there appears to have been strong normal pressure gradient in the shear layer, which prevented the inviscid MOC from providing a more or less accurate model of the flow in this zone. Secondly, this will also have strongly affected the base pressure modelling. Thirdly, the MOC seems to be very sensitive to such features. The lip shock on the inner side of the jet was strengthened by the real pressure distribution, compared with the identical geometry and pressure solution of figure 8.2.22, which uses only the experimental base pressure. Earlier marching breakdown was thus caused, and good evidence is thereby given that the lip shocks were not merely a curiosity generated by the calculation. In both networks, the compression caused by reflection of initial value line characteristics from the outer jet edge, was immediately reinforced by a similar reflection of the step expansion wave. This suggests that, in the stepped case, the curtailment of the developing first

separation bubble took place much more quickly compared with the unstepped case. Moreover, due to the added presence of the base step recirculation, the whole structure of the first bubble shifted downstream on the Coanda surface, and, consequently, greater bulk turning of the jet towards the axial direction took place. This accounts for the more marked effect of the step found in the axisymmetric flare. Additionally, due to the much larger separation scale, it is expected that these effects would still have continued to influence breakaway performance strongly at larger steps. This appears to be confirmed by the breakaway behaviour of the axisymmetric model, when compared to the planar one.

8.2.2.3 Field Test Simulations

A number of cases were run for the I8 flare operated in the field tests to confirm that the results generated for the laboratory air model corresponded with those for a real flare. The gas was assumed to be pure methane, and so was still modelled as an ideal gas, but with different values for gas properties. As a sample of these solutions, figure 8.2.23 shows the network produced for a 6.65 mm slot with a 0.55 mm step at a driving C_{po} of 0.252. For such a small step, the developing lip shock from the recirculation zone was amalgamated into the reattachment shock before it coalesced. The latter shock was quite weak and the marching method was able to continue it to the jet edge, where it reflected as a centred expansion (in actual fact, due to the axisymmetry, this was a ring). Since the expansion would only have helped breakaway performance if it struck the inner edge where the jet was attached to the

surface, which seems unlikely from the edge directions shown in the diagram, the step in the axisymmetric case had a self-limiting effect from the wave system, due to the larger separation scale.

Figure 8.2.24 shows the same slot but with a 3.60 mm step and a stronger driving C_{po} of 0.184. The same general pattern shown for the air calculations can be observed. In this case, estimates of the likely behaviour downstream of the solution are more tentative, but it does not seem too unlikely that the jet would have reattached by the time that the expansion, resulting from the reflection of the step reattachment shock at the outer edge, reached the inner edge. If this interpretation is correct, then the expansion would have aided separation resistance by providing a favourable pressure gradient zone. There is thus a further mechanism to account for the continued improvement in the breakaway point as the step height in the axisymmetric flare is increased.

9 DISCUSSION

9.1 EXPERIMENTAL FINDINGS

9.1.1 BREAKAWAY AND REVERSION MECHANISMS

The experimental work on breakaway and reversion demonstrated that these phenomena were repeatable within a small range of blowing pressure. This suggests that both are controlled by distinct sequences of large-scale events, especially in the case of breakaway, since this was completely insensitive to mechanical disturbances of the rig. Reversion could be influenced, to a small degree, which implies that turbulent unsteadiness plays a greater rôle in determining the lower limit of the hysteresis region.

The postulated mechanisms are described in the order in which the experiments were performed, since this facilitates the explanation. Starting with breakaway in the unstepped planar model, as the blowing C_{p0} fell (rising pressure), the cell structure scales approximately like that of a free jet with its centreline at the curved wall. Two separation bubbles appear as breakaway is approached, and these gradually increase in size. These amalgamate at a

critical value of C_{p0} , and reverse flow takes place between the second bubble and the first, which is at a lower pressure before amalgamation. The resultant increase in the size of the joint bubble has two effects: firstly, the recirculation velocity, driven by the main flow, drops, and secondly, the reattachment point wanders downstream. Both of these factors raise the static pressure in the bubble. This process is clearly unstable, and the jet rapidly flips off the surface.

Evidence for the existence of the separation bubbles is derived from the different flow visualisations and the surface pressure measurements. The justification for assuming that the opening of a path for reverse flow between bubbles is the culprit comes from the phenomenon of partial reattachment, which proves that a stable first separation bubble is possible, even though the second is fully open to atmosphere. The fact that this reversion type did not take place in the unstepped flare is ascribed to the strength of the reversion mechanism at the higher C_{p0} with this geometry, compared to the stepped case. This hypothesis of breakaway when the second separation point reaches the first reattachment is similar to that of McGlaughlin & Taft¹⁹⁶⁷ in their work on fluidic elements. The same mechanism is also mentioned in connection with airfoils by Sirieix¹⁹⁷⁵.

Turning to the corresponding reversion, as C_{p0} rises and the jet momentum falls, the initial separation point wanders upstream on the curved wall, since the boundary layer is less able to resist the adverse pressure gradient. However, this means that the rapid growth of the boundary layer takes place slightly

earlier, and the entrainment from the near-wall region is mildly enhanced. More important is that the static pressure drop in this region, due to the recirculation velocity, is better able to bend the jet with its lower momentum. These effects combine at the critical C_{po} , when the edge of the inner shear layer approaches the wall and seals off a bubble from the near-atmospheric pressure further downstream. The recirculation velocity is then immediately increased, the pressure in the bubble reduces still further and the jet is sucked onto the wall in a classic demonstration of the Chilowsky effect. This accounts for the slight sensitivity to disturbance of the rig, since this will increase the turbulence of the shear layer and also affect the bubble thickness.

The primary effect on breakaway of the introduction of the base step is that the jet structure now scales more like that of a free jet with the same height as that of the flare model. The separation bubbles are consequently much smaller and more numerous, permitting two to amalgamate without causing the reattachment point of the pair to jump into the high-pressure zone at the end of the curved surface, where the jet is 'straightened up'. Breakaway then occurs when a third bubble joins with the first two. In fact, it appears from the experimental results that the correct sequence is that the second and third bubble joining followed by breakaway when the first bubble joins the pair. The point at which this happens depends to a large extent on the step geometry (relative, of course, to the Coanda surface radius and slot height), but the actual mechanism of breakaway is unaltered from the unstepped case, although the critical pressure is much higher.

The similarity is less strong in the case of reversion, since, in all cases examined, the recirculation zone behind the backward-facing step at the nozzle exit was retained, regardless of whether the jet had broken away or not. This zone causes an acceleration of the broken away jet, which turns it towards the wall in order to lower the static pressure at the inner edge to that of the strong recirculation in the bubble. A related effect is that the initial boundary layer, in which the turbulence collapses after the very strong acceleration in the nozzle, undergoes very strong growth as a result of interaction with the step bubble, thereby increasing its resistance to the eventual separation from the Coanda surface. All the above factors lead to the jet inner edge being much closer to the curved wall in the stepped case, which accounts for the appearance of the Chilowsky effect reversion described above at much higher blowing pressures. Some trade-off would be expected from the energy lost in traversing the step zone reattachment shock, and this accounts for the diminishing returns with increasing step size. For the larger slot heights the energy loss seems to produce a negative offset, from the unstepped case, which virtually nullifies the advantage of using a step, at least from the reversion viewpoint.

Moving on to breakaway in the axisymmetric flare model, but again taking the case without a step first, the same mechanism is again apparent. However, the radial expansion provides additional means for lowering the jet bulk pressure, enabling the surrounding atmosphere to keep the flow pressed more firmly onto the wall. This reduces the bubble sizes and thus retards the onset of the amalgamation sequence leading to breakaway. The radial expansion

also enhances the separation resistance of the boundary layer (discussed in chapter 8), which further delays the bubble growth.

The comparison with the planar model is complicated by the significant end wall effects which were observed. On the end wall, the boundary layer experiences a cross-stream pressure gradient, which rises strongly towards the outer edge. The reduced ability of the end wall boundary layer to resist this gradient, compared with the main part of the jet, permits the penetration of higher pressure fluid into the bubbles from the corners, thereby diminishing the breakaway performance over an ideal two-dimensional case. The penetration also gives rise to a vortical secondary flow with the axis in the streamwise direction, which seems to couple to the strong vortices with cross-stream axes in the recirculation zones. The resulting vortex structure is similar to that of a finite airfoil, and the consequent strong mixing will bring momentum from the main jet into the curved wall boundary layer, and so, paradoxically, help to delay the breakaway mechanism. The proportional improvement obtained by moving to axisymmetry is relatively insensitive to slot/radius ratio (*N.B.* slot height in the axisymmetric model scales by a factor of 1.2 to give the planar equivalent). A consideration of the wide variation in cross-stream pressure gradient for different geometries suggests that the above effects for the planar case could offset each other to a large extent.

Such a conclusion must, however, take into consideration that these effects will cause a deviation from two-dimensional separation zones, and Korkegi¹⁹⁷⁵ points out that a skewed shock on a compression ramp induces earlier separation

than the 2D case. Thus cross-flow variations would once again lower breakaway resistance, since the incoming compressions from jet outer edge reflections of the lip and step expansion waves are effectively skewed with respect to the separation zones. Patankar & Sridhar¹⁹⁷¹ also report that the angle of separation for a 3D *incompressible* circular wall jet is lower than that for the 2D case. The subsonic work of Felsing & Moller¹⁹⁶⁹ reveals the sensitivity of such wall jets to injection, and leads to the suspicion that leakage into the separation bubbles through the sidewall seals accounts for some part of the lower breakaway pressure ratio in the planar model. It therefore appears that any offsetting of positive and negative influences of departures from two-dimensionality is subject to a very complex interaction process, and, although the net result is similar at all slot heights, the extent of the reduction of breakaway performance cannot be so easily appreciated.

For reversion in the axisymmetric unstepped model, the process is similar to that of the planar case. However, the comments above on the increase of boundary layer separation resistance due to radial flow effects apply equally to the reverting jet. The bending of the jet, caused by reduction of pressure on the inner jet edge due to the Chilowsky effect, will be further enhanced by a consequent cross-stream gradient, also due to the radial expansion. This amplification becomes more pronounced as the jet turns further towards the vertical, and the stronger effect towards the point where reattachment takes place causes earlier closure of the bubble. The cell structure of the axisymmetric jet is also more bulged, as the strong radial expansion at the nozzle exit increases the effect of the centred expansion at the lip, giving

stronger flow turning across the jet. This gives a positive effect on the size of the shear layers which is the major determining factor in the critical C_{p0} for the onset of Chilowsky effect jet reversion.

Turning to the last category, that of the axisymmetric model with a step, it can be seen that the general trend of the breakaway results was similar to that of the planar model, but diminished improvement of the performance as the step size is increased was much less marked than in the planar case. This corresponds well to the much shorter bubble lengths in the axisymmetric flare, since these give more space for growth with step height before breakaway improvement starts to be compromised by amalgamation of the bubbles. The growth in the size of the step recirculation zone is also lower in the axisymmetric case which maintains the bubble system at a greater distance from the higher pressure zone at the end of the curved surface, thereby further delaying the final stage of the bubble size jump which leads directly to breakaway.

The reversion performance for the stepped variant of the axisymmetric model did not show the trade-off effect noticed at larger slots in the planar case. It is difficult to be fully categorical on this point, since the geometries which could be broken away within the air supply limits (a necessary precondition for investigating reversion!) leave the performance of the largest slots relatively unexplored. The radial expansion does cause a turning in the jet edge opposite the step recirculation zone (nominally constant pressure), which will tend to weaken the reattachment shock significantly, thus occasioning a much smaller

loss of jet kinetic energy and accounting for the improved step reversion behaviour in axisymmetry.

Although both breakaway and reversion characteristics are markedly improved upon the addition of axisymmetry and steps to the 'basic' unstepped planar configuration, the latter showed the greatest decrease in critical C_{po} . This is precisely what would be hoped for, since it offers the prospect that further alterations will give the best effect in the limit which controls the application of the flare (as discussed in section 2.2.2).

9.1.2 RELEVANCE OF PLANAR WORK TO THE AXISYMMETRIC MODEL

The general impression from the results is that the planar and axisymmetric model behave in very similar ways, despite the obvious superiority of the axisymmetric geometry with respect to breakaway. In particular, the effect of varying the slot height is practically identical, and the effect of the step is also very close in the two cases.

The flow visualisations and other experimental results confirm that this correspondence extends to the details of the jet structure. Furthermore, since the calculations also show marked similarity, there is considerable justification for the use of planar models as a preliminary technique for future development, in order to reduce both cost and computational problems. Since the improvement in reversion characteristics for axisymmetry has been shown to be even better than that for breakaway, a planar model represents a doubly conservative underestimate of a design's capabilities.

This close correspondence also leads to the conclusion that the axisymmetric flare produces a very close approximation to true two-dimensional flow, at least in the parts of the jet which influence breakaway and reversion.

9.1.3 RELEVANCE OF LABORATORY RESULTS TO INDUSTRIAL FLARES

Figure 8.1.1 shows that the correlation for breakaway derived by B.P. from experimental gas-burning flares agrees with air flare model results from Exeter University, after application of a hypothesised correction for gas properties, which, consequently, seems to be well-justified.

The test results from the current work were significantly better than either of the two studies above. In spite of this, the general behaviour with respect to slot and step variation is the same, and it seems fair to take this as indicative that identical flow mechanisms are responsible for breakaway in all three studies. The flow visualisation results from the field tests are also very close to the laboratory ones, as comparisons of plate 13b with plate 19a and plate 16b with plate 18b (which represent roughly equivalent pairs) demonstrate.

The major difference between the axisymmetric model studied in the current work and that of the B.P. and Exeter University studies is the alteration in the design of the nozzle, to minimise both internal disturbances and separation before the lip edge. That this produces such a large effect is surprising, in view of the insensitivity of the inviscid calculation to the initial conditions, and gives further grounds for requiring a fuller computational

representation of the flowfield physics. The alternative argument, that the small disturbance due to the discontinuity between the step shaft and the Coanda surface is causing the discrepancy would only apply for the zero step case, and the B.P. correlation (with gas correction) shows that this discrepancy is maintained at non-zero steps. Overall, this suggests a further avenue for the optimisation of the flare performance, but one which would require considerable experimental and computational work.

9.2 COMPUTATIONAL MODELLING

9.2.1 BASE PRESSURE MODEL

The Tanner base pressure prediction has been applied with reasonable success for the planar flare simulations, except at conditions approaching nozzle choking. This seems to indicate that the recirculation characteristics of transonic base steps are markedly different from those in which supersonic flow is well established. The agreement for most of the calculations is not perfect and suggests that an optimisation of the empirical shock stand-off variable, which was set by Tanner for the best match to the data at $M = 1.73$, would be useful.

In axisymmetry, the agreement is far from satisfactory, and it seems that a thorough revision of the empirical bases of the model is required. The profile of the reattaching shear layer should be altered to account for different shear layer form in axisymmetry, and the shock stand-off ratio needs adjusting for

the different rate of coalescence of the characteristics which emanate from the viscous layer into the main flow to give a reattachment shock.

It should be noted that the model is applied to a jet case, where additional cross-stream influences complicate the flowfield, whereas it was originally developed for an obstacle placed in uniform two-dimensional supersonic flow. The good correspondence in the planar case therefore serves to confirm the strength of the basic theoretical justification for the method, and suggests that further work in the area of base flow prediction would do well to follow this line of analysis.

9.2.2 METHOD OF CHARACTERISTICS

In planar geometry, the combination of a simple separation criterion and a shock-capturing (and shock-fitting) algorithm has produced valuable information for the interpretation of breakaway mechanisms. However, the calculations predict the appearance of strong shocks in the flow, which causes numerical breakdown of the method. This problem appears to be due both to genuinely strong shocks (leading to subsonic transition) and to inaccuracies generated by the coalescence of too many characteristics at shock waves. One development of the Method of Characteristics (MOC) might be possible by using the solution shortly before such numerical breakdown to generate a new (interpolated) initial value line, which could then be used to resume the downstream marching.

Without the suggested modification, the algorithm performs relatively well for the unstepped flare model, but is somewhat restricted in the downstream distance for which a stepped case solution can be marched. The information which is gained about the near-nozzle region is still very useful in understanding the breakaway behaviour. The rapid growth of predicted separation bubbles as the experimental breakaway point is approached gives a useful criterion for design of unstepped flare surface contours, and may provide the same for stepped flares if it proves possible to extend the MOC as suggested above.

In axisymmetric geometry, the wave systems are even stronger, so the numerical breakdown in this case seriously affects the calculation of unstepped cases. In spite of this, a wealth of detail has been revealed in the early stages of the jet, particularly by applying a MOC variant which uses inner edge pressures specified by experimental values. An inviscid mechanism for the generation of lip shocks has been demonstrated, and the reason for computational failure of attached jet studies has been shown to be expansion towards the vacuum limit, which causes improbably large inner edge velocities. This expansion has given an important insight into the physical process of separation in the axisymmetric flare. The networks show that the characteristic spacing becomes very large as a result of the stronger expansion in axisymmetry, and thus the solutions in this case may also be amenable to refinement by restarting the MOC with an interpolated initial value line.

The experimental results have revealed the existence of Mach shock planes and rings for certain geometries at specific operating conditions (usually quite

far from breakaway). The general picture thus seems to be that the MOC alone will not be enough to fully model the jet core region, but that the insights which it provides into the fluid dynamics of the flare more than justify its application as an initial stage in the calculation.

9.2.3 BOUNDARY LAYER METHOD

It did not prove possible to match the boundary layer marching method with the MOC. The primary symptom of this problem is a large discrepancy between the viscous layer thickness predicted by each of the two methods, even when experimental data was used as the basis for both techniques. The MOC produces boundary layer thicknesses which are clearly far too large, and this is also noticeable from the MOC calculations for stepped cases using the experimental data, since the jet remains detached from the surface despite the appearance of reattachment shocks in the solutions. The interferometry reveals that, shortly after the influence of the lip expansion wave reaches the Coanda surface, significant normal pressure gradients arise, and in the unstepped case this is precisely the point at which the boundary layer and MOC methods diverge.

The boundary layer method, as implemented, neglects normal pressure gradients, thus giving a source of error. Further inaccuracies arise from neglect of wall curvature. The MOC has the unfortunate property that the inaccuracy accumulates as the marching proceeds, in contrast to other iterative methods for the jet core flow, so that, for interaction zones of significant length, additional numerical difficulties are to be expected.

Due to the above problems, extremely rapid breakdown of the matching calculation takes place when the MOC is coupled directly to the boundary layer. It seems, from the magnitude of the discrepancies, that refinement of the methods is unlikely to be enough to resolve the difficulty. The use of a third deck (a rotational MOC layer with the same stagnation pressure distribution as the supersonic part of the boundary layer) might be used to avoid the problems, but this would require a substantial amount of recoding to implement. Furthermore, this approach requires work to define the sonic velocity point for the integral profiles, which would need significantly more time than was available for this part of the project. The advantage of following this line of enquiry is that the intermediate deck could be checked with the experimental surface pressure distributions and MOC alone to see if the improvement is promising, before pursuing the work on the profiles.

The same remarks apply to the alternative of applying the Myring & Young¹⁹⁶⁸ technique of redefining the integral profile along Mach lines in order to resolve the normal pressure gradient problem. The necessary adjustments to the MOC would be simpler, but those required for the boundary layer more complex, so that the net effect in terms of development time would be similar.

9.3 OUTLOOK FOR SUPERSONIC COANDA JET RESEARCH

9.3.1 SUMMARY OF CURRENT POSITION

Breakaway and reversion tests, flowfield and surface flow visualisations and surface pressure measurements on planar stepped, axisymmetric unstepped

and stepped and industrial flares have all been successfully carried out. The results are substantially consistent between geometries and reveal that the basic mechanism of breakaway remains the same. The correction used by B.P. for different jet gases is justified by the results, as is the correlation for flare breakaway. However, changes in nozzle design appear to have a definite influence on breakaway performance which has not yet been fully explored.

Techniques have been developed that reduce the time delay in making rig measurements, which should improve the comparability of the results. The interferometer for the planar flare model has been improved to the point where optical effects in flowfield are the only remaining obstacle. Further progress in this area could only be achieved at the expense of major changes in the optical rig.

The Method of Characteristics has been developed to capture shocks within the flow. The technique is reasonably successful for the unstepped planar model. In spite of this, the strength of the shock waves predicted in stepped models (including the axisymmetric case) is sufficient to produce areas of subsonic flow in the jet core, which are also apparently present in experimental studies. The method is still useful for providing insights into the breakaway behaviour of the jet and will also be of considerable help as a starting point for more complex and expensive iterative simulation methods.

An integral boundary layer marching method has been developed to a preliminary stage. Considerable problems have come to light in attempts to

incorporate it into the MOC via a coupling algorithm. These difficulties suggest that the effort which would be required to complete this section of the project would be better spent in revising the whole computational approach. However, advice and evidence from the literature suggest that other approaches are also likely to involve a considerable amount of extra work, due to the extreme complexity of the flowfield revealed in the experimental results.

9.3.2 POSSIBLE DEVELOPMENT ROUTES

Relatively few areas are left outstanding on the experimental side, as far as the INDAIR flare is concerned. High speed camera visualisation work is still required to provide definitive confirmation of the breakaway mechanism inferred from the other experimental results. However, a very high framing rate will be needed (a 20 to 40 μs exposure time has been estimated to give only 10 frames during the breakaway process). This would be neither simple nor cheap to develop, since the necessary film illumination and synchronisation with the flare imply a requirement for an expensive light source and for a comprehensive control system for the air supply.

An improvement in the techniques for collecting flowfield quantitative data is highly desirable to enable investigations at blowing pressures higher than those accessible with the current equipment. The use of speckle interferometry or similar whole field techniques is liable to lead to the same disadvantages in terms of cost mentioned above in reference to the high-speed visualisation.

To be generally useful in both planar and axisymmetric flare models the application of laser doppler anemometry (LDA) would be the best option, but this again carries cost penalties if an existing installation proves to require substantial modification. Flow seeding is already present in the air supply to the models as a result of the imperfect operation of the filters, which should, in consequence, be relatively tightly controlled. However, there remains the problem of seeding the entrained air in an equivalent fashion.

An aspect of the investigation which could be confirmed at reasonable cost, is whether the substantial increase in breakaway performance in the axisymmetric model over previous ones is indeed due to the alterations in nozzle design. This requires only the replacement of the lip tube and the step shaft with equivalents modelling the earlier nozzle. The axisymmetric model might also be worth testing on the real fuel gas, if suitable safety precautions could be arranged, since this would allow both comparison between air and natural gas, and the available flowrate (much larger than that achievable in the air rig) would permit a broader map of breakaway to be investigated.

An attempt to reduce the 3D effects in the planar model would be of more academic interest. This would increase the value of comparisons with axisymmetric behaviour, but it would also provide a stronger link with planar *subsonic* results. Achieving the reduction is not likely to be easy in view of the results for the form of the flare flowfield. If fences are used for this purpose, the rapid growth of the boundary layer due to the shock interactions would need a considerable number of separate fences, and therefore a large increase

in the airflow requirement. Moreover, there is then a danger that a separation bubble falling at the edge of a fence would open to atmosphere, and the consequent early breakaway would totally invalidate the experiment. Suction of the sidewall boundary layer would also give invalid results, since it would be almost impossible to arrange the abstraction points to be effective, without simultaneously taking fluid from the separation bubbles and thereby delaying breakaway. For both options the optical arrangements are also likely to be disturbed and correspondingly worse results would be obtained. Increasing the slot height to width ratio again increases the airflow requirement.

Moving on to the computational modelling gives wider opportunities for further development. Mach shocks, subsonic transitions and strong boundary layer interaction cause significant difficulties in applying any solver, but particularly the MOC – boundary layer approach discussed above. New shock-capturing Euler codes have recently been reported (Marsilio & Moretti¹⁹⁸⁹), which would permit the direct application of Drela & Giles¹⁹⁸⁶ method to the INDAIR case, and hopefully eliminate the matching problems by the implicit iterative coupling. This would also provide scope for modelling the effect of shock reflections, which travel to the inner edge from the jet outer edge, and are an important influence on breakaway behaviour in the stepped cases. The implication that diffusion of shocks/compressions in viscous layers is crucial means that the success of simple boundary layer methods is likely to be limited.

It should be pointed out that the appearance of the Mach shock and consequent breakaway in a zone of subsonic flow invalidates the choice of most multi-zone methods for modelling, since the complexity is so great that placing the zone boundaries cannot be practically achieved without prior knowledge of the flowfield. This places a limitation on such methods for design work, since, if alternative geometries produce very strong shocks in analysis, one could not be sure that the physical flow did not give rise to Mach reflections. The only other multi-zone methods which have been found useful in INDAIR-type flows have been overlapping types, which implies that a considerable effort would be required to incorporate the shock-capturing process without prejudice to the stability of the coupling. Moreover, the greater the degree of overlap, the worse would be the computational efficiency, and the importance of shock diffusion implies that large overlaps are necessary.

The alternative of using a full Navier-Stokes solver offers better accuracy, but at the cost of yet more computational resources and reduced stability. The turbulence modelling in the latter case would also provide a considerable challenge, because of the very strong non-linear effects. Whatever the approach chosen, the MOC work will not have been in vain, since an iterative method will require a more or less accurate start point to be efficient and to avoid a 'false' solution (since the physical flow has two possible modes in hysteresis zone).

9.3.3 IMPLICATIONS FOR DESIGN IMPROVEMENTS

The mechanisms suggested above place the responsibility for breakaway upon the interaction of the various wave systems with the boundary layer, which implies that the alteration of the surface profile to reduce adverse pressure gradients would have only a secondary effect upon the breakaway performance. The primary effect is the reduction of the cell scale, which appears to give the Chilowsky effect in the bubbles greater scope. This accounts for the effects of both smaller slots and the addition of steps.

Measures to condense the cell structure would involve introducing curvature discontinuities in the surface to give rise to additional wave systems. This would be limited to regions of flow where the jet is attached, which means, in practice, the early part of the surface, thereby limiting the space available for such improvement. Breakaway performance is more likely to be enhanced by shapes producing mainly left-running shocks, since these are reflected at the jet outer edge as expansions and are seen as favourable pressure gradient zones at the boundary layer. These shocks would also increase the mixing layer turbulence, but the curvature changes to produce necessary compression act in the opposite direction from that required to turn the jet from the radial horizontal direction to the vertical. The appearance of extra right-running compressions or shocks arising from contour changes in the opposite sense (increased net curvature) would only be an advantage if they could be arranged to interact with separation bubbles, whereby they would cause the jet to turn towards the wall.

Another possibility would be to continue the Coanda curvature to a greater angle, with the objective of increasing the distance between the separation bubbles and the pressure recovery region, combining this with compression curvature at the transition to the cone surface ^{using} the main jet momentum λ to develop a 'seal' against the high pressure which penetrates through the boundary layer from the cone. Reducing the initial exit diameter of the nozzle would introduce stronger radial expansion throughout the jet, which should act against breakaway, but this would simultaneously decrease the discharge of the nozzle, and so prejudice another parameter of the design.

The process in which the jet breaks away due to penetration of high pressure into the bubble suggests that breakaway might be eliminated or delayed by the inclusion of a second step towards the end of the Coanda surface. The fact that the step recirculation zone is retained, regardless of jet mode, is further encouragement for this approach. However, care would need to be taken to avoid placing the new step under an existing separation bubble, since this would weaken the Chilowsky effect and accelerate the onset of breakaway. Such a design would be especially dangerous for the bubble 'jumping' at amalgamation, since this might easily cause the separated zone to spring over the new step, thereby defeating the objective of sealing off the high pressure zone. Another weakness is that the second step, due to the low pressure recirculation zone, might well accelerate the flow sufficiently to maintain supersonic flow over a much longer distance thereby substantially increasing flare noise levels.

The introduction of profiling of the step cavity has been suggested as a means of increasing breakaway performance, but the work of Tanner¹⁹⁸⁸ suggests that, within a broad range, the configuration of the boundary of the dead-air region has a minimal effect on the base pressure and hence on the external flow. This is confirmed, to some extent, by the evidence showing diminishing returns with increasing step height, which indicates that the Chilowsky effect is smaller as the zone size is increased.

The remaining option is to attack the boundary layer separation problem directly. Using measures to cause transition to turbulence as soon as possible would seem to be sensible, since this should promote both separation resistance and recirculation strength in the bubbles after jet separation. Vortex generators could be installed to increase the amount of main jet momentum which re-energises the near wall layers, and also to weaken the wave system, but this would turn the flow fully three-dimensional with an order of magnitude increase in the difficulties of computational modelling.

More drastically, suction could be applied to the wall. By definition, INDAIR flares for high pressure use reach choking conditions, so that a small nozzle incorporated internally in the flare could be designed for massive overexpansion, in order to generate the necessary surface pressure drop. Axisymmetric geometry gives the ideal opportunity for the large area ratio required. The major disadvantage at low flow rates is the presence of gas in the flare with potential for flashback. Moreover, this approach would complicate the manufacture considerably and hence increase the costs.

Manipulation of the flare profile to alter the general form of the jet will be more amenable to analysis, and will probably be much cheaper than using methods to optimise the boundary layer. However, both techniques hold out some potential for an increase in the INDAIR performance.

9.3.4 BY-PRODUCTS FOR OTHER PURPOSES

The rotational two-dimensional Method of Characteristics has been implemented in a program with two stages of modularity. The first stage is comprised of modules for the individual unit processes which have also been developed for shock-capturing flow. The second stage lies in the decoupling of the main network logic from that for the boundary conditions. It is hoped that these features will make the current program useful in other situations for which the MOC is suitable. The code is applicable to cases where shocks are not overwhelmingly strong, and it shows some improvement as a shock simulation technique over allowing the characteristics to cross.

The curved supersonic wall jet flow seems to be dominated by wave effects, and the limits to breakaway performance are set by boundary layer/shock wave interaction, which suggests that further research in the field of supersonic wall jet separation should concentrate on following this line of enquiry. The complexity of the flowfield revealed in the experiments makes the flow an ideal test case for non-equilibrium turbulence models, although appropriate experimental work on the turbulence structure has yet to be carried out.

A relatively inexpensive interferometry/schlieren/shadowgraph system has been refined to deal with flows having quite high shock wave strengths. The equipment is very flexible and can cope with a wide variation in flow conditions with minimal adjustment.

10 CONCLUSIONS

- Experimental studies have been carried out on a stepped planar flare model. These include interferometry, a range of optical flowfield visualisation methods, surface oil flow visualisations and surface pressure measurements.
- A stepped axisymmetric flare model running on air has been studied in the laboratory using a range of techniques, which includes optical flowfield visualisation, surface oil flow visualisation and surface pressure measurement. Similar, but simpler, tests have also been carried out upon an axisymmetric flare model operating with combustible gas.
- The rotational Method of Characteristics (MOC) has been applied to the flare flowfield, with adaptations which capture and fit shocks. It demonstrates considerable advantages in assisting the understanding of the fluid dynamics, but the technique was unable to model all the complexities of the jet flow accurately.
- Simple models for centred expansions, the rear-facing step base pressure and jet separations have been applied to the MOC as boundary conditions. The

expansion and separation models were quite successful in both planar and axisymmetric flow, whereas the base pressure model accuracy was only acceptable for planar flow. However, results for the axisymmetric case suggest that the basic approach used in this model was correct, provided that the near step flow is sufficiently far away from the transonic regime.

- In spite of considerable effort, it did not prove possible to match an integral boundary layer calculation with the MOC. Given the strong interaction between the main jet and the wall boundary layer revealed by the experimental work, and in view of the limitations of the MOC, the best prospect for further computational development appears to be the implementation of a single calculation method for the whole jet.
- From the experimental and computational evidence, the mechanism of jet breakaway appeared to depend on the amalgamation of separation bubbles, leading, via reverse flow, to strong bubble growth and consequent failure of Chilowsky Effect wall jet deflection.
- Smaller slot height/Coanda radius ratios reduced the pressure cell scale of the jet which reduced separation bubble sizes, and hence the onset of the breakaway mechanism as the blowing pressure increased was delayed. The addition of a rear-facing step to the start of the Coanda surface had a similar, but much stronger, effect upon the jet structure, which, combined with an increase in the turbulence of the wall boundary layer, also delayed separation and breakaway. Axisymmetry superimposed a favourable radial pressure gradient on the jet, which further aided breakaway resistance.

- The flare flowfield contained a number of features which tend to complicate turbulence structure. Detailed studies are required to refine understanding of the turbulence behaviour, and thus provide an extremely demanding test case for complex turbulence models.

LIST OF REFERENCES

- Abdol-Hamid K.S. & Wilmoth R.G. 1989
Multiscale Turbulence Effects in Underexpanded Supersonic Jets
A.I.A.A. Journal vol.27 no.3 315-322
- Ackroyd J.A.D. 1975
Fluid Mechanics considerations in supersonic jet target
Report OL/NSF/R12, SRL Daresbury Laboratory
- Adamson T.C. Jr. & Messiter A.F. 1980
Analysis of Two-Dimensional Interactions between Shock Waves and Boundary Layers
Annual Review of Fluid Mechanics vol.12 103-138
- Alber I.E. & Lees L. 1968
Integral Theory for Supersonic Turbulent Base Flows
A.I.A.A. Journal vol.6 1343-1351
- Alber I.E., Bacon J.W., Masson B.S. & Collins D.J. 1973
An Experimental Investigation of Turbulent Transonic Viscous-Inviscid Interactions
A.I.A.A. Journal vol.11 no.5 620-627
- Anderson J.D. 1986
Lecture Notes: Introduction to Computational Fluid Dynamics
Von Kármán Institute, Rhode-Saint-Genèse, Belgium
- Ardonceanu P.L. & de Roquefort A. 1980
Direct and Inverse Calculation of the Laminar Boundary Layer Solution
A.I.A.A. Journal vol.18 no.11 1392-1394
- Arieli R. & Murphy J.D. 1980
Pseudo-Direct Solution to the Boundary Layer Equations for Separated Flow
A.I.A.A. Journal vol.18 no.8 883-891
- Arzoan Y. & Ben-Dor G. 1986
Fully Computerised Evaluation of Interferograms from Fluid Flow Investigations
International Journal of Heat & Fluid Flow vol.6 no.2 133-136
- Assassa G.M. & Papailiou K.D. 1979
An Integral Method for Calculation Turbulent Boundary Layers with Separation
A.S.M.E. Journal of Fluids Engineering vol.101 no.1 110-116
- Baldwin B.S. & Rose W.C. 1975
Calculation of Shock Separated Boundary Layers
N.A.S.A. Report SP347 401-417
- Barnett M. & Davis R.T. 1986
Calculation of Supersonic Flows with Strong Viscous-Inviscid Interaction
A.I.A.A. Journal vol.24 no.12 1949-1955

- Baum E. 1968
An Interaction Model of a Supersonic Boundary Layer on Sharp and Rounded Rear-Facing Steps
 A.I.A.A. Journal vol.6 no.3 440-447
- Ben-Dor G., Whitten B.T. & Glass I.I. 1979
Evaluation of Perfect and Imperfect Gas Interferograms by Computer
 International Journal of Heat & Fluid Flow vol.1 no.2 77-91
- Benwell S. 1984
Preliminary investigation into various methods of noise suppression for the Indaur' Flan
 B.Sc. Project Report, University of Exeter
- Bogdanoff D.W. 1983
The Optical Quality of Shear Layers: Prediction and Improvement Thereof
 A.I.A.A. Journal vol.22 no.1 58-64
- Bourque C. & Newman B.G. 1960
Reattachment of a Two-Dimensional, Incompressible Jet to an adjacent Flat Plate
 Aeronautical Quarterly vol.11 no.3 201-232
- Boyd R.D., Miller D.J. & Ghiglia D.C. 1983
Automated Data Reduction for Optical Interferometric Data
 140-144 in Flow Visualisation III, Yang W.J. ed., Springer Verlag, Berlin
- Bradshaw P. 1969
The analogy between streamline curvature and buoyancy in turbulent shear flow
 Journal of Fluid Mechanics vol.36 177-191
- Bradshaw P. 1972
A Bibliography of 'Complex' Turbulent Flows
 Aero. Report 72-04 Imperial College, London
- Bradshaw P. 1973
Effects of Streamline Curvature on Turbulent Flow
 N.A.T.O. AGARDograph 169
- Bradshaw P. 1974
The effect of mean compression or dilatation on the turbulence structure of supersonic boundary layers
 Journal of Fluid Mechanics vol.63 449-464
- Bradshaw P. 1975a
Complex Turbulent Flows
 A.S.M.E. Journal of Fluids Engineering vol.97 no.2 146-154
- Bradshaw P. 1975b
Prediction of Separation using Boundary Layer Theory
 N.A.T.O. AGARD CP168 Paper 11
- Bradshaw P., Cebeci T. & Whitelaw J.H. 1981
Engineering Calculation Methods for Turbulent Flow
 Academic Press, London
- Bradshaw P. & Ferris D.H. 1970
Calculation of Boundary-Layer Development using the Turbulent Energy Equation: VIII Compressible Heat Transfer
 Aero. Report 1325, National Physical Laboratory, England
- Bradshaw P. & Ferris D.H. 1971
Calculation of boundary-layer development using the turbulent energy equation: compressible flow on adiabatic walls
 Journal of Fluid Mechanics vol.46 83-110
- Bradshaw P., Ferris D.H. & Atwell N.P. 1967
Calculation of boundary-layer development using the turbulent energy equation
 Journal of Fluid Mechanics vol.28 593-616

- Bradshaw P. & Unsworth K. 1974
An Improved FORTRAN Program for the Bradshaw-Ferris-Attwell Method of Calculating Turbulent Shear Layers
 Aero. Report 74-02, Imperial College, London
- Brandeis J. & Rom J. 1980
Three Layer Interactive Method for Computing Supersonic Laminar Separated Flows
 A.I.A.A. Journal vol.18 no.11 1321-1327
- British Petroleum 1977
Flow Characteristics of Coanda Devices
 Private Communication, B.P. Research, Sunbury-on-Thames
- British Petroleum 1980
Loss of Coanda Effect II
 Private Communication, B.P. Research, Sunbury-on-Thames
- Brune G.W., Rubbert P.E. & Nark T.C. Jr. 1975
A New Approach to Inviscid Flow - Boundary Layer Matching
 A.I.A.A. Journal vol.13 no.7 936-938
- Carpenter P.W. 1978
Noise Suppression of the INDAIR Flare
 Report TN78/1, University of Exeter
- Carpenter P.W. & Tabakoff W. 1968
Survey and Evaluation of Supersonic Base Flow Theories
 N.A.S.A. Report CR97129
- Carrière P., Sirieix M. & Détery J. 1975
Méthodes de Calcul des Écoulements Turbulents Décollées en Supersonique
 Progress in Aerospace Sciences vol.16 385-429
- Carroll B.F. & Dutton J.C. 1985
Transonic Flow in the Throat Region of Radial or Nearly Radial Supersonic Nozzles
 A.I.A.A. Journal vol.23 no.7 1127-1129
- Carter J.E. 1979
A New Boundary Layer - Inviscid Iteration Technique for Separated Flow
 A.I.A.A. Paper 79-1450
- Carter J.E. & Wornom S.F. 1975
Solutions for Incompressible Separated Boundary Layers including Viscous/Inviscid Interaction
 N.A.S.A. Report SP347 125-150
- Catalano G.D., Morton J.B. & Humphris R.R. 1977
An Experimental Investigation of a Three-Dimensional Wall Jet
 A.I.A.A. Journal vol.15 no.8 1146-1151
- Cebeci T. & Smith A.M.O. 1974
Analysis of Turbulent Boundary Layers
 Academic Press, London
- Chang I.-Shih & Chow W.L. 1975
Mach Disc from underexpanded axisymmetric nozzle flow
 A.I.A.A. Journal vol.12 n.8 1079-1082
- Chow W.L. & Spring D.J. 1975
Viscous Interaction of Flow Redevelopment after Flow Reattachment with Supersonic External Streams
 A.I.A.A. Journal vol.13 no.12 1576-1584
- Connor J.J. & Brebbia C.A. 1976
Finite Element Techniques for Fluid Flow
 Newnes-Butterworth, London

- Crocco L. & Lees L. 1964
A Mixing Theory for the Interaction between Dissipative Flows and Nearly Isentropic Streams.
 Journal of Aerospace Science vol.19 no.10 649-676
- Curle N. 1978
Development and separation of a compressible laminar boundary layer under the action of a very sharp adverse pressure gradient
 Journal of Fluid Mechanics vol.84 385-400
- Dash S.M., Beddini R.A., Wolf D.E. & Sinha N. 1983
Viscous/Inviscid Analysis of Curved Sub- or Supersonic Wall Jets
 A.I.A.A. Paper 83-1679
- Dash S.M., Wilmoth R.G. & Pergament H.S. 1979
Overlaid Viscous/Inviscid Model for the Prediction of Near-Field Jet Entrainment
 A.I.A.A. Journal vol.17 no.9 950-938
- Dash S.M. & Wolf D.E. 1984
Interactive Phenomena in Supersonic Jet Mixing Problems. Parts I and II
 A.I.A.A. Journal vol.22 no.7 905-913 & no.10 1395-1404
- Degani D. & Steger J.L. 1983
Comparison between Navier-Stokes and Thin Layer Computations for Separated Supersonic Flow
 A.I.A.A. Journal vol.21 no.11 1604-1606
- Denton J.D. 1982
An Improved Time Marching Method for Turbomachinery Flow Calculation
 A.S.M.E. Paper 82-GT-239
- Drela M. & Giles M.B. 1986
Viscous-Inviscid Analysis of Transonic and Low Reynolds Number Airfoils
 A.I.A.A. Journal vol.25 no.10 1347-1355
- Dunagan S.E., Brown J.L. & Miles J.B. 1987
Holographic Interferometry Study of an Axisymmetric Shock-Wave/Boundary Layer Strong Interaction Flow
 A.I.A.A. Journal vol.25 no.2 294-299
- Duncan 1987
Interactive Fortran in MTS
 N.U.M.A.C., Universities of Durham and Newcastle upon Tyne
- Dvorak F.A. & Choi D.H. 1981
The Analysis of Circulation-Controlled Airfoils in Transonic Flow
 A.I.A.A. Proceedings
- El-Hady N.M. & Verma A.K. 1984
Instability of Compressible Boundary Layers along Curved Walls with Suction or Cooling
 A.I.A.A. Journal vol.22 no.2 206-213
- Elrafaee M.M., Wu J.C. & Lekoudis S.G. 1982
Solutions of the Compressible Navier-Stokes Equations using the Integral Method
 A.I.A.A. Journal vol.20 no.3 356-362
- El-Taher R.M. 1983
Experimental Investigation of Curvature Effects on Ventilated Wall Jets
 A.I.A.A. Journal vol.21 no.11 1505-1511
- Emanuel G. 1984
Supersonic Compressive Ramp without Laminar Boundary Layer Separation
 A.I.A.A. Journal vol.22 no.1 29-34

- Fekete G.I. 1963
Coanda Flow of a Two-Dimensional Wall Jet on the outside of a Circular Cylinder
M.E.R.L. Report 63-11, McGill University
- Felsing G.W. & Moller P.S. 1969
Coanda Flow over a Circular Cylinder with Injection Normal to the Surface
A.I.A.A. Journal vol.7 no.5 842-846
- Fernholz H.H. 1966
The Deflection of Free Jets at Convexly Curved Walls (Coanda Effect)
Canadian National Research Council Technical Translation 1504
- Fernholz H.H. 1967
Aerodynamische Hysterese, Steuerschneiden- und Reynoldszahl-Einfluß bei der Strömungsumlenkung und Ablösung an Stark gekrümmten Wänden (Coanda Effekt)
Zeitschrift für Flugwissenschaft vol.15 no.4 136-142
- Floryan J.M. 1989
Görtler Instability of Wall Jets
A.I.A.A. Journal vol.27 no.1 112-114
- GHOST Manual 1985
The GHOST-80 User Manual CLM-R241 (Edition 2)
U.K.A.E.A. Culham Laboratories, Abingdon
- Gibson M.M. & Rodi W. 1981
A Reynolds-stress closure model of turbulence applied to the calculation of a highly curved mixing layer
Journal of Fluid Mechanics vol.103 161-182
- Gibson M.M. & Younis B.A. 1982
Modelling the Curved Turbulent Wall Jet
A.I.A.A. Journal vol.20 no.12 1707-1712
- Gilchrist A.R. 1985
The Development and Breakaway of a Compressible Air Jet with Streamline Curvature and its Application to the Coanda Flare
Ph.D. Thesis, University of Durham
- Green J.E. 1970
Interactions between Shocks and Turbulent Boundary Layers
Progress in Aerospace Sciences vol.11 235-340
- Green P. 1987
The Fluid Dynamics and Aeroacoustics of External Coanda Flares
Ph.D. Thesis, University of Exeter
- Green P. & Carpenter P.W. 1983
Method of Integral Relations for Curved Compressible Turbulent Mixing Layers with Lateral Divergence
Numerical Methods in Laminar & Turbulent Flow, Pineridge Press, Swansea
- Gregory-Smith D.G., Gilchrist A.R. & Senior P. 1990
A combined system for measurements of high-speed flow by interferometry, schlieren and shadowgraph
Measurement Science & Technology (1990) 419-424
- Gregory-Smith D.G. & Robinson C.J. 1982
The Discharge from a Thin Slot over a Surface of Convex Curvature
International Journal of Mechanical Science vol.24 no.6 329-339
- Guitton, D.E. 1964
Two-Dimensional Turbulent Wall Jets over Curved Surfaces
M.E.R.L. Report 64-7, McGill University
- Guitton D.E. & Newman B.G. 1977
Self-preserving turbulent wall jets over convex surfaces
Journal of Fluid Mechanics vol.81 155-185

- Habashi W.G. & Hafez M.M. 1982
Finite Element Solutions of Transonic Flow Problems
 A.I.A.A. Journal vol.20 no.10 1368-1376
- Halim A. & Hafez M. 1984
Calculation of Separation Bubbles using Boundary Layer Type Equations
 395-415 in Rec. Adv. Num. Meth. Fluids vol.3, Pineridge Press, Swansea
- Hall M.G. 1982
Advances and Shortcomings in the Calculation of Inviscid Flows with Shock Waves
 33-62 in Roe P.L. ed., Num. Meth. Aeronaut. Fluid Dyn., Academic Press
- Hama F.R. 1966
Experimental Investigations of Wedge Base Pressure and Lip Shock
 N.A.S.A. Technical Report 32-1033
- Hankey W.L. & Holden M.S. 1975
Two-Dimensional Shock Wave - Boundary Layer Interactions in High Speed Flows
 N.A.T.O. AGARDograph 203
- Harris C.M. & Crede C.E. 1961
Shock and Vibration Handbook Volume 2: Data Analysis, Testing and Methods of Control
 McGraw-Hill, New York
- Havener A.G. 1988
Holographic Measurements of Transition and Turbulent Bursting in Supersonic Axisymmetric Boundary Layers
 A.I.A.A. Journal vol.26 no.12 1467-1476
- Havener A.G. & Radley R.J. Jr. 1974
Turbulent Boundary-Layer Flow Separation Measurements using Holographic Interferometry
 A.I.A.A. Journal vol.12 no.8 1071-1075
- Hesselink L. 1988
Digital Image Processing in Flow Visualization
 Annual Review of Fluid Mechanics vol.20 421-485
- Hoffman J.D. 1973
Accuracy Studies of the Numerical Method of Characteristics for Axisymmetric, Steady Supersonic Flow
 Journal of Computational Physics vol.11 210-239
- Hunt B.L. 1980
Calculation of Two-Dimensional and Three-Dimensional Regular Shock Intersections
 Aeronautical Journal (1980) 285-289
- Hunt B.L. & Lamont P.J. 1980
The impingement of underexpanded axisymmetric jets on perpendicular and inclined flat plates
 Journal of Fluid Mechanics vol.100 471-512
- Hussaini M.Y. & Zang T.A. 1987
Spectral Methods in Fluid Dynamics
 Annual Review of Fluid Mechanics vol.19 339-367
- Inger G.R. 1974
Supersonic Laminar Flow past a Small Rear-Facing Step
 A.I.A.A. Journal vol.12 no.6 739-740 & no.8 1157-1158
- Inger G.R. 1975
Three Dimensional Disturbances in Reattaching Separated Flows
 N.A.T.O. AGARD CP168
- Irwin H.P.A.H. & Arnot-Smith P. 1975
Prediction of the effect of streamline curvature on turbulence
 Physics of Fluids vol.18 no.6 624-630

- Issa R.I. & Lockwood F.C. 1977a
A Hybrid Marching Integration Procedure for the Prediction of Two-Dimensional Supersonic Boundary Layers
 A.S.M.E. Journal of Fluids Engineering vol.99 no.1 205-212
- Issa R.I. & Lockwood F.C. 1977b
On the Prediction of Two-Dimensional Supersonic Viscous Interactions Near Walls
 A.I.A.A. Journal vol.15 no.2 182-188
- Jenkins D.R. 1988
Interpretation of shadowgraph patterns in Rayleigh-Bénard convection
 Journal of Fluid Mechanics vol.190 451-469
- Jobe C.E. & Hankey W.L. 1980
Turbulent Boundary Layer Calculations in Adverse Pressure Gradient Flows
 A.I.A.A. Journal vol.18 no.11 1394-1397
- Johannesen N.H. & Meyer R.E. 1959
Axially-symmetric Supersonic Flow near the Centre of an Expansion
 Aeronautical Quarterly vol.2 127-142
- Johnson D.A., Horstman C.C. & Bacchalo W.D. 1980
Comparison between Experiment and Prediction for a Transonic Turbulent Separated Flow
 A.I.A.A. Paper 80-1407
- Kallinderis Y.G. & Baron J.R. 1989
Adaptation Methods for a New Navier-Stokes Algorithm
 A.I.A.A. Journal vol.27 no.1 37-43
- Keller H.B. 1978
Numerical Methods in Boundary Layer Theory
 Annual Review of Fluid Mechanics vol.10 417-443
- Keller J.B. 1957
Teapot Effect
 Journal of Applied Physics vol.28 no.8 859-864
- Keshavan N.R. 1975
Separation of a Turbulent Boundary Layer on a Lifting Cylinder
 A.I.A.A. Journal vol.13 no.2 252-253
- Korkegi R.H. 1975
Comparison of shock-induced two- and three-dimensional incipient turbulent separation
 A.I.A.A. Journal vol.13 no.4 534-535
- Kwon O.K. & Pletcher R.H. 1986
A Viscous-Inviscid Interaction Procedure
 A.S.M.E. Journal of Fluids Engineering vol.108 no.1 64-75
- Laderman A.J. 1979
Adverse Pressure Gradient Effects on Supersonic Boundary Layer Turbulence
 A.I.A.A. Paper 79-1563
- Lamont P.J. & Hunt B.L. 1976
The impingement of underexpanded axisymmetric jets on wedges
 Journal of Fluid Mechanics vol.76 307-336
- Lauder B.E. & Rodi W. 1981
The Turbulent Wall Jet
 Progress in Aerospace Sciences vol.19 81-128
- LeBalleur J.C. 1984
Strong Matching Methods for Computing Transonic Viscous Flow Including Wakes and Separations
 Rec. Adv. Num. Meth. Fluids vol.3 chap.14, Pineridge Press, Swansea

- Lee D. & Pletcher R.H. 1988
Simultaneous Viscous-Inviscid Interaction Calculation Procedure for Transonic Turbulent Flows
 A.I.A.A. Journal vol.26 no.11 1354-1362
- Lees L. & Reeves B.L. 1964
Supersonic Separated and Reattaching Laminar Flows - General Theory
 A.I.A.A. Journal vol.2 no.11 1907-1920
- Lighthill M.J. 1953
On Boundary Layers and Upstream Influence
 Proceedings of the Royal Society vol.217 series A 344-357, 478-507
- Liu X. & Squire L.C. 1988
An investigation of shock/boundary-layer interactions on curved surfaces at transonic speeds
 Journal of Fluid Mechanics 187 467-486
- Lourenco L., Khothapalli A., Buchlin J.M. & Riethmuller M.L. 1986
Noninvasive Experimental Technique for the Measurement of Unsteady Velocity Fields
 A.I.A.A. Journal vol.24 no.10 1715-1717
- MacCormack R.W. 1982
A Numerical Method for Solving the Equations of Compressible Viscous Flow
 A.I.A.A. Journal vol.20 no.9 1275-1281
- Magi E.C. & Gai S.L. 1988
Supersonic Base Pressure and Lipshock
 A.I.A.A. Journal vol.26 no.3 370-372
- Mahgoub H.E.H. & Bradshaw P. 1979
Calculation of Turbulent-Inviscid Flow Interactions with Large Normal Pressure Gradients
 A.I.A.A. Journal vol.17 no.10 1025-1029
- Marsilio R. & Moretti G. 1989
Shock-Fitting Method for Two-Dimensional Inviscid, Steady Supersonic Flows in Ducts
 Meccanica vol.24 216-222
- McCartin B.J. 1983
Applications of Exponential Splines in Computational Fluid Dynamics
 A.I.A.A. Journal vol.21 no.8 1059-1065
- McGlaughlin D.W. & Taft C.K. 1967
Fluidic Electrofluid Converter
 A.S.M.E. Journal of Basic Engineering vol.89 334-340
- Mehta R.D. 1988
Vortex/Separated Boundary Layer Interactions at Transonic Mach Numbers
 A.I.A.A. Journal vol.26 no.1 15-26
- Merzkirch W.F. 1974
Flow Visualisation
 Academic Press, London
- Metral A. & Zerner F. 1948
The Coanda Effect
 British TIL/T4207 translation from the French Pub. Sci. et Tech. du Min. de l'Air 218
- Miles J. 1984
Strange Attractors in Fluid Dynamics
 Advances in Applied Mechanics vol.24 189-214
- Moretti G. 1987
Computation of Flows with Shocks
 Annual Review of Fluid Mechanics vol.19 313-337

- Moretti G. 1988
Efficient Euler Solver with Many Applications
 A.I.A.A. Journal vol.26 no.6 655-660
- Morrison J.F. 1982
A Study of an Axi-Symmetric Wall Jet with Streamline Curvature and its Application to the Coanda Flare
 Ph.D. Thesis, University of Durham
- Morrison J.F. & Gregory-Smith D.G. 1984
Calculation of an Axisymmetric Turbulent Wall Jet Over a Surface of Convex Curvature
 International Journal of Heat and Fluid Flow vol.5 no.3 139-148
- Morton K.W. & Paisley M.F. 1989
A Finite Volume Scheme with Shock Fitting for the Steady Euler Equations
 Journal of Computational Physics vol.80 168-203
- Motallebi F. & Norbury J.F. 1981
The effect of base bleed on vortex shedding and base pressure in compressible flow
 Journal of Fluid Mechanics vol.110 273-292
- Muck K.C., Andreopoulos J. & Dussauge J.P. 1988
Unsteady Nature of Shock-Wave/Turbulent Boundary-Layer Interaction
 A.I.A.A. Journal vol.26 no.2 179-187
- Muck K.C., Hoffman P.H. & Bradshaw P. 1985
The effect of convex surface curvature on turbulent boundary layers
 Journal of Fluid Mechanics vol.161 347-369
- Murphy J.D., Presley L.L. & Rose W.C. 1975
On the Calculation of Supersonic Separating and Reattaching Flow
 N.A.S.A. Report SP347 151-175
- Myring F. & Young A.D. 1968
The Isobars in Boundary Layers at Supersonic Speeds
 Aeronautical Quarterly vol.19 105-126
- Nagano Y. & Hishida M. 1987
Improved Form of the $k-\epsilon$ Model for Wall Turbulent Shear Flows
 A.S.M.E. Journal of Fluids Engineering vol.109 part 2 156-160
- NAG Library 1988
NAG Fortran Library - Mark 13
 NAG Ltd., Oxford
- Narasimha R. & Sreenivasan K.R. 1979
Relaminarisation of Fluid Flows
 Advances in Applied Mechanics vol.19 222-310
- Newman B.G., Patel R.P. & Savage S.B. 1972
Three-Dimensional Wall Jet Originating from a Circular Orifice
 Aeronautical Quarterly vol.23 188-200
- Newman B.G. 1969
The Prediction of Turbulent Jets and Wall Jets
 Canadian Aerospace Journal vol.15 288-305
- Nieland V.Y. 1970
Asymptotic Theory of Plane Steady Supersonic Flows with Separation Zones
 372-381 in Fluid Dynamics vol.5, Plenum, New York
 (Translated from Izv. ANSSR Mekh. Zhid. Kost. i Gaza. vol.5 no.3 22-32)
- Norwood R.E. 1962
Two-dimensional Transonic Gas Jets
 Proc. 4th U.S. National Cong. Appl. Mech. vol.2 1359-1367

- Oriel 1980
Handling and Cleaning of Coated Optical Components
 Oriel Corporation, Stamford, USA
- Page R.H. & Przimbil C.E.G. 1975
Cinematographic Study of Separated Flow Regions
 N.A.T.O. AGARD CP168 paper 38
- Papamoschou D. & Roshko A. 1988
The compressible turbulent shear layer: an experimental study
 Journal of Fluid Mechanics vol.197 453-477
- Parsons C. 1988
An Experimental and Theoretical Study of the Aeroacoustics of External-Coanda Gas Flares
 Ph.D. Thesis, University of Exeter
- Parthasarthy S.P., Cho Y.I. & Back L.H. 1987
Wide-Field Shadowgraphy of Tip Vortices from a Helicopter Rotor
 A.I.A.A. Journal vol.25 no.1 64-70
- Patankar S.V. & Spalding D.B. 1972
A Calculation Procedure for Heat, Mass and Momentum Transfer in Three-Dimensional Parabolic Flows
 International Journal of Heat and Mass Transfer vol.15 1787-1806
- Patankar U.M. & Sridhar K. 1971
Three-dimensional Curved Wall Jets
 A.S.M.E. Paper 71-WA/FE-2
- Plotkin A. 1982
Spectral Method Solutions for Some Laminar Channel Flow with Separation
 A.I.A.A. Journal vol.20 no.12 1713-1719
- Presley L.L. 1975
Comparison of a Shock-Capturing Technique with Experimental Data for Three-Dimensional Internal Flows
 N.A.S.A. Report SP347 623-642
- Press W.H., Flannery B.P., Teukolsky S.A. & Vetterling W.T. 1986
Numerical Recipes - The Art of Scientific Computing (FORTRAN Version)
 Cambridge University Press
- Pritchard J.L. 1957
The Dawn of Aerodynamics
 Journal of the Royal Aeronautical Society, March 1957, 157
- Ramaprian B.R., & Shivaprasad B.G. 1977
Mean Flow Measurements in Turbulent Boundary Layers
 A.I.A.A. Journal vol.15 no.2 189-196
- Ribaut M. 1983
A Vortex Sheet Method for Calculating Separated Two-Dimensional Flows
 A.I.A.A. Journal vol.21 no.8 1079-1084
- Roderick W.E.B. 1961
Use of the Coanda-Effect for the Deflection of Jet Sheets Over Smoothly Curved Surfaces. Part II - Some Tests with Supersonic, Over and Under Expanded Jet Sheets
 UTIA Report TN51, University of Toronto
- Roe P.L. 1982
Numerical Modelling of Shockwaves and Other Discontinuities
 211-244 in Num. Meth. Aeronaut. Fluid Dyn., Roe P.L. ed., Academic Press
- Rose W.C. 1974
Turbulence Measurements in a Compressible Boundary Layer
 A.I.A.A. Journal vol.12 no.8 1060-1064

- Rotta J.C. 1967
Effect of Streamwise Wall Curvature on Compressible Turbulent Boundary Layers
 Physics of Fluids Supplement S174-S180
- Samimy M., Petrie H.L. & Addy A.L. 1986
Turbulent Reattaching Free Shear Layers
 A.I.A.A. Journal vol.24 no.2 261-267
- Schlichting H. 1955
Boundary-Layer Theory
 5th Edition, McGraw-Hill, New York
- Schlichting H. 1979
Boundary-Layer Theory
 7th Edition, McGraw-Hill, New York
- Schmidt E.M. & Shear D.D. 1975
Optical Measurements of Muzzle Blast
 A.I.A.A. Journal vol.13 no.8 1086-1091
- Schofield W.H. 1985
Turbulent boundary layer development in an adverse pressure gradient after an interaction with a normal shock wave
 Journal of Fluid Mechanics vol.154 43-62
- Senior P. 1986
Development of a Flow Computation Method
 S.E.A.S. Internal Report, University of Durham
- Settles G.S. 1973
Colour-Coding Schlieren Techniques for the Optical Study of Heat and Fluid Flow
 International Journal of Heat & Fluid Flow vol.6 no.1 3-15
- Settles G.S. 1983
Flow Visualisation Methods for Practical Aerodynamic Testing
 306-315 in Flow Visualisation III, Yang W.J. ed., Springer Verlag, Berlin
- Settles G.S. 1986
Modern Developments in Flow Visualisation
 A.I.A.A. Journal vol.24 no.8 1313-1323
- Shan-Fu S. 1978
Unsteady Separation According to the Boundary-Layer Equations
 Advances in Applied Mechanics vol.18 177-221
- Shand E.B. 1984
Glass Engineering Handbook
 McGraw-Hill, New York
- Shang J.S., Hankey W.L. Jr. & Dwoyer D.L. 1973
Numerical Analysis of Eddy Viscosity Models in Supersonic Turbulent Boundary Layers
 A.I.A.A. Journal vol.11 no.12 1677-1683
- Shankar V. 1982
Conservative Full Potential, Implicit Marching Scheme for Supersonic Flows
 A.I.A.A. Journal vol.20 no.11 1508-1514
- Sirieux M. 1975
Décollement Turbulent en Écoulement Bidimensionnel
 AGARD CP168 paper 12
- Smits A.J., Eaton J.A. & Bradshaw P. 1979
The response of a turbulent boundary layer to lateral divergence
 Journal of Fluid Mechanics vol.94 243-268
- Smits A.J., Young S.T.B. & Bradshaw P. 1979
The effect of short regions of high surface curvature on turbulent boundary layers
 Journal of Fluid Mechanics vol.94 209-242

- So R.M. & Mellor G.L. 1975
Experiment on Turbulent Boundary Layers on a Concave Wall
 Aeronautical Quarterly vol.16 35-40
- Sockol P.M. & Johnson W.A. 1986
Coupling Conditions for Boundary Layers and Rotational Inviscid Flow
 A.I.A.A. Journal vol.24 no.6 1033-1035
- Stanislas M. 1983
Ultra High Speed Smoke Visualisation of Unsteady Flows Using a Pulsed Ruby Laser
 42-44 in Flow Visualisation III, Yang W.J. ed., Springer Verlag, Berlin
- Stewartson K. 1974
Multistructured Boundary Layers on Flat Plates and Related Bodies
 Advances in Applied Mechanics vol.14 145-239
- Stollery J.L. 1969
Hypersonic Viscous Flow Over Concave and Convex Surfaces
 1969 Symp. Viscous Interaction Phenomena in Supersonic and Hypersonic Flow
- Stollery J.L. 1975
Laminar and Turbulent Boundary-Layer Separation at Supersonic and Hypersonic Speeds
 AGARD CP168 paper 20
- Stookesberry D.C. & Tannehill J.C. 1987
Computation of Separated Flow Using the Space Marching Conservative Supra-Characteristics Method
 A.I.A.A. Journal vol.25 no.8 1063-1070
- Stricker J. & Kafri O. 1982
A New Method for Density Gradient Measurements in Compressible Flows
 A.I.A.A. Journal vol.20 no.6 820-823
- Stricker J., Keren E. & Kafri O. 1983
Axisymmetric Density Field Measurements by Moiré Deflectometry
 A.I.A.A. Journal vol.21 no.12 1767-1769
- Sturek W.B. 1974
Turbulent Boundary-Layer Shear Stress Distributions for Compressible Adverse Pressure Gradient Flows
 A.I.A.A. Journal vol.12 no.3 375-376
- Swafford T.W. 1983
Analytical Approximation of Two-Dimensional Separated Turbulent Boundary Layer Velocity Profiles
 A.I.A.A. Journal vol.21 no.4 923-925
- Tanner M. 1973
Theoretical Prediction of Base Pressure for Steady Base Flow
 Progress in Aerospace Sciences vol.14 177-225
- Tanner M. 1978
Two Different Theoretical Approaches to the Base Pressure Problem in 2D Supersonic Flow
 Aeronautical Quarterly vol.29 no.2 14-130
- Tanner M. 1988
Base Cavity at Angles of Incidence
 A.I.A.A. Journal vol.26 no.3 376-377
- Vest V.M. 1979
Holographic Interferometry
 Wiley, New York

- Viegas J.R. & Horstmann C.C. 1979
Comparison of Multiequation Turbulence Models for Several Shock - Boundary Layer Interaction Flows
 A.I.A.A. Journal vol.17 no.8 811-820
- Voisinet R.L.P. 1975
An Experimental Investigation of the Compressible Turbulent Boundary Layer Induced by a Continuous Flow Compression
 AGARD CP168 paper 19
- Wadia A.R. 1979
Application of the Finite Element Method to Transonic Flows with Shocks
 A.I.A.A. Journal vol.17 no.10 1141-1142
- Watson 1987
Advice on CFD Method Implementation
 Private Conversation, Computation Group, B.P. Research, Sunbury-on-Thames
- Weinbaum S. 1966
Rapid Expansion of a Supersonic Boundary Layer and Its Application to the Near Wake
 A.I.A.A. Journal vol.4 no.2 217-226
- Werle M.J. & Bertke S.D. 1976
Application of an Interacting Boundary Layer Model to the Supersonic Turbulent Separation Problem
 Report AFL76-4-21, University of Cincinnati
- Werle M.J. & Vatsa V.N. 1974
New Method for Supersonic Boundary-Layer Separations
 A.I.A.A. Journal vol.12 no.11 1491-1497
- Whiffen M.C. & Ahuja K. 1983
An Improved Schlieren System and Some New Results on Acoustically Excited Jets
 Journal of Sound and Vibration vol.86 no.1 99-105
- Whitfield D.L., Swafford T.W. & Jacocks J.L. 1981
Calculation of Turbulent Boundary Layers with Separation and Viscous/Inviscid Interaction
 A.I.A.A. Journal vol.19 no.10 1315-1322
- Wilkins J., Witheridge R.E., Desty D.H., Mason J.T.H. & Newby N. 1977
The Design, Development and Performance of Indair and Mardair Flares
 Paper 2822, Offshore Technology Conference, Houston (1977)
- Wille R. & Fernholz H.H. 1965
Report on the First European Mechanics Colloquium on the Coanda effect
 Journal of Fluid Mechanics vol.23 801-819
- Wilson D.J. & Goldstein R.J. 1976
Turbulent Wall Jets with Cylindrical Streamwise Surface Curvature
 A.S.M.E. Journal of Fluids Engineering vol.98 550-557
- Winter K.G., Rotta J.C. & Smith K.G. 1968
Studies of the Turbulent Boundary Layer on a Waisted Body of Revolution in Subsonic and Supersonic Flow
 Aeronautical Research Council Report 3633
- Wu J.H.T., Elabdin M.N., Neemeh R.A. & Ostrowski P.P. 1977
The Structure of a Radially Directed Underexpanded Jet
 A.I.A.A. Journal vol.15 no.11 1651-1657
- Zucrow M.J. & Hoffman J.D. 1976
Gas Dynamics: Volumes I and II
 John Wiley & Sons, New York

